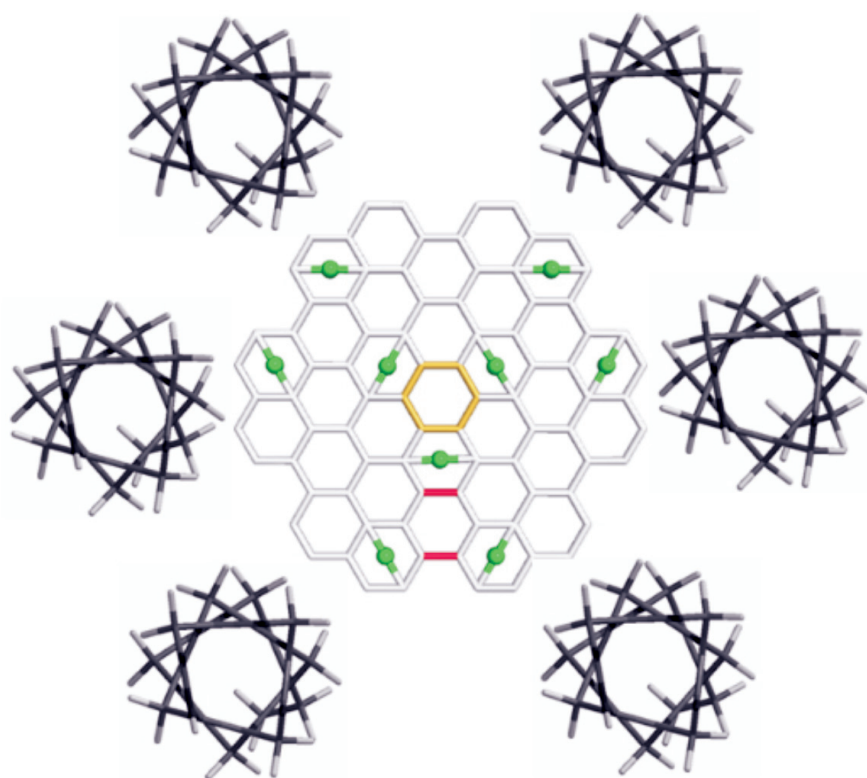




STUDIA UNIVERSITATIS
BABEŞ-BOLYAI



CHEMIA

1/2010

STUDIA

UNIVERSITATIS BABEȘ-BOLYAI

CHEMIA

1

Desktop Editing Office: 51ST B.P. Hasdeu Street, Cluj-Napoca, Romania, Phone + 40 264-405352

CUPRINS – CONTENT – SOMMAIRE – INHALT

VALENTINA TASOTI, ADRIAN NICOARĂ, PAUL ȘERBAN AGACHI, Investigation of AZ91 Magnesium Alloy Oxidation Kinetics by Means of Electrochemical Impedance Spectroscopy.....	5
LAURIAN VLASE, IOANA FELECAN, DANA MUNTEAN, DANIELA IACOB, Quantification of Phenobarbital in Human Plasma by LC/MS/MS for Therapeutic Drug Monitoring.....	15
ADRIANA HANGAN, JOAQUIN BORRAS, LUMINITA OPREAN, Cu(II) Complexes with N-substituted Sulfonamides	23
RADU SILAGHI-DUMITRESCU, Computational Description of Peptide Architectures Based on Hydrogen Bonds.....	31
LIANA MARIA MURESAN, JULIEN EYMARD, DIANA BLEJAN, EMIL INDREA, Zn-Ni Alloy Coatings from Alkaline Bath Containing Triethanolamine. Influence of Additives.....	37
ERIKA TASNADI, GABRIEL KATONA, MIRCEA V. DIUDEA, Modeling of Biologically Active Molecular Structures	45
ANAMARIA PADUREAN, CALIN-CRISTIAN CORMOS, ANA-MARIA CORMOS, PAUL-ȘERBAN AGACHI, Technical Assessment of CO ₂ Capture Using Alkanolamines Solutions.....	55

DIANA DUDEA, MARIOARA MOLDOVAN, LAURA SILAGHI DUMITRESCU, HORATIU COLOSI, ALEXANDRA BOTOS, ADA IRIMIE, CAMELIA ALB, In Vitro Study on the Effectiveness of a Group of Experimental Hydrogen Peroxide and Carbamide Peroxide Bleaching Gels upon Dental Enamel.....	65
KATALIN NAGY, CSABA L. NAGY, MIRCEA V. DIUDEA, Omega Polynomial in Diamond-Like Dendrimers.....	77
MAHBOUBEH SAHELI, MAHDIEH NEAMATI, KATALIN NAGY, MIRCEA V. DIUDEA, Omega Polynomial in Sucor Network	83
LAURIAN VLASE, DANIELA-SAVETA POPA, DANA MUNTEAN, MARCELA ACHIM, A New LC/MS/MS Method for Determination of Lisinopril in Human Plasma.....	91
LUCIAN COPOLOVICI, IOAN BALDEA, ALEXANDRA CSAVDARI, Determination of Aromatic Amines and Phenols by Kinetic Methods Based on Landolt Effect.....	103
ADRIAN PATRUT, KARL F. VON REDEN, DANIEL A. LOWY, SALVINA PASCA, LASZLO KEKEDY-NAGY, IRINA SOVAGO, Radiocarbon Dating of the Historic Oak of Tebea, Romania	113
NORBERT MUNTEAN, IOAN BÂLDEA, GABRIELLA SZABÓ, ZOLTÁN NOSZTICZIUS, Antioxidant Capacity Determination by the Briggs- Rauscher Oscillating Reaction in a Flow System	121

Studia Universitatis Babeş-Bolyai Chemia has been selected for coverage in Thomson Reuters products and custom information services. Beginning with V. 53 (1) 2008, this publication is indexed and abstracted in the following:

- Science Citation Index Expanded (also known as SciSearch®)
- Chemistry Citation Index®
- Journal Citation Reports/Science Edition

INVESTIGATION OF AZ91 MAGNESIUM ALLOY OXIDATION KINETICS BY MEANS OF ELECTROCHEMICAL IMPEDANCE SPECTROSCOPY

VALENTINA TASOTI^a, ADRIAN NICOARĂ^{b,*} AND PAUL ȘERBAN AGACHI^a

ABSTRACT. A magnesium alloy oxidation in alkaline solutions was investigated by electrochemical impedance spectroscopy. Recorded impedance spectra exhibited up to two capacitive loops, suggesting oxidation through adsorbed intermediates. For a kinetic description of reaction mechanism, equation of the parameters of Voigt-type electrical equivalent model were obtained and used for magnesium alloy oxidation in open circuit conditions.

Keywords: *Microarc oxidation, magnesium alloy, electrochemical impedance spectroscopy, kinetic mechanism*

INTRODUCTION

Magnesium alloys – which are increasingly used in automotive, aerospace and electronic industries – suffer for poor friction-reducing, anti-wear and corrosion resistance. Fortunately, these disadvantages can be significantly reduced by appropriate surface treatment techniques. Microarc oxidation is such a technique, which can be used to fabricate ceramic coatings on a various range of chemical active metals and their alloys [1-3]. As compared with other surface treatment techniques, microarc oxidation is economic efficient, easy to control, ecological friendly and versatile [4].

Microarc oxidation is an electrode process that combines conventional electrochemical oxidation with spark discharges, allowing the obtaining of a ceramic coating with good protective properties. It requires the use of high enough voltage to allow dielectric breakdown of formed oxide film, which occurs at discrete locations accompanied by spark discharges. These high-temperature and high-pressure discharges ensure not only the conditions indispensable for spinel formation from oxides, but also increase the oxidation rate [5].

^a *Babes-Bolyai University, Department of Chemical Engineering and Material Science, 11 Arany Janos, 400028 Cluj Napoca, Romania*

^b *Babes-Bolyai University, Department of Physical Chemistry, 11 Arany Janos, 400028 Cluj Napoca, Romania, anicoara@chem.ubbcluj.ro*

For better understanding of overall process a mathematic model was developed, describing distributions of electrical potential, charge flux and temperature [6]. In order to extend its predictive capabilities, further developments should include kinetic information about elementary reaction steps. In present study oxidation kinetics of AZ91 magnesium alloy (containing 9% Al and 1% Zn) was investigated by means of electrochemical impedance spectroscopy, in two electrolytes solutions, further denoted as solution no. 1 and no. 2, which are usual for microarc oxidation.

RESULTS AND DISCUSSION

Electrochemical impedance spectroscopy was chosen for its unique ability of revealing the response of the elementary reaction steps, by exhibiting in isolation a series of phenomena. Each slow enough phenomenon will exhibit a loop with increasing diameter as its rate decreases, whereas the time-constant is increasing as the inertia of corresponding phenomenon increases. Examples of such phenomena with corresponding time-constant (usually) increasing in mentioned order are: charge conduction by migration, charge balance, mass transport, surface relaxation with adsorbed intermediates and electrocrystallization. Only migration has negligible inertia, thus its elementary response, namely the ohmic resistance (R_{Ω}), is frequency-independent.

The plots of measured electrochemical impedance are presented in Fig. 1, exhibiting a high-frequency capacitive loop, with an additional low-frequency capacitive loop only in the case of solution no. 2. The high-frequency loop was assigned to charge balance phenomenon; its characteristics are the loop diameter, defined as charge transfer resistance (R_{ct}), and time-constant ($\tau_c = R_{ct}C_d$) which is also influenced by the double-layer capacity (C_d). The low-frequency loop was assigned to a phenomenon of surface relaxation with adsorbed intermediates and has as characteristics the adsorption resistance (R_a), defined as diameter of loop, and adsorption time-constant (τ_a). The absence of some other low-frequency loops, assignable to mass transport and electrocrystallization phenomena, proves that these elementary steps are fast enough to be ignored when modelling the process.

Qualitatively, charge transfer is the slowest elementary step and is marginally influenced by electrolyte concentration. Conversely, the surface relaxation loop is much more influenced by electrolyte concentration, whereas the contribution of this phenomenon to overall process is minor.

To quantify these phenomena, the experimental impedance spectra are fitted with a *Voight*-type electrical equivalent model, constructed by serial connection between the ohmic resistor and two parallel resistor-capacitor elements [7]. The fitting model describing the influence of frequency on impedance's modulus is:

$$|Z(f)| = \left\{ \left[R_{\Omega} + \frac{R_{ct}(1 + 2\pi f R_{ct} C_d \sin \alpha)}{1 + 4\pi f R_{ct} C_d \sin \alpha + (2\pi f R_{ct} C_d)^2} + \frac{R_a}{1 + (2\pi f \tau_a)^2} \right]^2 + \left[\frac{2\pi f R_{ct}^2 C_d \cos \alpha}{1 + 4\pi f R_{ct} C_d \sin \alpha + (2\pi f R_{ct} C_d)^2} + \frac{2\pi f R_a \tau_a}{1 + (2\pi f \tau_a)^2} \right]^2 \right\}^{1/2} \quad (1)$$

and is employed for calculation of the following model parameters: R_{Ω} , R_{ct} , C_d , R_a , τ_a and α ; the last one, without kinetic relevance, describes the flattening of loop caused by electrode roughness [8].

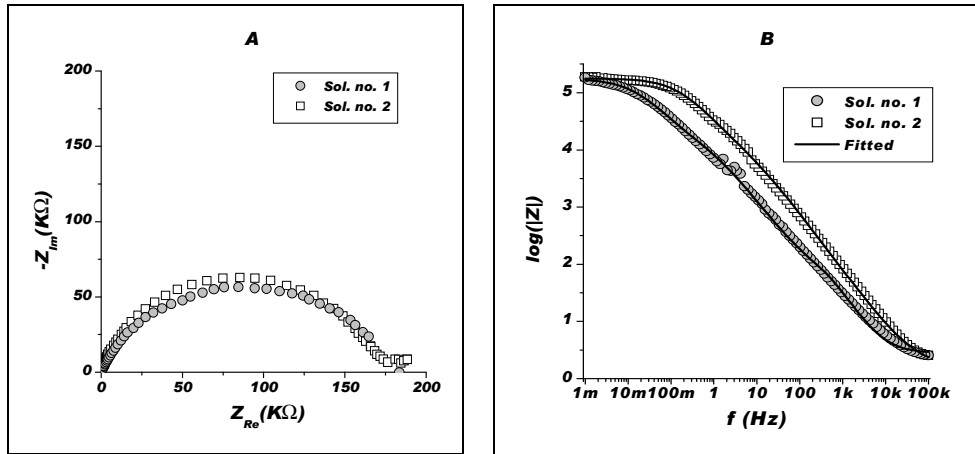


Figure 1. Measured spectra as complex-plane (A) and Bode (B) impedance plots, for oxidation of AZ91 alloy in electrolyte solutions presented in legend. In addition, in (B) fitted spectra are also presented as solid lines

The fittings were performed utilizing the nonlinear Levenberg-Marquardt algorithm implemented on Microcal Origin[®] 6.1. The results of this iterative fitting procedure are presented in Table 1 (line A) as estimates of the value and of the standard error, for 0.95 level of confidence, of the above-mentioned model parameters. Being kinetic relevant, the average of measured dc current is also presented in Table 1.

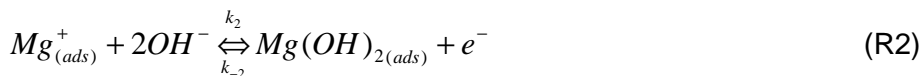
Although useful in describing the behaviour of elementary phenomena, Voigt model parameters can be further correlated with the rates of elementary reaction through a herein developed mathematic model. In order to maintain the model complexity into reasonable limits, only the behaviour of magnesium, the main constituent of the AZ91 alloy, was taken into account.

Table 1. Results of fitting procedures: A) electrical equivalent circuit parameters obtained by fitting experimental spectra; B) fitting of the obtained parameters leading to the kinetic parameters (rate constants and symmetry factors) presented in text.

Fitted data/ Fitting model	Sol.	I (nA)	R _{ct} (kΩ)	R _a (kΩ)	τ _a (s)	R _Ω (Ω)	C _d (μF)	α (rad)
A. Experimental spectra/ Eq. (1)	1	4.9±1.6 ^(a)	174±9	– ^(b)	– ^(b)	2.1±0.4	9.3±0.9	0.72±1.0
	2	4.2±1.8 ^(a)	169±14	20±8	61±19	1.6±0.2	2.5±0.3	0.76±1.2
B. Electric parameters/ Eqs. (2); (11); (17); (26)	1	4.97	176	2.31	100.9	without kinetic relevance		
	2	4.32	169	19.9	60.7			

(a) the average measured of dc current; (b) data unavailable due to the absence of low-frequency loop.

The chemical mechanism is considered as follows:



The faradaic current (I_F) and the coverage fractions of the adsorbed species generated by the two oxidation steps (θ_1 , θ_2) are introduced by the charge (in steady-state) and the mass balance equations:

$$\frac{I_F}{AF} = k_1(1 - \theta_1 - \theta_2) - k_{-1}\theta_1 + k_2C_{OH^-}\theta_1 - k_{-2}\theta_2 \quad (2)$$

$$\Gamma_{\max_1} \frac{d\theta_1}{dt} = k_1(1 - \theta_1 - \theta_2) + k_{-2}\theta_2 - k_{-1}\theta_1 - k_2C_{OH^-}\theta_1 \quad (3)$$

$$\Gamma_{\max_2} \frac{d\theta_2}{dt} = k_2C_{OH^-}\theta_1 - k_{-2}\theta_2 - k_3\theta_2 \quad (4)$$

where: A is the electrode area, F is the Faraday number, C_{OH^-} the interfacial concentration of OH^- and Γ_{\max_i} are the maximum surface concentrations of corresponding adsorbed species. In addition, k_1 , k_2 and k_{-1} , k_{-2} are the rate constants of considered elementary reaction steps during oxidation and reduction, respectively; k_3 reflects the coverage clearing steps, like surface diffusion towards growing crystallites.

An important feature of the electrochemical impedance spectroscopy is the possibility of operating measurements in steady-state conditions.

Accordingly, steady-state coverage fractions can be easily calculated using the mass balance equations, by assuming solely their time-independence. The obtained equations are:

$$\theta_1 = \frac{1}{1 + \frac{k_{-1}}{k_1} + \frac{k_2 C_{OH^-}}{k_1} + \left(1 - \frac{k_{-2}}{k_1}\right) \frac{k_2 C_{OH^-}}{k_{-2} + k_3}} \quad (5)$$

$$\theta_2 = \frac{1}{1 + \frac{k_3}{k_1} + \left(1 + \frac{k_{-1}}{k_1}\right) \frac{k_{-2} + k_3}{k_2 C_{OH^-}}} \quad (6)$$

The faradaic impedance (Z_F) can be obtained by taking into account the function of state nature of faradaic current, namely $I_F = I_F(E, \theta_1, \theta_2)$ as can be seen in eq. (2). In absence of experimental evidence supporting the contribution of mass transport to the overall process, C_{OH^-} was not considered as an associate variable. Consequently, faradaic current differential is the exact differential expression:

$$dI_F = \left. \frac{\partial I_F}{\partial E} \right|_{\theta_1, \theta_2} dE + \left. \frac{\partial I_F}{\partial \theta_1} \right|_{E, \theta_2} d\theta_1 + \left. \frac{\partial I_F}{\partial \theta_2} \right|_{E, \theta_1} d\theta_2 \quad (7)$$

and can be used to introduce the faradaic impedance as:

$$\frac{1}{Z_F} \equiv \frac{dI_F}{dE} = \left. \frac{\partial I_F}{\partial E} \right|_{\theta_1, \theta_2} + \left. \frac{\partial I_F}{\partial \theta_1} \right|_{E, \theta_2} \frac{d\theta_1}{dE} + \left. \frac{\partial I_F}{\partial \theta_2} \right|_{E, \theta_1} \frac{d\theta_2}{dE} \quad (8)$$

The three partial derivatives of faradaic current are calculated assuming common exponential activation of reaction rates for an electrochemical processes ($i=1,2$), namely:

$$k_i = k_i^o \exp\left[(1 - \beta_i) \frac{F}{RT} (E - E_i^o)\right] \quad (9)$$

$$k_{-i} = k_{-i}^o \exp\left[-\beta_i \frac{F}{RT} (E - E_i^o)\right] \quad (10)$$

The newly introduced terms are as follows: k_i^o are standard rate constants, β_i the transfer coefficients, E_i^o the standard potentials and R is the gas constant. The obtained equations for the partial derivatives are:

$$\left. \frac{\partial I_F}{\partial E} \right|_{\theta_1, \theta_2} \equiv \frac{1}{R_{ct}} = \frac{F^2 A}{RT} \left[(1 - \beta_1) k_1 (1 - \theta_1 - \theta_2) + \beta_1 k_{-1} \theta_1 + (1 - \beta_2) k_2 C_{OH^-} \theta_1 + \beta_2 k_{-2} \theta_2 \right] \quad (11)$$

$$\left. \frac{\partial I_F}{\partial \theta_1} \right|_{E, \theta_2} = -FA(k_1 + k_{-1} - k_2 C_{OH^-}) \quad (12)$$

$$\left. \frac{\partial I_F}{\partial \theta_2} \right|_{E, \theta_1} = -FA(k_1 + k_{-2}) \quad (13)$$

where eq. (11) introduces the charge transfer resistance (R_{ct}).

The calculation of the remanding terms from eq. (8) requests differentiation of the mass balance equations, after a prior transformation of time-dependent variables into frequency-dependent ones by means of Fourier transform. If M_1 denotes the right-hand side of eq. (3), one obtains:

$$j\omega\Gamma_{\max_1} d\theta_1 = \left[\left. \frac{\partial M_1}{\partial E} \right|_{\theta_1, \theta_2} \right] dE + \left[\left. \frac{\partial M_1}{\partial \theta_1} \right|_{E, \theta_2} \right] d\theta_1 + \left[\left. \frac{\partial M_1}{\partial \theta_2} \right|_{E, \theta_1} \right] d\theta_2 \quad (14)$$

where j is the complex operator and ω , the pulsation. Similarly, by denoting with M_2 the right-hand side of eq. (4), after a convenient rearrangement, the equations of coverage fractions total derivatives become:

$$\frac{d\theta_1}{dE} = \frac{A_{1,1}(1 + j\omega\tau_2) + A_{1,2}A_{2,1}}{(1 + j\omega\tau_1)(1 + j\omega\tau_2) - A_{1,2}A_{2,2}} \quad (15)$$

$$\frac{d\theta_2}{dE} = \frac{A_{2,1}(1 + j\omega\tau_1) + A_{1,1}A_{2,2}}{(1 + j\omega\tau_1)(1 + j\omega\tau_2) - A_{1,2}A_{2,2}} \quad (16)$$

where we defined the relaxation time-constants of adsorbed species (τ_i) and several *ad hoc* kinetic terms ($A_{i,j}$) as:

$$\tau_1 = -\Gamma_{\max_1} \left/ \left. \frac{\partial M_1}{\partial \theta_1} \right|_{E, \theta_2} \right. = \frac{\Gamma_{\max_1}}{k_1 + k_2 C_{OH^-} + k_{-1}} \quad (17)$$

$$\tau_2 = -\Gamma_{\max_2} \left/ \left. \frac{\partial M_2}{\partial \theta_2} \right|_{E, \theta_1} \right. = \frac{\Gamma_{\max_2}}{k_{-2} + k_3} \quad (18)$$

$$A_{1,1} = -\left. \frac{\partial M_1}{\partial E} \right|_{\theta_1, \theta_2} \left/ \left. \frac{\partial M_1}{\partial \theta_1} \right|_{E, \theta_2} \right. = \frac{F}{RT} \frac{(1 - \beta_1)k_1(1 - \theta_1 - \theta_2) + \beta_1 k_{-1} \theta_1 - (1 - \beta_2)k_2 C_{OH^-} \theta_1 - \beta_2 k_{-2} \theta_2}{k_1 + k_2 C_{OH^-} + k_{-1}} \quad (19)$$

$$A_{1,2} = -\left. \frac{\partial M_1}{\partial \theta_2} \right|_{E, \theta_1} \left/ \left. \frac{\partial M_1}{\partial \theta_1} \right|_{E, \theta_2} \right. = \frac{k_{-2} - k_1}{k_1 + k_2 C_{OH^-} + k_{-1}} \quad (20)$$

$$A_{2,1} = -\left. \frac{\partial M_2}{\partial E} \right|_{\theta_1, \theta_2} \left/ \left. \frac{\partial M_2}{\partial \theta_2} \right|_{E, \theta_1} \right. = \frac{F}{RT} \frac{(1 - \beta_2)k_2 C_{OH^-} \theta_1 + \beta_2 k_{-2} \theta_2}{k_{-2} + k_3} \quad (21)$$

$$A_{2,2} = - \frac{\partial M_2}{\partial \theta_1} \Big|_{E, \theta_2} / \frac{\partial M_2}{\partial \theta_2} \Big|_{E, \theta_1} = \frac{k_2 C_{OH^-}}{k_{-2} + k_3} \quad (22)$$

Finally, the equation of faradaic impedance becomes:

$$\frac{1}{Z_F} = \frac{1}{R_{ct}} - FA \frac{(k_1 + k_{-1} + k_2 C_{OH^-})[A_{1,1}(1 + j\omega\tau_2) + A_{1,2}A_{2,1}] + (k_1 + k_{-2})[A_{2,1}(1 + j\omega\tau_1) + A_{1,1}A_{2,2}]}{(1 + j\omega\tau_1)(1 + j\omega\tau_2) - A_{1,2}A_{2,2}} \quad (23)$$

This equation describes the faradaic impedance for the proposed reaction mechanism and exhibits a relaxation phenomenon (i.e., semicircular loop on complex plane representation) for each adsorbed intermediates. In investigated frequency range, maximum one adsorption-related relaxation phenomenon can be evidenced experimentally, allowing us to simplify eq. (23). For instance, if $\tau_2 \ll \tau_1$, one can approximate $1 + j\omega\tau_2 \approx 1$; that is, the loop related to surface relaxation of the $Mg(OH)_{2(ads)}$ is exhibited only at frequencies lower than those used experimentally. This particular simplifying case was further considered because this loop emerges only for high C_{OH^-} . Thus, its corresponding time-constant must be function of C_{OH^-} and, because only eq. (17) fulfils this condition, it allows us to consider the assumption reasonable. In these conditions, the equation of faradaic impedance becomes:

$$\frac{1}{Z_F} = \frac{1}{R_{ct}} - FA \frac{(k_1 + k_{-1} + k_2 C_{OH^-})(A_{1,1} + A_{1,2}A_{2,1}) + (k_1 + k_{-2})[A_{2,1}(1 + j\omega\tau_1) + A_{1,1}A_{2,2}]}{1 - A_{1,2}A_{2,2} + j\omega\tau_1} \quad (24)$$

To calculate the adsorption resistance (R_a), one has to first calculate the faradaic impedance for infinite small frequency:

$$\frac{1}{Z_F} \Big|_{\omega \rightarrow 0} = \frac{1}{R_{ct}} - FA \frac{(k_1 + k_{-1} + k_2 C_{OH^-})(A_{1,1} + A_{1,2}A_{2,1}) + (k_1 + k_{-2})(A_{2,1} + A_{1,1}A_{2,2})}{1 - A_{1,2}A_{2,2}} \quad (25)$$

After using its definition, it leads to:

$$R_a \equiv Z_F \Big|_{\omega \rightarrow 0} - R_{ct} = \frac{1}{\frac{1}{R_{ct}} - FA \frac{(k_1 + k_{-1} + k_2 C_{OH^-})(A_{1,1} + A_{1,2}A_{2,1}) + (k_1 + k_{-2})(A_{2,1} + A_{1,1}A_{2,2})}{1 - A_{1,2}A_{2,2}}} - R_{ct} \quad (26)$$

In conclusion, the impedance analytic model allows the formulation of a series of variables that contain kinetic information, namely I_F , R_{ct} , R_a and $\tau_a \equiv \tau_1$, all explicitly dependent on rate constants of the elementary reaction steps.

Calculation of the individual reactions rate constants was performed using another non-linear fitting procedure with the Levenberg-Marquardt algorithm. The dependent variable in this case is a vector with I_F , R_{ct} , R_a and τ_a as components, whereas C_{OH^-} is the independent variable and the model coefficients are the kinetic parameters (k_1 , k_{-1} , k_2 , k_{-2} , k_3 and β_1). In order to avoid solving an underdetermined mathematical problem, values for two other parameters were attributed ($\beta_2=0.5$, $\Gamma_{max1}=1.62 \cdot 10^{-9}$ mol cm⁻²). The attributed value for transfer coefficient is common and should not influence significantly the obtained results if reaction (R2) is a fast one. Γ_{max1} was theoretically calculated under following assumptions: compact packing of magnesium atoms with $1.72 \cdot 10^{-8}$ cm atomic radius.

The fitting results consist in model parameters estimates ($k_1=1.65 \cdot 10^{-12}$ mol cm⁻² s⁻¹, $k_{-1}=10^{-14}$ mol cm⁻² s⁻¹, $k_2=8.8 \cdot 10^{-9}$ cm s⁻¹, $k_{-2}=8 \cdot 10^{-12}$ mol cm⁻² s⁻¹, $k_3=10^{-11}$ mol cm⁻² s⁻¹ and $\beta_1=0.39$) and calculated dependent variables, presented in Tab. 1 line (B), which are in very good correlation with those obtained on impedance spectra fitting, presented in Tab. 1 line (A). To further compare the obtained values, one should use the values of apparent rate constant ($k_2' \equiv k_2 C_{OH^-}$), being $1.3 \cdot 10^{-11}$ mol cm⁻² s⁻¹ and $2.6 \cdot 10^{-11}$ mol cm⁻² s⁻¹ for solution no. 1 and 2, respectively.

The determined values suggest that the first oxidation step (R1) is relatively slow and thermodynamically irreversible, whereas the second oxidation step (R2) is significantly faster and rather reversible. The last considered step, that of coverage clearing (R3), is also a fast step and no further evidence about its reversibility can be obtained by the analysis of the presented data. More importantly, although oxidation takes place in a succession of reversible and irreversible steps, under given experimental conditions the slowest step is reaction (R1). However, the experimental evidencing of adsorption-related relaxation phenomenon makes imperative to take into account the reaction steps in which the adsorbed intermediate is involved, especially when a nonstationary model is considered.

Another important kinetic feature found is the difference between symmetry factors of the two oxidation elementary steps. In the investigated case, by increasing the potential, the reaction (R1) is favoured in comparison with reaction (R2), as it can be seen in eq. (9). Unlike in the present study, when the open circuit potential is applied, a much higher potential must be employed in order to sustain microarc oxidation, condition in which reaction (R2) could even be slower than (R1).

Further studies, especially aiming the influence of temperature, are requested for a realistic kinetic description of the microarc oxidation process. Because direct investigation of the microarc oxidation is rather difficult, mainly due to its intrinsic nonstationarity, the electrochemical impedance spectroscopy can provide both qualitative and quantitative information about the discussed process even if the investigation is performed in more convenient conditions.

EXPERIMENTAL SECTION

The working electrode made of AZ91 magnesium alloy was cut to 1 cm². Prior to being use it was polished, with up to 2500 grid paper under ethanol, cleaned in an ultrasonic bath and then dried with cold air. A saturated calomel electrode and a platinum counter electrode, with surface of 2 cm², completed the employed conventional three-electrode setup. To improve the signal-to-noise ratio, the electrochemical cell was introduced into a Faraday cage.

The two employed electrolyte solutions were made up in distilled water, both containing 0.5M KF and 0.25M Na₃PO₄; in addition, 1.5 or 3M of KOH, and 0.5 or 1M of NaAlO₂ was employed when preparing solutions no. 1 or no. 2, respectively. Analytical grade reagents were used in all cases.

Electrochemical impedance spectroscopy measurements were undertaken using an Autolab PGSTAT 302 (Eco Chemie, The Netherlands) potentiostat equipped with FRA2 module. Impedance spectrums were obtained at open circuit potential (of -1.21 V vs. SCE), at 25±1 °C, using perturbation of 10 mV amplitude.

ACKNOWLEDGEMENTS

One of the authors, V. Tasoti, gratefully acknowledges Dr. Patrik Schmutz (Swiss Federal Laboratories for Materials Testing and Research, Dübendorf, Switzerland) for providing the facilities for carrying out the experimental part of this work and for fruitful discussions.

REFERENCES

- 1 J. Liang, B. Guo, J. Tian, H. Liu, J. Zhou, T. Xu, *Applied Surface Science*, **2005**, 252, 345.
- 2 P.I. Butyagin, Ye.V. Khokhryakov, A.I. Mamaev, *Materials Letters*, **2003**, 57, 1749.
- 3 Y. Wang, T. Lei, B. Jiang, L. Guo *Applied Surface Science*, **2004**, 233, 258.
- 4 S. Verdier, M. Boinet, S. Maximovitch, F. Dalard, *Corrosion Science*, **2005**, 47, 1429.
- 5 Y.Q. Wang, K. Wu, M.Y. Zheng, *Surface Coating Technology*, **2006**, 201, 353.
- 6 V. Tasoti, S. Agachi, J. P. Caire, *Proceedings of 30th International Conference of Slovak Society of Chemical Engineering*, **2003**, 1, P146 1-6.
- 7 J. R. Macdonald, "Impedance spectroscopy Emphasizing solid materials and systems", John Wiley and Sons, New York, **1987**, p. 179-188.
- 8 F. Berthier, J.-P. Diard, R. Michel, *Journal of Electroanalytical Chemistry*, **2001**, 510, 1.

QUANTIFICATION OF PHENOBARBITAL IN HUMAN PLASMA BY LC/MS/MS FOR THERAPEUTIC DRUG MONITORING

LAURIAN VLASE^a, IOANA FELECAN^a, DANA MUNTEAN^{a,b},
DANIELA IACOB^c

ABSTRACT. A simple and sensitive LC/MS/MS method for quantification of phenobarbital and in human plasma has been developed and validated. Phenobarbital was separated under isocratic conditions using a mobile phase of 70:30 (v/v) 0.1% acetic acid and acetonitrile. In these chromatographic conditions, the retention time of phenobarbital was 1.2 min and the overall time of one analysis was 1.7 min. Plasma sample preparation consisted in protein precipitation with methanol. The detection of phenobarbital was realized in MRM mode using an ion trap mass spectrometer with electrospray negative ionization. The linearity domain was established between 2.00 and 80.00 µg/mL. Accuracy (bias%) and precision (CV%) were less than 9.8% for intra-day assay and 12.6% for inter-day assay. The recovery ranged between 95.9 and 136.4%. The method is very simple and fast and was used for therapeutic drug monitoring of phenobarbital.

Keywords: phenobarbital, LC/MS/MS, therapeutic drug monitoring

INTRODUCTION

Phenobarbital, 5-Ethyl-5-phenyl-2,4,6-pyrimidinetrione, is widely used for his properties as anesthetic, sedative, hypnotic and anticonvulsant drug (Fig. 1). After oral administration phenobarbital presents 95% bioavailability, with a very long half life of 72 to 144 hours. Phenobarbital is metabolized by the liver, mainly through hydroxylation and glucuronidation and it is excreted primarily by the kidneys. The currently accepted therapeutic concentration range for phenobarbital in plasma is 10 to 30 µg/mL [1].

Being a drug with large inter-subject variability and narrow therapeutic window, therapeutic drug monitoring is required for phenobarbital in order to improve its pharmacotherapy and safety.

^a University of Medicine and Pharmacy "Iuliu Hațieganu", Faculty of Pharmacy, Emil Isac 13, RO-400023, Cluj-Napoca, Romania, vlaselaur@yahoo.com

^b "Babeș-Bolyai" University, Faculty of Chemistry and Chemical Engineering, Arany Janos 11, RO-400028, Cluj-Napoca, Romania

^c University of Medicine and Pharmacy "Iuliu Hațieganu", Faculty of Medicine, Emil Isac 13, RO-400023, Cluj-Napoca, Romania

Several methods for determination of phenobarbital concentration in human plasma have been reported. Mainly, high performance liquid chromatography (HPLC) methods with UV detection were described [2,4,5], Liquid chromatography coupled with mass spectrometry (LC/MS or LC/MS/MS) methods were reported also [3]. LC/MS has been widely accepted as the most used method in the identification and quantitative analysis of drugs and its metabolites because of its superior sensitivity and specificity.

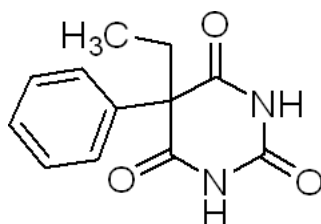


Figure 1. Molecular structure of phenobarbital

The aim of present study is the development of a rapid and specific LC/MS/MS method for the quantification of phenobarbital in human plasma in order to be applied in therapeutic drug monitoring or pharmacokinetic studies. In comparison with previously published HPLC methods (Table 1), the proposed method has the advantage of simple sample preparation by protein precipitation and a very short time of analysis.

RESULTS AND DISCUSSION

In the electric field created by the electrospray ionization source, the molecule of phenobarbital readily loose an proton, an negative ion being generated, with m/z 231 (Fig. 2). Thus, the detection of phenobarbital was carried out in multiple reaction monitoring (MRM) mode, by fragmentation of the parent ion with the m/z 231. The fragmentation of the parent ion is induced by collision of the ion with helium in the ion trap and a stable product ion with m/z 188 is observed in the mass spectra (Fig. 2). Finally, the abundance of ion with m/z 188 was monitored and quantitatively correlated with phenobarbital concentration. The retention time of phenobarbital was 1.2 min (Fig. 3) and, due detection specificity, no significant interference was observed at the retention time in plasma blank samples chromatograms.

Table 1. Analytical characteristics of several reported HPLC or LC/MS methods for the determination of phenobarbital in plasma

References	Matrix	Detection	Mobile phase constituents	Extraction	LOQ (µg/mL)	Run time (min)
Paibir et al. [2]	Human urine	HPLC-UV	12:88 (v/v) acetonitrile- H_3PO_4 (pH 2.3; 0.025 M)	Filtration	0.7	50
Kanazawa et al. [3]	Human plasma	LC-APCI-MS	30:70 (v/v) acetonitrile-0.1 M potassium phosphate buffer	Solid phase extraction	n/a	8
Moriyama et al. [4]	Rat offspring plasma	HPLC-UV	25:75 (v/v) acetonitrile-0.01 M KH_2PO_4	Solid phase extraction	5	10
Costa Q et al. [5]	Human plasma	HPLC-UV	22:78 (v/v) acetonitrile-water	Stir bar-sorptive extraction	0.08	5

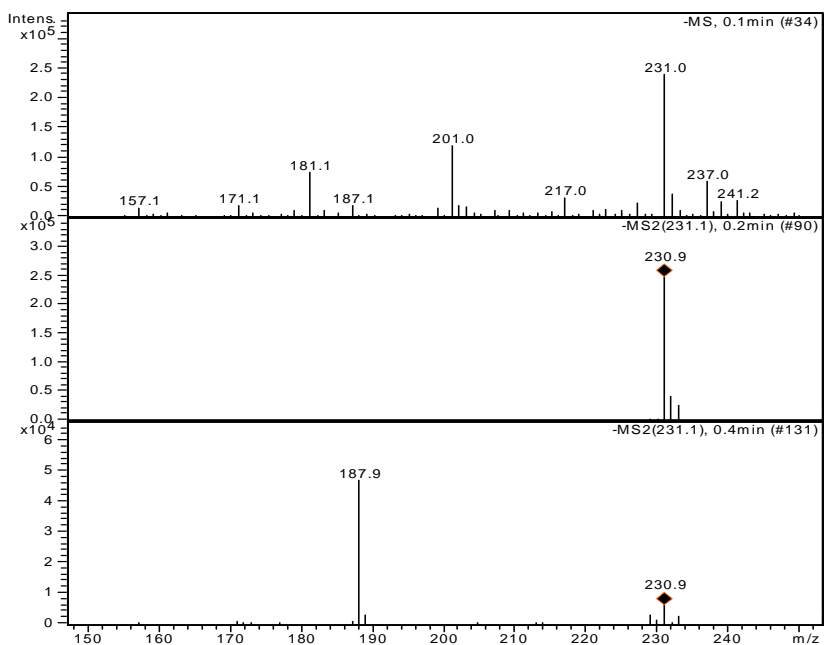


Figure 2. Ion mass spectra used for detection and quantification of phenobarbital from human plasma (upper spectra - full scan, middle spectra - isolation, lower spectra - fragmentation).

The calibration curves showed linear response over the range of concentration used in the assay procedure. The calibration curve for phenobarbital was in the concentration range 2.00-80.00 $\mu\text{g/mL}$, using 7 calibration levels, $n = 5$ days, with a coefficient of correlation greater than 0.997. The residuals had no tendency of variation with concentration and were between $\pm 14.6\%$ values.

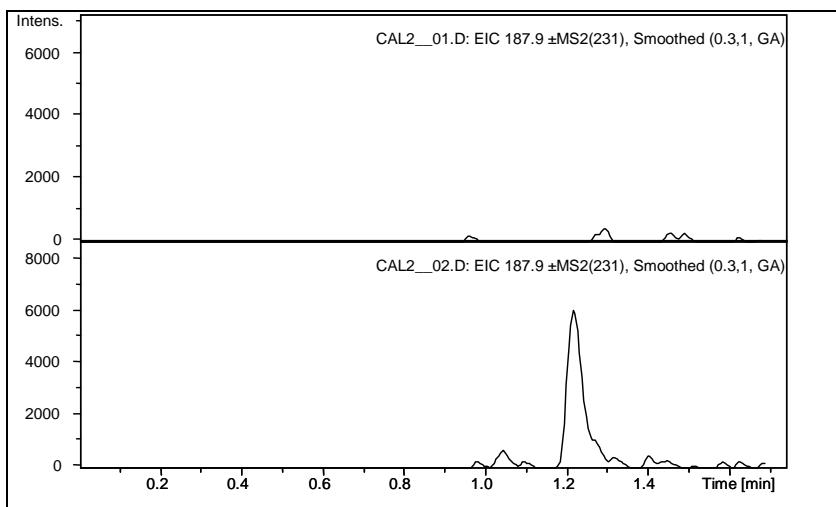


Figure 3. Typical chromatogram of the LLOQ plasma standard with 2.00 $\mu\text{g/mL}$ phenobarbital

The inter- and intra-day precision and accuracy results are showed in Table 2 and Table 3 and they are in agreement to international regulations regarding bioanalytical methods validation [6-11]. Precision and accuracy were from -6.7% to 9.8% for intra-day assay and from -1.2% to 12.6% for inter-day assay. The lower limit of quantification was established at 2.00 $\mu\text{g/mL}$ phenobarbital. Precision and accuracy at quantification limit were 15.4% and -17.8% for intra-day determinations and 11.4% and 6.8% for inter-day determinations, respectively. The recovery was consistent and ranged between 95.9 and 136.4% (Tables 2 and 3).

Table 2. Intra-day precision, accuracy and recovery ($n = 5$) for phenobarbital

C_{nominal} $\mu\text{g/mL}$	Mean c_{found} $\mu\text{g/mL}$ (\pm S.D.)	CV %	Bias %	Recovery % (\pm S.D.)
2.00	1.64 \pm 0.25	15.4	-17.8	95.9 \pm 19.2
5.00	5.12 \pm 0.50	9.8	2.4	98.4 \pm 8.5
32.00	32.88 \pm 2.23	6.8	2.7	102.4 \pm 6.8
64.00	59.69 \pm 1.24	2.1	-6.7	101.0 \pm 2.1

Table 3. Inter-day precision, accuracy and recovery (n = 5) for phenobarbital

<i>C_{nominal}</i> <i>µg/mL</i>	<i>Mean C_{found}</i> <i>µg/mL</i> (<i>± S.D.</i>)	<i>CV %</i>	<i>Bias %</i>	<i>Recovery %</i> (<i>± S.D.</i>)
2.00	2.14±0.24	11.4	6.8	136.4±16.0
5.00	5.50±0.69	12.6	10.1	100.5±9.0
32.00	32.70±2.69	8.2	2.2	98.1±3.6
64.00	63.22±2.17	3.4	-1.2	99.0±4.2

CONCLUSIONS

The proposed method provides accuracy and precision for quantitative determination of phenobarbital in human plasma. The simple sample preparation by protein precipitation, the selected MS transition for monitoring and a very short time of chromatographic analysis allows a specific and efficient determination of a large number of plasma samples in a short time. This high-throughput method is suitable for therapeutic drug monitoring or pharmacokinetic investigations of phenobarbital.

EXPERIMENTAL SECTION

Reagents

Phenobarbital was reference standard from Sigma-Aldrich (Sigma-Aldrich Chemie GmbH, Munich, Germany). Acetonitril, acetic acid and methanol were Merck products (Merck KGaA, Darmstadt, Germany). Distilled, deionised water was produced by a Direct Q-5 Millipore (Millipore SA, Molsheim, France) water system. The human blank plasma was supplied by the Local Bleeding Centre Cluj-Napoca, Romania.

Standard solutions

A stock solution of phenobarbital with concentration of 10 mg/mL was prepared by dissolving appropriate quantity of reference substance in 10 mL acetonitril. A working solution was obtained by diluting a specific volume of stock solution with plasma. Then this was used to spike different volumes of plasma blank, providing finally seven plasma standards with the concentrations ranged between 2.00 and 80.00 µg/mL. Accuracy and precision of the method was verified using plasma standards with concentrations of 2.00, 5.00, 32.00 and 64.00 µg/mL phenobarbital.

Chromatographic and mass spectrometry systems and conditions

The HPLC system was an 1100 series model (Agilent Technologies) consisted of a binary pump, an in-line degasser, an autosampler, a column thermostat, and an Ion Trap VL mass spectrometer detector (Bruker Daltonics GmbH, Germany). Chromatograms were processed using QuantAnalysis software. The detection of phenobarbital was MS/MS using an electrospray

negative ionisation (ESI negative). The monitored ion transition was from the m/z 231.1 ion to m/z 187.9 ion. Chromatographic separation was performed at 45 °C on a Zorbax SB-C18 100 mm x 3 mm i.d., 3.5 μ m column (Agilent Technologies), protected by an in-line filter.

Mobile phase

The mobile phase consisted of a mixture of 0.1% acetic acid and acetonitrile (70:30 (v/v)), each component being degassed, before elution, for 10 min in an Elma Transsonic 700/H (Singen, Germany) ultrasonic bath. The pump delivered the mobile phase at 1 mL/min.

Sample preparation

Standard and test plasma samples were prepared as follows in order to be chromatographically analyzed. In an Eppendorf tube 0.2 mL plasma were mixed with 0.6 mL methanol. The tube is vortex-mixed for 10 s and then centrifuged for 6 min at 5000 rpm. A volume of 0.15 mL of supernatant is transferred in an autosampler vial and 1 μ l was injected into the HPLC system.

Method validation

Method validation involves verifying specificity [6,7], by using six different plasma blanks obtained from healthy human volunteers who did not take before phenobarbital and any other medication. The linearity of the peak area against standard concentration was verified between 2.00-80.00 μ g/mL phenobarbital by applying least-squares linear regression. The applied calibration model was: $y = a \cdot x + b$, $1/y$ weight, where y is peak area and x , concentration. Distribution of the residuals (% difference of the back-calculated concentration from the nominal concentration) was investigated. The calibration model was accepted, if the residuals were within $\pm 20\%$ at the lower limit of quantification and within $\pm 15\%$ at all other calibration levels and at least 2/3 of the standards meet this criterion.

The limit of quantification was established as the lowest calibration standard with an accuracy and precision less than 20%. The intra- and inter-day precision (expressed as coefficient of variation %, CV%) and accuracy (relative difference % between found and theoretical concentration, bias%) of the assay procedure were determined by the analysis in the same day of three samples at each of three levels of concentration in the considered concentration range and one sample of each in three different days, respectively. The recoveries at each of previous levels of concentration were measured by comparing the response of the treated plasma standards with the response of standards in water with the same concentration in phenobarbital as the final extract from plasma standards.

ACKNOWLEDGMENTS

This work was supported by the project CEEEX-ET code 121/2005 financed by CNCSIS Romania.

REFERENCES

1. M.J. Brodie, M.A. Dichter, *Seizure*, **1997**, 6(3), 159.
2. S.G. Paibir, W.H. Seine, *J. Chromatogr. B*, **1997**, 691, 111.
3. H. Kanazawa, Y. Konishia, Y. Matsushimaa, T. Takahashib, *J. Chromatogr. A*, **1998**, 797, 227.
4. M. Moriyama, S. Yamashita, H. Domoto, K. Furuno, H. Araki, Y. Gomita, *J. Chromatogr. B*, **1999**, 723, 301.
5. R.H. Costa Queiroza, C. Bertuccib, W.R. Malfara, S.A. Carvalho Dreossi, A. Rodrigues Chaves, D.A. Rodrigues Valerio, M.E. Costa Queiroz, *J. Pharm. Biomed. Anal.*, **2008**, 48(2), 428.
6. U. S. Department of Health and Human Services, Food and Drug Administration, Center for Drug Evaluation and Research. Guidance for Industry. Bioavailability and Bioequivalence Studies for Orally Administrated Drug Products – General Considerations, Rockville, USA, **2003**, <http://www.fda.gov/cder/guidance/index.htm>.
7. The European Agency for the Evaluation of Medicinal Products. Note for Guidance on the Investigation of Bioavailability and Bioequivalence, London, UK, **2001** (CPMP/EWP/QWP/1401/98).
8. D. Mihi, L. Vlase, S. Imre, C. M. Mihi, M. Achim, D. L. Muntean, *Studia Universitatis Babeş-Bolyai, Chemia*, **2009**, 54(3), 151.
9. M. Achim, D. Muntean, L. Vlase, I. Bâldea, D. Mihi, S. E. Leucuța, *Studia Universitatis Babeş-Bolyai, Chemia*, **2009**, 54(3), 7.
10. A. Butnariu, D. S. Popa, L. Vlase, M. Andreica, D. Muntean, S. E. Leucuta, *Revista Româna de Medicina de Laborator*, **2009**, 15(2), 7.
11. D. S. Popa, L. Vlase, S. E. Leucuța, F. Loghin, *Farmacia*, **2009**, 57(3), 301.

CU(II) COMPLEXES WITH N-SUBSTITUTED SULFONAMIDES

ADRIANA HANGAN^a, JOAQUIN BORRAS^b, LUMINITA OPREAN^a

ABSTRACT. The paper reports the synthesis, physical and chemical characterization of two complexes with Cu(II) and N-substituted sulfonamide as ligands:

[Cu(*N*-(5-ethyl-1,3,4-thiadiazol-2-yl)-4-methylbenzenesulfonamidate)₂(ethylenediamine)] (1) and [Cu(*N*-[5-(ethylsulfanyl)-1,3,4-thiadiazol-2-yl]benzenesulfonamidate)₂(H₂O)₃] (2). The structures of complexes were confirmed by elemental analysis, IR, UV-Vis spectroscopy, magnetic measurements and electronic paramagnetic resonance (EPR) spectra. Correlations of the results obtained from physico-chemical investigations afford the assignment of the most probable structural formulae for the metal complexes. The ligands act as monodentate, coordinating the metal ion geometry through a single N_{thiadiazole} atom. The complex 1 present a square-planar and the complex 2 present a slightly distorted square pyramidal geometry.

Keywords: copper(II) complexes, sulfonamides N-substituted

INTRODUCTION

The study of N-substituted heterocyclic sulfonamide ligands shown their ability to coordinate biologically important metallic ions. The pharmacological activity and the chelating properties of sulfonamides allow the synthesis of metallic complexes with various therapeutic activities, which serve as models for metalloenzymes. Studies have shown that copper(II) complexes with N-substituted sulfonamides as ligands can be used as potential "chemical nucleases". The aromatic rings in the structure of these ligands can be intercalated between the bases of the DNA chain. The cleavage of the DNA chain is a result of the complex interaction with the DNA bases and the formation of ROS (due to the presence of Cu(II)) [1-5].

Taking into consideration these aspects, in this paper we report the synthesis and characterization of two Cu(II) complexes with *N*-(5-ethyl-1,3,4-thiadiazol-2-yl)-4-methylbenzenesulfonamide (HL1) and *N*-[5-(ethylsulfanyl)-1,3,4-thiadiazol-2-yl]benzenesulfonamide (HL2). The ethylenediamine molecule as bidentate ligand and the water molecule as monodentate ligand also participate to the coordination of Cu(II) in the complex 1 respectively complex 2.

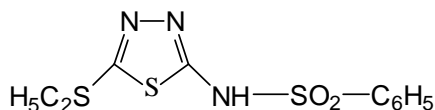
^a Universitatea de Medicina si Farmacie, Facultatea de Farmacie, Str. Ion Creanga Nr. 12, RO- Cluj-Napoca, Romania, acoma6@yahoo.com

^b Universidad de Valencia, Facultad de Farmacia, 46100 Burjassot, Valencia, Spain

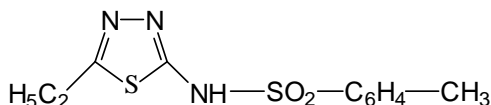
RESULTS AND DISCUSSION

The synthesized ligands (scheme 1) previously reported [2,6] can coordinate various metallic ions through N, S, O atoms present in their molecule. Thus, they can behave like monodentate, bidentate or polydentate ligands. In most cases, the coordination can take place at the two nitrogen atoms of the thiadiazole moiety $N_{\text{thiadiazole}}$, the nitrogen atom of the sulfonamide $N_{\text{sulfonamide}}$, protonated or deprotonated, and even at the sulfur $S_{\text{sulfonamide}}$ or oxygen $O_{\text{sulfonamide}}$ atom from the same sulfonamide moiety. In the majority of the syntheses of metallic complexes, the nitrogen atom of the sulfonamide moiety becomes deprotonated. Through its negative charge it thus contributes to the compensation of the positive charges of the metallic ions which generate the complexes [7,8].

The elemental analyses show that the complexes are type $[\text{Cu}(\text{L}1)_2(\text{ethylenediamine})]$ (complex **1**) and $[\text{Cu}(\text{L}2)_2(\text{H}_2\text{O})_3]$ (complex **2**). The compounds are microcrystalline powders, insoluble in methanol, ethanol, acetone, chloroform and soluble in dimethylformamide and in dimethylsulfoxide. The complexes are stable at room temperature and light.



N-(5-ethyl-1,3,4-thiadiazol-2-yl)-4-methylbenzenesulfonamide (**HL1**)



N-[5-(ethylsulfanyl)-1,3,4-thiadiazol-2-yl]benzenesulfonamide(**HL2**)

Scheme 1

Spectroscopic and magnetic properties

The IR spectra of both complexes present a similar pattern. The most remarkable difference occurs in the band corresponding to the stretching vibration of the thiadiazole ring, which is shifted from 1530 cm^{-1} (HL1) and 1566 cm^{-1} (HL2) in the free ligands to 1482 cm^{-1} (complex **1**) and 1486 cm^{-1} (complex **2**) in the complexes. The characteristic band corresponding to the $\nu(\text{S-N})$ appears at 930 cm^{-1} (complex **1**) and 938 cm^{-1} (complex **2**) shifted towards higher frequencies with respect to those of the uncoordinated ligands. These modifications in the thiadiazole heterocycle and in the sulfonamide

group correspond to the involvement to the N_{thiadiazole} atom in coordination of Cu(II) and to the deprotonation of the sulfonamido moiety [9,10]. This deprotonation will also lead to an electron delocalization involving the atoms of the sulfonamide moiety and the atoms from the thiadiazole ring [11]. There are also modifications of the values of the symmetrical and asymmetrical valence vibrations [$\nu_s(\text{SO}_2)$ and $\nu_{as}(\text{SO}_2)$] for the S=O bond of the sulfonamide moiety, as they too shift to lower frequencies in the complex's IR spectrum (1123 and 1297 cm^{-1} (complex **1**) respectively 1142 and 1300 cm^{-1} (complex **2**)). The IR spectrum of the complex **1** shows an overlap of some other bands on the bands corresponding to the ligands, which makes them difficult to assign. Thus, the characteristic bands of the $-\text{NH}_2$ group of ethylenediamine (2900 cm^{-1} , 1600 cm^{-1} and 1460 cm^{-1}) cannot be distinguished from the sulfonamide ligand bands [12,13].

UV-Vis, EPR and magnetic properties

The solid electronic spectrum of both complexes displays a band near 400 nm (395 nm for complex **1** and 402 nm for complex **2**) assigned to a LMCT transition. The complex **1** exhibits a d-d band at 606 nm and the complex **2** show a d-d band at 669 nm. This band (for complex **2**) is in the 600-850 nm range stated by literature for Cu(II) with square pyramidal geometry, showing a CuN_2O_3 chromophore [14,15].

The presence of ethylenediamine in the complex **1** leads to a stronger separation between the e_g-t_{2g} orbitals of the Cu(II) ion, leading to a shift towards lower wave-lengths for the electron transitions of the metallic ion [14]. This pattern is characteristic for distorted square-planar copper (II) complexes [16].

The polycrystalline X-band EPR spectra of the both complexes are axial. The EPR parameters, obtained by simulation [17] are $g_{\parallel} = 2.135$, $g_{\perp} = 2.075$ and $A_{\parallel} = 180 \times 10^{-4} \text{ cm}^{-1}$ for complex **1** (figure 1) and $g_{\parallel} = 2.22$, $g_{\perp} = 2.09$ and $A_{\parallel} = 150 \times 10^{-4} \text{ cm}^{-1}$ (figure 2) for complex **2**. According to the Bertini classification, the values of A_{\parallel} for complex **1** and complex **2** can be correlated with the structure of the complex [18]. Thus, values between 160 and 200 $\times 10^{-4} \text{ cm}^{-1}$ correspond to a square-planar geometry. The value of A_{\parallel} for complex **1** can be correlated with the geometry of the complex [18]. Values between 130 and 160 cm^{-1} correspond to a square pyramidal or distorted trigonal bipyramidal geometry. As $g_{\parallel} > g_{\perp}$ in the complexes, the unpaired electron must be in the $d_{x^2-y^2}$ (or d_{xy}) orbital [19].

The room temperature magnetic moments of complex **1** ($\mu_{\text{eff}} = 1.72 \text{ MB}$) and for complex **2** ($\mu_{\text{eff}} = 1.83 \text{ MB}$) are consistent with the presence of a single unpaired electron.

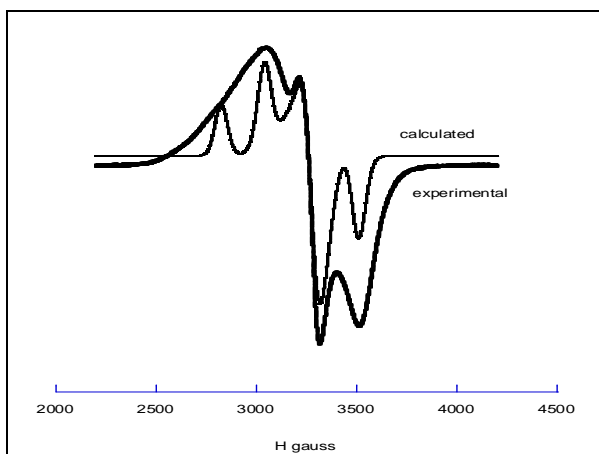


Figure 1. X Band EPR of the compound 1

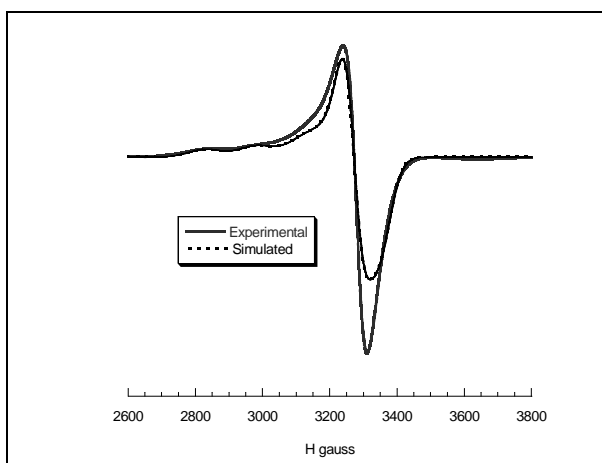
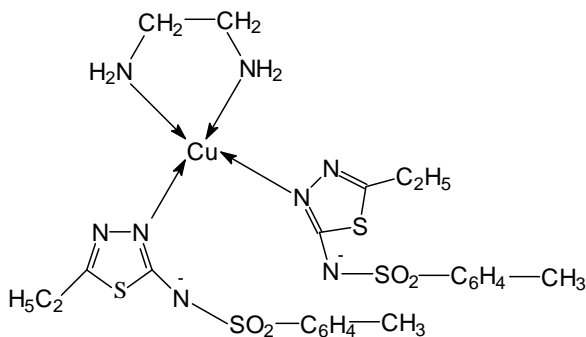


Figure 2. X Band EPR of the compound 2

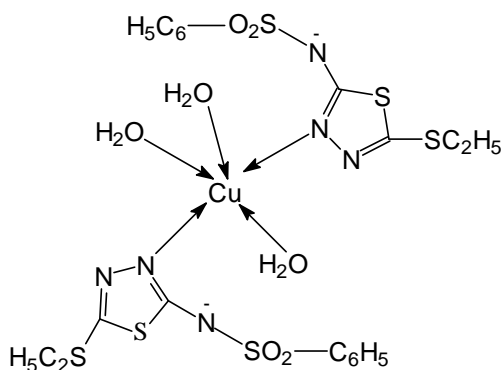
CONCLUSIONS

Two complexes of Cu(II) with sulfonamides N-substituted were synthesized: $[\text{Cu}(\text{L1})_2(\text{ethylenediamine})]$ (complex 1) and $[\text{Cu}(\text{L2})_2(\text{H}_2\text{O})_3]$ (complex 2). The results offered by distinct methods for structural characterization of the complexes (i.e. elemental analysis, spectral (IR, UV-Vis, EPR) and magnetic determinations) together with the crystallographic data available for other mononuclear copper (II) complexes containing the same N-substituted sulfonamide ligands (HL1 and HL2) [2,6] allowed us to propose the structural formulae shown in figure 3. The capacity of DNA cleavage by

copper-sulfonamides complexes is of considerable interest because of their potential use as "chemical nucleases" and thus, as chemotherapeutic and antiviral agents.



Complex 1 – [Cu(L1)₂(ethylenediamine)]



Complex 2 – [Cu(L2)₂(H₂O)₃]

Figure 3. The proposed structure of two complexes C1 and C2

EXPERIMENTAL SECTION

Materials and physical measurements

Copper chloride dihydrate, copper acetate monohydrate and ethylenediamine were purchased from commercial sources. All reagents used were of analytical grade. The two ligands (HL1 and HL2) used for the synthesis of the complexes were synthesized by our group.

Elemental analysis (C, N, H, S) were performed on a Perkin-Elmer device, using the combustion technique. IR spectra were recorded with a Perkin-Elmer FT-IR 1730 spectrophotometer using powder samples in KBr disks, in the 4000-400 cm^{-1} range. Fast ion bombardment (FAB) mass spectra were obtained on a VG Autospec spectrometer in m-nitrobenzene as a solvent. Diffuse reflectance spectra (nujol mulls) were carried out on a Shimadzu UV-2101 PC spectrophotometer. Magnetic susceptibilities were measured at room temperature with the Faraday MSB-MKI balance. $\text{Hg}[\text{Co}(\text{NCS})_4]$ was used as susceptibility standard. Electronic paramagnetic resonance (EPR) spectra were performed at room temperature with a Bruker ELEXSYS spectrometer operating at the X-band frequency.

Synthesis of the ligands

N-(5-ethyl-1,3,4-thiadiazol-2-yl)-4-methylbenzenesulfonamide (**HL1**) and *N*-[5-(ethylsulfanyl)-1,3,4-thiadiazol-2-yl]benzenesulfonamide (**HL2**)

The two ligands were obtained and characterized as previously reported by our group [2,19].

Synthesis of the complexes

[*Cu*(*N*-(5-ethyl-1,3,4-thiadiazol-2-yl)-4-methylbenzenesulfonamidate)₂(ethylenediamine)] (**1**)

1 mmol of the ligand (HL1) is dissolved in 40 ml of methanol. To this solution is added 1 mmol of $\text{CuCl}_2 \cdot 2\text{H}_2\text{O}$ and the mixture is stirred until the copper salt is completely dissolved, forming a green solution. 0.5 mmol of ethylenediamine are added dropwise. The solution turns to blue, forming a violet precipitate (Cu(II)-ethylenediamine complex). The mixture is stirred at room temperature for three hours. The precipitate is then filtered. The filtrate is kept at room temperature in a crystallizer. After four weeks by the slow evaporation of the solvent a blue crystalline powder was obtained. This powder was then filtrated and further crystallized using methanol.

Data for complex **1** (yield 68%).

$\text{C}_{24}\text{H}_{32}\text{CuN}_8\text{S}_4\text{O}_4$ (688): C 42.03 (calc. 41.86); H 4.58 (4.65); N 16.45 (14.27); S 18.93 (18.60)%. IR (KBr) (ν_{max} (cm^{-1})): 1482 (thiadiazole); 1297, 1123 $\nu(\text{SO}_2)$; 930 $\nu(\text{S-N})$. Solid UV/Vis (λ_{max} (nm)): 395 (LMCT), 606 (d-d).

[*Cu*(*N*-[5-(ethylsulfanyl)-1,3,4-thiadiazol-2-yl]benzenesulfonamidate)₂(H_2O)₃] (**2**)

1 mmol of HL2 ligand is dissolved in a mixture of 40 ml methanol. Separately, a solution of 0.5 mmol $\text{Cu}(\text{CH}_3\text{COO})_2 \cdot \text{H}_2\text{O}$ and 5 ml of water was prepared. The copper solution is added to the ligand solution under continuous stirring. The resulting mixture is stirred at room temperature for two hours. The resulting light green solution is kept in a crystallizer at room temperature. After a few days, the complex was obtained as a green crystalline powder. This powder was then filtrated and further crystallized using methanol.

Data for complex **2** (yield 65%).

C₂₀H₂₆CuN₆S₆O₇ (718): C 33.18 (calc. 33.42); H 3.54 (3.62); N 11.38 (11.69); S 27.03 (26.74)%. IR (KBr) (ν_{\max} (cm⁻¹)): 1486 (thiadiazole); 1300, 1142 ν (SO₂); 938 ν (S–N). Solid UV/Vis (λ_{\max}) (nm): 402(LMCT), 669 (d-d).

ACKNOWLEDGEMENT

The authors are thankful for the financial support offered by research grants CNCSIS 1467 and PN II 61-003.

REFERENCES

1. B. Marcias, I. Garcia, M.J. Villa, M. Gonzalez-Alvarez, J. Borrás, A. Castineiras, *Journal of Inorganic Chemistry*, **2003**, 96, 367.
2. A. Hangan, J. Borrás, M. Liu-Gonzalez, L. Oprean, *Z. Anorg. Allg. Chem.*, **2007**, 633, 1837.
3. M. Gonzalez-Alvarez, G. Alzuet, J. Borrás et al., *Journal of Biological Inorganic Chemistry*, **2008**, 13, 1249.
4. A.M. Thomas, M. Nethaji, S. Mahadevan et al., *Journal of Inorgani Biochemistry*, **2004**, 98, 1087.
5. J. L. Garcia-Gimenez, G. Alzuet, M. Gonzalez-Alvarez, M. Liu-Gonzalez, A. Castineiras, J. Borrás, *Journal of Inorganic Biochemistry*, **2009**, 103, 243.
6. A. Hangan, J. Borrás, M. Liu-Gonzalez, L. Oprean, *Revista de Chimie*, **2009**, 60, 755.
7. M. Gonzalez-Alvarez, G. Alzuet, J. Borrás, M. Pitie, B. Meunier, *Journal of Biological Inorganic Chemistry*, **2003**, 8, 644.
8. B. Marcias, M.V. Villa, B. Gomez, J. Borrás, G. Alzuet, M. Gonzalez-Alvarez, A. Castineiras, *Journal of Bioinorganic Chemistry*, **2007**, 101, 441.
9. M. Gonzalez-Alvarez, G. Alzuet, J. Borrás, L. Castillo de Agudo, S. Garcia-Granada, J.M. Montejo-Bernardo, *Journal of Inorganic Biochemistry*, **2004**, 98, 189.
10. J. Casanova, G. Alzuet, S. Ferrer, J. Latorre, J.A. Ramirez, J. Borrás, *Inorganica Chimica Acta*, **2000**, 304, 170.
11. C.A. Otter, S.M. Couchman, J.C. Jeffery, K.L.V. Mann, E. Psillakis, M.D. Ward, *Inorganica Chimica Acta*, **1998**, 278, 178.
12. M.J. Begley, P. Hubberstey, J. Stroud, *Polyhedron*, **1997**, 16, 805.
13. G. Alzuet, S. Ferrer, J. Borrás, R. Martinez-Manez, *Polyhedron*, **2000**, 19, 725.
14. A.B.P Lever, "Inorganic Electronic Spectroscopy", Elsevier, New York, **1984**, 356.
15. I. Beloso, J. Borrás, J. Castro, J. A. Garcia-Vazquez, P. Perez-Lourido, J. Romero, A. Sousa, *European Journal of Inorganic Chemistry*, **2004**, 3, 635.

16. B.J. Hathaway, "Comprehensive Coordination Chemistry", Pergamon Press, Inc, New -York, **1987**, chapter 9.
17. WINEPR-Simfonia 1.25. (1994-1996) Bruker Analytik GmbH: Kalsruhe.
18. I. Bertini, R. Drago, "ESR and NMR of Paramagnetic Species in Biological and Related System", Springer, Boston, **1980**.
19. E. Colacio, J.P. Costes, R. Kivekas, J.P. Laurant, J. Ruiz, M. Sundberg, *Journal of Inorganic Chemistry*, **1991**, 30, 1475.

COMPUTATIONAL DESCRIPTION OF PEPTIDE ARCHITECTURES BASED ON HYDROGEN BONDS

RADU SILAGHI-DUMITRESCU^a

ABSTRACT. The geometrical structures of systems whose architectures rely entirely on hydrogen bonds, such as α -helical polypeptides, are not always properly described with current computational methods.

Keywords: *peptide, density functional, semiempirical, Hartree-Fock, hydrogen bond*

INTRODUCTION

Computational examination of enzyme mechanisms employing such methods as density functional theory (DFT) or Hartree-Fock (HF) has traditionally been restricted, especially in metalloproteins containing transition metal ions, to smaller-size models of the active sites, due to the large computing resources required.[1-5] In recent years, the use of accurate solvation models and QM/MM-type techniques have allowed for the influence of the protein environment to be taken into account more explicitly, albeit with treatment of the less-relevant parts of the polypeptide at levels of theory inferior to those applied to the active site models.[1-5] Additionally, there have been constant efforts to improve the performance of the 'lower-level' theory levels (semiempirical, molecular mechanics) so that they can be applied not just to the distant polypeptide regions, but also to the actual active site.[6-9] At the current rate of increase in computer performance, it is not unfeasible to consider that in the near future it will be possible to apply DFT or (post-)HF methods to enzyme models consisting of the entire protein. Already at the present stage, single-point energies have occasionally been computed for entire protein models at higher levels, such as DFT.[9-21] It is in this context that the present study seeks to estimate the performance of some of the commonly used computational models in predicting accurate geometries of polypeptide chains. For some of these methods, this is likely to be a particularly challenging situation. First, polypeptide architectures tend to rely primarily on weak, non-covalent, interactions (mainly hydrogen bonding). Second, those methods requiring parametrization may not necessarily perform efficiently if

^a *Universitatea Babeș-Bolyai, Facultatea de Chimie și Inginerie Chimică, Str. Kogălniceanu Nr. 1, RO-400084 Cluj-Napoca, Romania, rsilaghi@chem.ubbcluj.ro*

they have not been parametrized for proteins; given the unexpected structural and reactivity findings occasionally uncovered by experiment, even properly parametrized methods may in principle fail in some cases.

RESULTS AND DISCUSSION

Shown in Figure 1 and Table 1 are the results of geometry optimizations on the decaglycine helix. At the HF/3-21G** level, the computed geometry appears funnel-shaped as opposed to the purely helical starting point. Although 1:1 peptide CO---HN hydrogen bonds appear conserved, they are distorted (decreased C-O-H and N-H-O angles, by up to 47°) and elongated by at least 0.1-0.4 Å in terms of the N---O distance and 0.2-0.5 Å in term of the O-H distance) compared to the canonical structure. It is also notable that the parameters listed in Table 1 for the HF geometry vary significantly between the six peptide bonds involved in CO---HN hydrogen bonding, while there would be no such differences in a canonical helix. This HF geometry to our knowledge has no known equivalent in experimental chemistry.

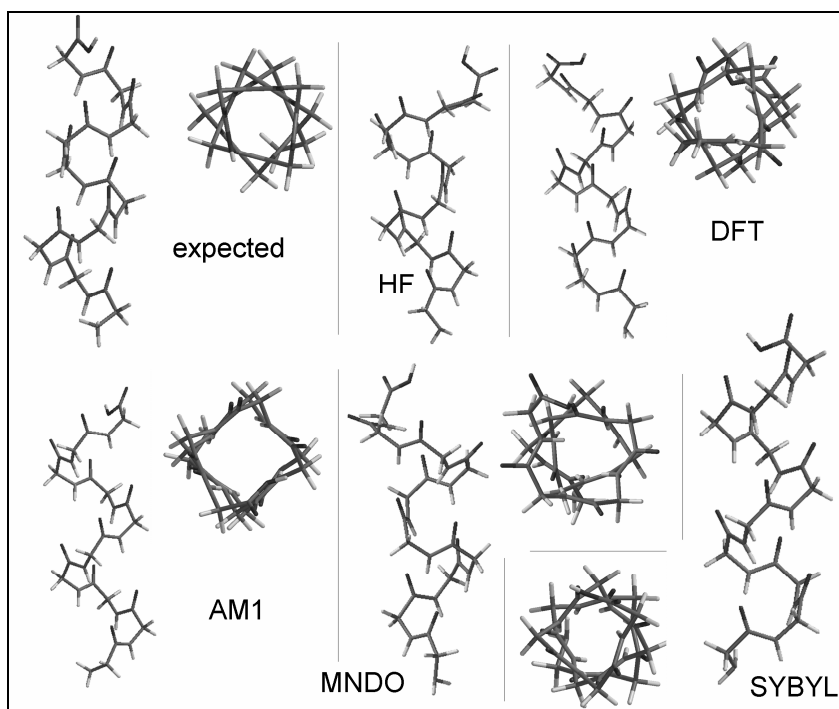


Figure 1. Canonical form of an alpha-helical deca-glycine, compared to geometries obtained by geometry optimization with various computational methods. (side-views and top views).

In the BP86/6-31G** geometry the regularity of the helix is also lost, and the resulting geometry is in-between the canonical form of Figure 1 and the artefactual HF discussed above. Thus, the CO---HN hydrogen bonds feature O-H distances ranging from 2.01 to 2.63 Å, i.e. both irregular and inappropriately long; they are also distinctly less linear (by up to 40°) than in a canonical helix.

Table 1. Key geometrical parameters (distances in Å, angles in °) for the deca-glycine model and its computed geometries at various theory levels. Values are given for each peptide bond starting from the N-terminus of the peptide; the internal parameters of the peptide bonds (C=O, N-H and OC-NH bond lengths) are given as averages since they do not vary significantly (i.e., by more than 0,01 Å) within a model computed with a given method.

Parameter	expected	Sybyl	MNDO	AM1	BP86	HF
O---H	1.72	2.40	3.31	2.33	2.01	2.20
	1.72	2.40	3.18	2.28	2.12	1.94
	1.72	2.50	3.25	2.37	2.09	2.03
	1.72	2.51	3.22	2.43	2.15	2.05
	1.72	2.41	3.23	2.16	2.63	1.93
	1.72	2.45	3.30	2.52	2.67	2.11
	1.72	2.45	3.30	2.52	2.67	2.11
HN---O	2.74	3.17	4.30	2.96	2.98	3.16
	2.74	3.26	4.17	3.13	3.13	2.93
	2.74	3.26	4.23	3.15	3.08	2.99
	2.74	3.43	4.19	3.08	3.06	3.00
	2.74	3.40	4.21	3.15	3.36	2.90
	2.74	3.27	4.28	3.04	3.71	2.87
N-H---O	169°	133°	171°	151°	153°	164°
	169°	143°	169°	142°	167°	171°
	169°	133°	167°	134°	160°	161°
	169°	153°	166°	122°	146°	160°
	169°	171°	167°	172°	128°	164°
	169°	139°	166°	112°	167°	132°
C-O---H	168°	134°	146°	145°	121°	155°
	168°	135°	145°	150°	150°	158°
	168°	138°	139°	142°	132°	142°
	168°	134°	137°	145°	137°	152°
	168°	142°	138°	161°	135°	153°
	168°	121°	136°	120°	137°	122°
C=O	1.22	1.22	1.23	1.25	1.24	1.22
N-H	1.03	1.00	1.02	1.00	1.03	0.99
OC-NH	1.32	1.35	1.38	1.38	1.36	1.34

The PM3 (semiempirical) implementation examined here leads to an entirely non-helical geometry (not shown). Figure 1 and Table 1 show that the MNDO method performs somewhat better than the PM3, even though the hydrogen bonds are still elongated by ~ 2 Å compared to the canonical alpha helix. The AM1 method yields a funnel-type geometry similar to that of HF/3-21G**, and featuring a distinct loss of hydrogen-bond regularity, with the O-H distances at least 0.6 Å longer than in the canonical alpha-helical structure. When using the SYBYL forcefield, the O-H 'hydrogen-bonding' distances were also overestimated by >0.8 Å and the C=O---HN linearity was completely lost.

CONCLUSIONS

No two computational methods yield the same geometry for a decaglycine helix, and none of these geometries correctly reproduces the canonical alpha-helical structure expected and in fact used as a starting point in the respective computations; the origin of these differences is most likely in the different degrees of accuracy with which these computational methods describe hydrogen bonds (and weak interactions in general); all of the methods tested here distinctly underestimate the strength of the hydrogen bonds, predicting O---H distances larger by up to 2 Å than expected, and N-H---O or CO---H angles by up to 40-50° smaller than expected. The methods employed here are often used in computational studies of large-scale systems; our results appear to point out to intrinsic deficiencies of all these methods in quantitatively describing systems whose architecture relies considerably on weak interactions.

MATERIALS AND METHODS

The present study employs an alpha-helical model in order to estimate and compare the performance of several levels of theory in providing accurate geometries. The methods tested here include Hartree-Fock (HF/3-21G**[22]) density functional (BP86/6-31G**[22]) semiempirical (MNDO[22], AM1[22], PM3[23]) and molecular mechanics (SYBYL[22]) applied with standard convergence criteria as defined in the respective software packages (Spartan[22] and Gaussian98[23] respectively); similar results, not discussed here, were obtained with the newer M05 functional as implemented in Gaussian03.[24] Figure 1 shows the canonical form expected for an alpha-helical stretch of decaglycine. This model is built within the Builder module of the Spartan software package,[22] capped with hydrogen atoms (i.e., C-terminal COOH, N-terminal -NH₂) and not subjected to any further modifications. Characteristic for this structure is the regularity imposed by hydrogen bonds formed between C=O and NH groups of different peptide bonds. The length of the helix (free carboxy atom to free amino group) is 15.4 Å, and other parameters are listed

in Table 1. This model was then subjected to geometry optimization at various levels of theory, as detailed above. A zwitterionic version of this helix (capped with ammonium and carboxylate groups, respectively) as well as a 20-alanine helix were also examined with qualitatively similar results, and are not discussed further.

ACKNOWLEDGMENTS

Funding from the Romanian Ministry of Education and Research, (grants PN II 565/2007 and Parteneriate-FLUORODENT) and from the Romanian Academy (63/2007) is gratefully acknowledged.

REFERENCES

1. Noodleman, L.; Lovell, T.; Han, W. G.; Li, J., Himo, F. *Chem Rev*, **2004**, *104*, 459.
2. Siegbahn, P. E.,Blomberg, M. R. A. *Chem. Rev.*, **2000**, *100*, 421.
3. Harris, D. L. *Curr. Opin. Chem. Biol.*, **2001**, *5*, 724.
4. Friesner, R. A.,Dunietz, B. D. *Acc. Chem. Res.*, **2001**, *34*, 351.
5. Gooding, S. R.; Winn, P. J.; Jones, G. A.; Ferenczy, G. G.; Frusher, M. J., Reynolds, C. A. *J. Phys. Chem. A.*, **2006**, *110*, 6487.
6. Silaghi-Dumitrescu, R. *Rev. Chim.*, **2004**, *55*, 304.
7. Tejero, I.; Gonzalez-Lafont, A., Lluch, J. M. *J Comput Chem*, **2007**, *28*, 997.
8. McNamara, J. P.; Sundararajan, M.; Hillier, I. H.; Ge, J.; Campbell, A., Morgado, C. *J Comput Chem*, **2006**, *27*, 1307.
9. McNamara, J. P.; Sundararajan, M., Hillier, I. H. *J Mol Graph Model*, **2005**, *24*, 128.
10. Csontos, J.; Palermo, N. Y.; Murphy, R. F., Lovas, S. *J Comput Chem*, **2008**, *29*, 1344.
11. Sulpizi, M.; Raugei, S.; VandeVondele, J.; Carloni, P., Sprik, M. *J Phys Chem B*, **2007**, *111*, 3969.
12. Jensen, K. P. *J Inorg Biochem*, **2006**, *100*, 1436.
13. Sundararajan, M.; Hillier, I. H., Burton, N. A. *J Phys Chem A*, **2006**, *110*, 785.
14. Machonkin, T. E.; Westler, W. M., Markley, J. L. *Inorg Chem*, **2005**, *44*, 779.
15. Vrajmasu, V. V.; Munck, E., Bominaar, E. L. *Inorg Chem*, **2004**, *43*, 4867.
16. Kennepohl, P., Solomon, E. I. *Inorg Chem*, **2003**, *42*, 696.
17. Vrajmasu, V. V.; Bominaar, E. L.; Meyer, J., Munck, E. *Inorg Chem*, **2002**, *41*, 6358.
18. Glaser, T.; Rose, K.; Shadle, S. E.; Hedman, B.; Hodgson, K. O., Solomon, E. I. *J Am Chem Soc*, **2001**, *123*, 442.
19. Sigfridsson, E.; Olsson, M. H., Ryde, U. *Inorg Chem*, **2001**, *40*, 2509.

20. Kloiber, K.; Weiskirchen, R.; Krautler, B.; Bister, K., Konrat, R. *J Mol Biol*, **1999**, 292, 893.
21. Nayal, M., Di Cera, E. *J Mol Biol*, **1996**, 256, 228.
22. Spartan 5.0, Wavefunction, Inc., 18401 Von Karman Avenue Suite 370, Irvine, CA 92612 U.S.A.
23. Gaussian 98 (Revision A.1), M. J. Frisch, G. W. Trucks, H. B. Schlegel, G. E. Scuseria, M. A. Robb, J. R. Cheeseman, V. G. Zakrzewski, J. A. Montgomery, R. E. Stratmann, J. C. Burant, S. Dapprich, J. M. Millam, A. D. Daniels, K. N. Kudin, M. C. Strain, O. Farkas, J. Tomasi, V. Barone, M. Cossi, R. Cammi, B. Mennucci, C. Pomelli, C. Adamo, S. Clifford, J. Ochterski, G. A. Petersson, P. Y. Ayala, Q. Cui, K. Morokuma, D. K. Malick, A. D. Rabuck, K. Raghavachari, J. B. Foresman, J. Cioslowski, J. V. Ortiz, B. B. Stefanov, G. Liu, A. Liashenko, P. Piskorz, I. Komaromi, R. Gomperts, R. L. Martin, D. J. Fox, T. Keith, M. A. Al-Laham, C. Y. Peng, A. Nanayakkara, C. Gonzalez, M. Challacombe, P. M. W. Gill, B. G. Johnson, W. Chen, M. W. Wong, J. L. Andres, M. Head-Gordon, E. S. Replogle and J. A. Pople, Gaussian 98 (Revision A.1), Gaussian, Inc., Pittsburgh PA, 1998.
24. Gaussian 03, Revision C.02, Frisch, M. J.; Trucks, G. W.; Schlegel, H. B.; Scuseria, G. E.; Robb, M. A.; Cheeseman, J. R.; Montgomery, Jr., J. A.; Vreven, T.; Kudin, K. N.; Burant, J. C.; Millam, J. M.; Iyengar, S. S.; Tomasi, J.; Barone, V.; Mennucci, B.; Cossi, M.; Scalmani, G.; Rega, N.; Petersson, G. A.; Nakatsuji, H.; Hada, M.; Ehara, M.; Toyota, K.; Fukuda, R.; Hasegawa, J.; Ishida, M.; Nakajima, T.; Honda, Y.; Kitao, O.; Nakai, H.; Klene, M.; Li, X.; Knox, J. E.; Hratchian, H. P.; Cross, J. B.; Bakken, V.; Adamo, C.; Jaramillo, J.; Gomperts, R.; Stratmann, R. E.; Yazyev, O.; Austin, A. J.; Cammi, R.; Pomelli, C.; Ochterski, J. W.; Ayala, P. Y.; Morokuma, K.; Voth, G. A.; Salvador, P.; Dannenberg, J. J.; Zakrzewski, V. G.; Dapprich, S.; Daniels, A. D.; Strain, M. C.; Farkas, O.; Malick, D. K.; Rabuck, A. D.; Raghavachari, K.; Foresman, J. B.; Ortiz, J. V.; Cui, Q.; Baboul, A. G.; Clifford, S.; Cioslowski, J.; Stefanov, B. B.; Liu, G.; Liashenko, A.; Piskorz, P.; Komaromi, I.; Martin, R. L.; Fox, D. J.; Keith, T.; Al-Laham, M. A.; Peng, C. Y.; Nanayakkara, A.; Challacombe, M.; Gill, P. M. W.; Johnson, B.; Chen, W.; Wong, M. W.; Gonzalez, C.; and Pople, J. A.; Gaussian, Inc., Wallingford CT, 2004.

Zn-Ni ALLOY COATINGS FROM ALKALINE BATH CONTAINING TRIETHANOLAMINE. INFLUENCE OF ADDITIVES

LIANA MARIA MUREȘAN^{a,*}, JULIEN EYMARD^b,
DIANA BLEJAN^a, EMIL INDREA^c

ABSTRACT. The Zn-Ni alloys have been electrodeposited from an alkaline bath containing triethanolamine as complexing agent for Ni²⁺ ions. Polyethyleneglicol (PEG), in combination with either coumarin, piperonal or vanillin have been tested as brightening agents. Their effect on the codeposition process and on the corrosion resistance of the resulted coatings was investigated. Under the examined conditions, the electrodeposition was of anomalous type. The effect of plating bath conditions on the corrosion resistance was studied by Tafel polarization measurements. It was found that the tested compounds had a beneficial effect both on deposits quality and on their corrosion resistance.

Keywords: zinc - nickel alloys, electrodeposition, corrosion, triethanolamine

INTRODUCTION

Zn-Ni alloys replace successfully cadmium coatings in the automotive industry [1] and provide superior sacrificial protection to steel than pure zinc since they corrode more slowly. Moreover, adhesion of chromate onto Zn-Ni alloy is superior to zinc.

Zinc-nickel can be plated from acid [2-12] or alkaline noncyanide solutions [13-21]. Although Ni is nobler than Zn, the codeposition of Zn-Ni in both cases is anomalous and Zn is present in a higher percent than Ni in the final deposit [2].

The acid bath typically gives a higher Ni content than the alkaline one (*i.e.* 10-14% vs. 6-9 %), with high current efficiency, but the distribution of the plated alloy is poor. In contrast, alkaline electrodeposition is less efficient, but gives more uniform plating in both thickness and alloy composition [14]. Moreover, alkaline baths are non-corrosive.

Basic alkaline baths usually contain Zn²⁺ and Ni²⁺ ions, an alkali metal hydroxide and a complexing agent for nickel, such as polyethyleneimine [13, 21], di-, or triethylenetriamine [14], N,N'-bis(3-amino-propyl)ethylenediamine [14], tetraethylenepentamine [14], triethanolamine [19, 20, 22], tartrate [15], ammonia [17-18] etc.

^a "Babes-Bolyai" University, Department of Physical Chemistry, 11 Arany Janos St., 400028 Cluj-Napoca, ROMANIA. * E-mail: limur@chem.ubbcluj.ro

^b IUT Rouen, FRANCE

^c INCDTIM Cluj-Napoca, 65-103 Donath Str., RO-400293 Cluj-Napoca, ROMANIA

Electrodeposited Zn–Ni alloys exhibit three main phases: the α -phase, which is a solid solution of zinc in nickel with an equilibrium solubility of about 30% Zn, the γ -phase, an intermediate phase with a composition $\text{Ni}_5\text{Zn}_{21}$ and the η -phase, which is a solid solution of nickel in zinc with a very low amount of nickel [23].

The use of additives in electrodeposition baths is extremely important due to their influence on the growth and structure of the cathodic deposits [24]. They influence the physical and mechanical properties of the coatings as well as their chemical composition and their corrosion resistance.

In this context, the aim of this work is to investigate the effect of piperonal, coumarin and vanillin in combination with polyethyleneglicol (PEG) on Zn-Ni electrodeposition from an alkaline bath containing triethanolamine.

X ray diffraction (XRD) was used for determination of phase structure of the deposits and electrochemical measurements were carried out in order to characterize their corrosion behavior by using Tafel method.

RESULTS AND DISCUSSION

Electrodeposition

Table 1 presents the results of the visual observation made on Zn-Ni electrodeposits obtained in the absence or in the presence of different additives.

Table 1. Effect of additives on the visual aspect of the alloy deposit. Electrolyte: ZnO 15 g/l + NaOH 130 g/l + $\text{NiSO}_4 \cdot 6 \text{H}_2\text{O}$ 6 g/l + Triethanolamine (TEA) 80 g/l (pH 14); $i = 40 \text{ mA/cm}^2$; $t = 35 \text{ min}$; $t^0 = 20 \pm 2^\circ\text{C}$.

No.	Additives	Aspect of the deposit
1	-	dark grey, rough, mat
2	3 ml/l PEG +1 mg/l piperonal	grey, semi bright
3	3 ml/l PEG + 1 mg/l coumarin	grey, semi bright
4	3 ml/l PEG +1 mg/l vanillin	grey, uniform, smooth
5	3 ml/l PEG +5 mg/l vanillin	grey, uniform, semi bright
6	3 ml/l PEG +10 mg/l vanillin	light grey, uniform, bright

It was observed that the most leveled and bright deposits were obtained in presence of the combination of PEG and vanillin and, as expected, the brightness of the deposits increased with the vanillin concentration. All additives improved the quality of the deposits in terms of adherence, grain size and homogeneity.

Corrosion measurements

Linear polarization tests in a potential range of $\pm 200 \text{ mV}$ vs. the open circuit potential (ocp) have been made employing the Zn-Ni coated steel electrodes obtained in presence of different additives (Figure 1). PEG was used in all cases as a “carrier”. “Carriers” are compounds with large molecules suffering rapid adsorption - desorption that are usually used in conjunction with compounds having small molecules and suffering specific adsorption at the electrodic interface, in order to obtain leveled and bright metallic deposits [24].

As can be observed, the Zn-Ni alloy becomes nobler than zinc (the corrosion potential is shifted in the positive direction) and hence, the corrosion rate of alloy is hindered. At the same time, the deposit remains still sacrificial with respect to steel.

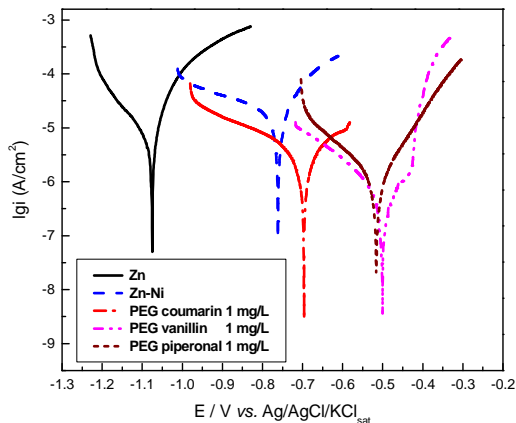


Figure 1. Polarization curves for Zn-Ni coated steel obtained from a bath containing different additives. Experimental conditions: electrolyte Na_2SO_4 0.2 g/l (pH 5); scan rate, 0.166 mV/s; PEG concentration, 3 ml/l.

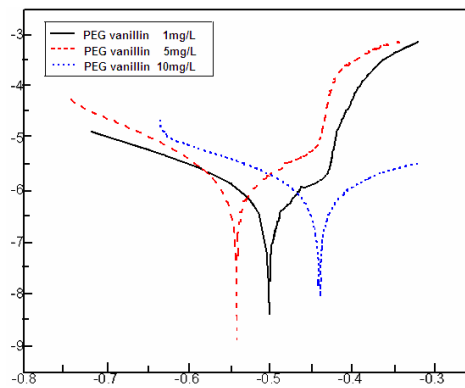


Figure 2. Polarisation curves for Zn-Ni coated steel obtained from a bath containing different concentrations of vanillin. Experimental conditions: electrolyte Na_2SO_4 0.2 g/l (pH 5); scan rate, 0.166 mV/s; PEG concentration, 3 ml/l.

The addition of additives gives rise to significant decreases of corrosion current densities as compared to Zn and Zn-Ni obtained without additives. This indicates that, as expected, the investigated organic compounds strongly modified the quality of the cathodic deposit in terms of structure and morphology, producing more compact, fine-grained and consequently more corrosion resistant coatings.

For a given additive (e.g. vanillin) the effect depends on the compound concentration (Figure 2). However, the dependence of the corrosion current density on the additive concentration in the plating bath is not monotone, probably due to the fact that in every electrodeposition process, there is an optimal additive concentration for which the deposit quality is the best [25]. This aspect should be investigated in more details in the future.

The values of the corrosion parameters of the coatings prepared in the absence and in the presence of additives were calculated from the polarization curves by using the Stern - Geary theory [26] and Tafel interpretation and are presented in Table 2.

As can be seen from Table 2, the additives shift the corrosion potential towards more positive values and decrease the corrosion current with about one order of magnitude. When used in concentration of 1 mg/l in combination with PEG, coumarin and vanillin led to similar results concerning the corrosion rate,

but the deposits obtained in the presence of vanillin present higher polarization resistance than those obtained in the presence of coumarin and were brighter.

Table 2. Parameters of the corrosion process of the Zn and Zn-Ni coatings

Parameters	Zn	Zn-Ni	Zn-Ni+PEG	Zn-Ni + PEG		Zn-Ni + PEG		
			+coumarin	+ piperonal	+ vanillin	+ vanillin		
			1mg/l	1mg/l	5mg/l	1mg/l	5mg/l	10mg/l
$i_{corr}(A/cm^2)$	5.80E-06	1.68E-06	3.44E-07	1.68E-06	1.00E-06	3.34E-07	4.95E+0	4.07E-07
$b_c(V/dec)$	0.034	0.074	0.040	0.085	0.118	0.056	0.034	0.053
$b_a(V/dec)$	0.084	0.047	0.050	0.112	0.048	0.046	0.038	0.005
$R_p(Ohm)$	438	441	911	618	9976	6948	3315	4865
$E_{corr}(mV)$	-1075	-761	-622	-516.0	-530	-501	-541	-438
V_{corr} (mm/year)	1.16E-01	2.51E-02	5.13E-03	2.51E-02	1.49E-02	4.98E-03	7.38E-03	6.05E-03

* b_a and b_c are the anodic and cathodic activation coefficients, respectively.

XRD analysis

In order to put on evidence the formation of Zn-Ni alloy by electrodeposition and to correlate the electrochemical results with the structural data of the coatings, XRD investigations were carried out on the coated steel electrodes obtained with PEG and 1 mg/l of different additives (Figure 3).

The XRD patterns of the Zn-Ni coatings obtained from a bath containing PEG (3 ml/l) in combination with either piperonal, vanillin or coumarin 1 mg/l (Figure 3) have revealed the formation of the ZnNi cubic alloy, space group P 4/m, PDF card no. 65-3203; $a = 0.295(6)$ nm and $V = 0.259(2)$ nm³. The unit cell parameters and the unit cell volumes of the ZnNi cubic alloy, calculated using the PowderCell software [27] from the whole X-ray diffraction pattern refinement of the above-mentioned Zn-Ni coatings, are presented in the Table 3.

The microstructural parameters, the effective crystallite mean size, D_{eff} (nm) and the mean root square (rms) of the microstrains, ($\langle \epsilon^2 \rangle_m^{1/2}$), of the ZnNi cubic crystalline phase of the Zn-Ni coatings are also presented in Table 3.

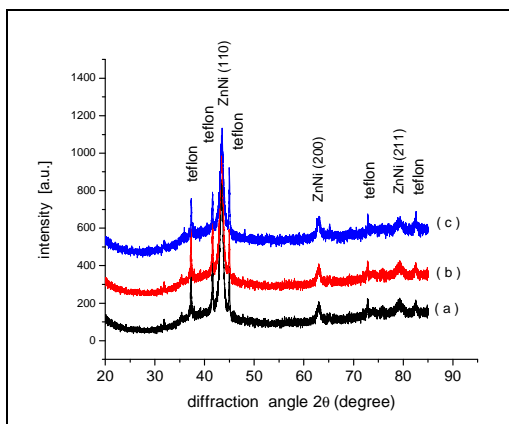


Figure 3. X-ray diffractograms of Zn-Ni coatings obtained from a bath containing PEG (3 ml/l) in combination with piperonal (a), vanillin (b) and coumarin (c) in concentration 1 mg/l.

Table 3. The unit cell parameters, the unit cell volumes of the ZnNi cubic alloy and the microstructural parameters of the Zn-Ni coatings obtained from a bath containing PEG (3 ml/l) in combination with piperonal (a), vanillin (b) and coumarin (c) in concentration 1 mg/l

Samples	Unit cell parameter a [nm]	Unit cell volume [nm ³]	Effective crystallite mean size Deff (nm)	Rms of the microstrains $\langle \epsilon^2 \rangle^{1/2} \times 10^3$
Zn-Ni + PEG + piperonal	0.2958(2)	0.2588(7)	8.85	5.093
Zn-Ni + PEG + vanillin	0.2955(6)	0.2581(9)	8.45	4.574
Zn-Ni + PEG + coumarin	0.2957(7)	0.2587(4)	9.62	2.424

The nanostructured Zn-Ni coatings prepared in the presence of additives piperonal and vanillin showed a smaller average size of the crystallites (8.6 nm), than the nanostructured Zn-Ni coatings prepared in the presence of coumarin (9.6 nm). At the same time, the lattice microstrain $\langle \epsilon^2 \rangle^{1/2}$ of nanostructured Zn-Ni coatings prepared in the presence of piperonal and vanillin shows a larger value of the intercrystallite zones that suggests a higher interaction between the nanoparticles of the coating and the steel support and, consequently, a higher corrosion resistance of the coatings.

CONCLUSIONS

The Zn-Ni coatings showed an excellent corrosion resistance as compared with conventional Zn coatings obtained from an alkaline bath. Using of additives allowed obtaining more corrosion resistant Zn-Ni deposits than in their absence.

The best corrosion behavior was exhibited by the coatings obtained in the presence of PEG in combination with piperonal or with vanillin, which presented a smaller average size of the crystallites than the nanostructured Zn-Ni coatings prepared in the presence of coumarin.

EXPERIMENTAL SECTION

Electrodeposition

The electrodeposition of the Zn-Ni coatings was carried out in a two compartments glass cell, with the capacity of 250 ml, using a steel (OL37) disk electrode ($\varnothing = 1\text{cm}$) as working electrode, a Ag/AgCl/KCl_{sat} as reference electrode and a Pt foil as counter electrode. Before electrodeposition, the working electrode was wet polished on emery paper of different granulations and finally on felt with a suspension of alumina. Before plating, the electrode was ultrasonicated during 2 minutes, washed with acetone and distilled water in order to remove the impurities from the surface.

The approximately 40 μm thick composite coatings were obtained at a constant current density ($i = 40 \text{ mA/cm}^2$) by using a potentiostat / galvanostat (Voltalab PGP201, Radiometer analytical), during 35 minutes, at room temperature ($25 \pm 2^\circ\text{C}$).

Corrosion measurements

The corrosion measurements were performed with a potentiostat Autolab-PGSTAT 10, (Eco Chemie BV, Utrecht, Netherlands). Before the polarization measurements, the open circuit potential (OCP) was recorded during 1 hour, until it was stabilized.

XRD measurements

The powder X-ray diffraction (XRD) patterns were obtained with a Bruker D8 Advance powder diffractometer working at 40 kV and 40mA, using $\text{CuK}\alpha$ wavelength, with a germanium monochromator. The measurement was performed in the range angle $2\theta=20-85^\circ$ and in a step-scanning mode with a step $\Delta 2\theta = 0.01^\circ$. Pure corundum powder standard sample was used to correct the data for instrumental broadening.

The Warren-Averbach X-ray Fourier analysis [28] of the ZnNi (1 1 0) ($2\theta = 43.42$ degree), ZnNi (2 0 0) ($2\theta = 63.02$ degree) and ZnNi (2 1 1) ($2\theta = 79.22$ degree) cubic ZnNi alloy structure diffraction profiles were used in order to determine the microstructural parameters of the Zn-Ni coatings (the effective crystallite mean size, D_{eff} (nm) and the mean root square (rms) of the microstrains, $\langle \varepsilon^2 \rangle_m^{1/2}$).

ACKNOWLEDGEMENTS

The financial support within the project PN II INOVARE No. 261/2008 (ZINITECH) is gratefully acknowledged.

REFERENCES

1. N. Zaki, E. Budman, *Products Finishing*, **1991**, 46.
2. P. Ganeshan, S.P. Kumaraguru, B.N. Popov, *Surface & Coatings Technology* **2007**, *201*, 7896.
3. M.M. Abou Krishna, F.H. Assaf, A.A. Toghan, *Journal of Solid State Electrochemistry*, **2007**, *11*, 244.
4. C.E. Lehmborg, D.B. Lewis, G.W. Marshall, *Surface & Coatings Technology* **2005**, *192*, 269.
5. M.M. Abou-Krishna, *Applied Surface Science* **2005**, *252*, 1035.
6. B.D. Bammel, *US. Patent* 4597838, Cl. C25D 356, **1986**.
7. M. Eyraud, Z. Hanane, J. Crousier, *Surface & Coatings Technology* **1994**, *67*, 35.

8. V. Ravindran, V.S. Muralidharan, *Bulletin of Materials Science* **2006**, 29, 293.
9. Z. Wu, L. Fedrizzi, P.L. Bonora, *Surface & Coatings Technology*, **1996**, 85, 170.
10. M.M. Abou-Krishna, A.M. Zaky, A.A. Toghan, *Asian Journal of Biochemistry* **2006**, 1, 84.
11. M. Sider, C. Fan, D.L. Piron, *Journal of Applied Electrochemistry* **2001**, 31, 313.
12. V. Ravindran, V.S. Muralidharan, *Portugaliae Electrochimica Acta* **2007**, 25, 391.
13. W. Schwartz, W.H. Berkowitz, B.E. Esquenet, *US Patent* 3681211, Cl. C23b 5/32, **1972**.
14. C. Müller, M. Sarret, M. Benballa, *Journal of Electroanalytical Chemistry* **2002**, 519, 85.
15. M.G. Hosseini, H. Ashassi-Sorkabi, H.A.Y. Ghiasvand, *Surface & Coatings Technology* **2008**, 202, 2897.
16. G.D. Wilcox, D.R. Gabe, *Corrosion Science* **1993**, 35, 1251.
17. I. Rodriguez-Torres, G. Valentin, F. Lapique, *Journal of Applied Electrochemistry* **1999**, 29, 1035.
18. V.G. Roev, R.A. Kaidrikov, A.B. Khakimullin, *Russian Journal of Electrochemistry* **2001**, 37, 756.
19. H.Y. Lee, S.G. Kim, *Surface & Coatings Technology* **2000**, 135, 69-74.
20. L.S. Tsybul'skaya, T.V. Gaevs'kaya, O.G. Purovs'kaya, T.V. Byk *Surface & Coatings Technology* **2008**, 203, 234.
21. K. Oshima, T. Murai, H. Sakurai, S. Igarashi, H. Hanagata, H. Igarashi *US Patent* 4889602, Cl. C25D 3/56, **1989**.
22. M.S. Chandrasekar, S. Srinivasan, M. Pushpavanam, *Journal of Solid State Electrochemistry* **2009**, 13, 781.
23. D.E. Hall, *Plating & Surface Finishing* **1983**, 70, 59.
24. O. Kardos, D.G. Foulke, "Applications of mass transfer theory. Electrodeposition on small-scale profiles" in *Advances in Electrochemistry and Electrochemical Engineering*; Tobias, Ch. W.; Ed.; Publisher: Interscience New York, NY, **1966**; Vol. 2, pp. 145.
25. L.M. Muresan, S.C. Varvara, "Leveling and Brightening mechanisms in Metal Electrodeposition" in *Metal Electrodeposition*, Ed. M. Nunez, Nova Science Publishers, Inc. New York, **2005**, chapter 1.
26. M. Stern, A. L. Geary, *Journal of Electrochemical Society* **1957**, 104, 56.
27. W. Kraus, G. Nolze, *Journal of Applied Crystallography* **1996**, 29, 301.
28. N. Aldea, E. Indrea, *Computer Physics Communications* **1990**, 60, 155.

MODELING OF BIOLOGICALLY ACTIVE MOLECULAR STRUCTURES

ERIKA TASNADI^a, GABRIEL KATONA^a, MIRCEA V. DIUDEA^a

ABSTRACT. In view of finding the best relationship between biological activity and structure using topological indices, a QSAR/QSPR study was performed on a set of 44 benzodiazepin-derivatives. In a similarity test, the highest scored structures were submitted to mono and multi linear regression analysis and the optimal model was drawn out. The activity of several newly designed by us structures, belonging to the same class of molecules, was predicted with the use of the title model.

Keywords: *molecular modeling, biological activity, QSAR-QSPR*

INTRODUCTION

The projection of molecular structures with desired physico-chemical or biological properties is one of the major goals of Molecular Topology. The identification of the crucial factors involved in the structure-property relationship is gained by the comparative analysis of a set of molecules. This analysis is realized by the aid of topological descriptors (indices) [1] and regression analysis, included in various algorithms. The topological characterization of the chemical structures allows their classification based on similarity criteria.

A bioactive molecule interacts with a biological receptor within an *effector-receptor complex*, in which the two partners mutually accommodate their structures and energies such that the resulting complex exists sufficiently long for generating a biological response. The structural features of the bioactive molecules, responsible for a given biological activity (i.e. pharmacological profile), are called *pharmacophore*. It plays an essential role in the recognition process preceding the complex formation. The receptor (i.e. a situs in a biomacromolecule) must contain complementary features to the pharmacophore for the recognition (complexation and ultimately biological response) to occur. In addition to the pharmacophore and its complementary atoms, the effector and biomacromolecule present *areas of nonspecific interactions*, which modulate the biological response.

^a Faculty of Chemistry and Chemical Engineering, "Babes-Bolyai" University, Arany Janos Str. 11, 400084, Cluj, Romania, diudea@chem.ubbcluj.ro

Several 2D- and 3D-QSAR approaches are performed to model the receptor-drug interaction, with ultimate aim the drug design. A quantitative structure-activity relationship (QSAR) correlates the changes in the observed biological activity with the changes in the chemical structure of a series of molecules.

Quantitative Structure–Property Relationship (QSPR) and Quantitative Structure–Activity Relationship (QSAR) studies [2] give a simple and reasonable support for predicting physico-chemical and biological properties. A QSPR/QSAR study looks for connections that link directly the molecular structure to the properties of the chemical compounds [1,2]. By the aid of structural descriptors / topological indices (calculated on molecular graphs), various mathematical models are developed to relate quantitatively the molecular structures and their physico-chemical or biological properties.

This method is inductive and the errors are minimized, verified and validated statistically.

The current methods to quantify the similarity [3] of two or more molecules take into consideration three types of the molecular structure description:

- Topological- by means of molecular graphs
- Configurational- using of atomic coordinates in 3D space
- Quantum mechanic- using data on molecular fields, energy levels of molecular orbitals, etc.

The present report is structured as follows: after an introductory part (see above), the “Method” introduces to the procedure used for optimization and calculation of the indices. The “Results and Discussion” present the results and comments the performance of the used method.

METHOD

The following procedure was used to find the best relationship between structures and biological property:

1. structures are optimized to find a minimum-energy (stable) configuration (HYPER CHEM version 7.52)
2. an index database is generated by using DRAGON 5.0 software [4]
3. an exhaustive search to find the best equation (with the correlation coefficient $R > 0.90$), by STATISTICA 6.0, software
4. prediction of biological property for newly designed structures

Thus, before computing the indices, it is important to find a minimum-energy (stable) configuration for a molecular system, especially for 3D-type descriptors. We used for geometry optimization the molecular mechanics method MM+, with the Polak-Ribière conjugate gradient, at RMS lower than 0.009.

The next step was the calculation of indices. The initial database contained 1630 indices which were generated by using Dragon software. From each descriptor block (as provided by DRAGON), the indices showing the best correlation coefficient in monovariate regression against the biological activity, were collected out.

The statistical analysis was performed by using the STATISTICA software package. The procedure to find the best model for the prediction of the biological activity follows the below steps 1-3:

1. search for the best monovariate regression
2. search for the best bi- and tri-variate regression
3. prediction of biological activity based on the best regression equation, of the form: $y_i = a + \sum_j b_j x_{ij}$ where b_j are regression coefficients, a is a constant, y_i is the dependent variable (e.g., the modeled property, $\log IC_{50}$) and x_{ij} are the independent variables (in particular, topological indices), $j=1,2,\dots,m$ for the molecular structures $i, i=1,2,\dots,n$.

RESULTS AND DISCUSSION

Structure of benzodiazepine derivatives [5]

Benzodiazepines (BZs) play an important role in medicinal chemistry, e.g. as a nucleus for combinatorial synthesis. The benzodiazepines caught the interest of scientists because of their putative role in mammalian central nervous system and for their exceptional tolerance; they form an important class of therapeutic agents with wide-spread applications in the treatment of anxiety and emotional disorders.

In our investigation, we used the set of classical 1,4-BZs derivatives listed in **Table 1**, having the general formula shown in **Figure 1**. The six substituent positions are R^7 and R^8 in A-ring, R^1 and R^3 in B-ring, and R^2 and R^6 in the C-ring.

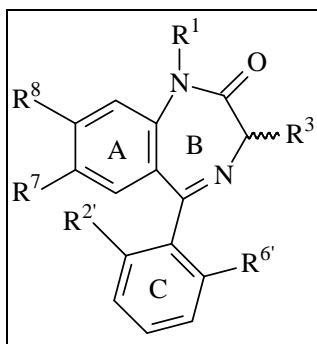


Figure 1. Classical 1,4-BZs

Table 1. Benzodiazepine derivatives and their binding affinities (log IC₅₀)

ID	Name	R ⁷	R ¹	R ²	R ⁶	R ³	R ⁸	log IC ₅₀
1	Ro 05-3061	F	H	H	H	H	H	1.602
2	Ro 05-4865	F	CH ₃	H	H	H	H	1.230
3	Ro 05-6820	F	H	F	H	H	H	0.869
4	Ro 05-6822	F	CH ₃	F	H	H	H	0.708
5	Nordazepam	Cl	H	H	H	H	H	0.973
6	Diazepam	Cl	CH ₃	H	H	H	H	0.908
7	Ro 05-3367	Cl	H	F	H	H	H	0.301
8	Delorazepam	Cl	H	Cl	H	H	H	0.255
9	Ro 07-9957	I	CH ₃	F	H	H	H	0.462
10	Ro 05-2904	CF ₃	H	H	H	H	H	1.114
11	Ro 14-3074	N ₃	H	F	H	H	H	0.724
12	Nitrazepam	NO ₂	H	H	H	H	H	1.000
13	Ro 05-4435	NO ₂	H	F	H	H	H	0.176
14	Flunitrazepam	NO ₂	CH ₃	F	H	H	H	0.580
15	Clonazepam	NO ₂	H	Cl	H	H	H	0.255
16	Ro 05-4082	NO ₂	CH ₃	Cl	H	H	H	0.342
17	Ro 05-3590	NO ₂	H	CF ₃	H	H	H	0.544
18	Ro 20-7736	NHOH	CH ₃	F	H	H	H	1.982
19	Ro 05-3072	NH ₂	H	H	H	H	H	2.587
20	Ro 05-4318	NH ₂	CH ₃	H	H	H	H	2.663
21	Ro 20-1815	NH ₂	CH ₃	F	H	H	H	1.813
22	Ro 05-4619	NH ₂	H	Cl	H	H	H	1.875
23	Ro 05-4528	CN	CH ₃	H	H	H	H	2.580
24	Ro 20-2541	CN	CH ₃	F	H	H	H	1.477
25	Ro 20-2533	CH ₂ CH ₃	H	H	H	H	H	1.556
26	Ro 20-5747	CH=CH ₂	H	H	H	H	H	1.380
27	Ro 20-5397	CHO	H	H	H	H	H	1.633
28	Ro 20-3053	COCH ₃	H	F	H	H	H	1.255
29	Ro 05-2921	H	H	H	H	H	H	2.544
30	Ro 05-4336	H	H	F	H	H	H	1.322
31	Ro 05-4520	H	CH ₃	F	H	H	H	1.146
32	Ro 05-4608	H	CH ₃	Cl	H	H	H	0.580
33	Ro 07-4419	H	H	F	F	H	H	1.279
34	Ro 07-3953	Cl	H	F	F	H	H	0.204
35	Ro 07-4065	Cl	CH ₃	F	F	H	H	0.613
36	Ro 07-5193	Cl	H	Cl	F	H	H	0.477
37	Ro 22-3294	Cl	H	Cl	Cl	H	H	0.845
38	Ro 07-5220	Cl	CH ₃	Cl	Cl	H	H	0.740
39	Ro 13-3780	Br	CH ₃	F	F	H	H	0.380
40	Ro 07-6198	H	H	F	F	H	Cl	1.447
41	Ro 20-8895	H	H	F	H	H	CH ₃	1.279
42	Ro 22-6762	Cl	CH ₃	H	H	H	Cl	1.602
43	Ro 20-8065	Cl	H	F	H	H	Cl	0.556
44	Ro 20-8552	CH ₃	H	F	H	H	Cl	1.146

Table 2 presents the symbol and description of the indices which show the best correlation with the biological property. In Table 3 the values of these descriptors are presented.

Table 2. Topological indices: the meaning of descriptors (DRAGON 5.0).

Symbol	Descriptor meaning	Descriptor block
EEig04d	E igenvalue 04 from e dge adj. matrix weighted by d ipole moments	Edge adjacency indices
nNH ₂	N umber of primary amines (aliphatic)	Functional group counts
XMOD	M odified Randic connectivity index	Connectivity indices
Hy	H ydrophilic factor	Molecular properties
IC0	I nformation c ontent index (neighborhood symmetry of 0 -order)	Information indices
MATS3e	M oran autocorrelation – lag 3 / weighted by a tomic S anderson e lectronegativities	2D autocorrelation
BIC0	B ond information c ontent (neighborhood symmetry of 0 -order)	Information indices
S0K	K ier s ymmetry index	Topological descriptors
RDF045 m	R adial d istribution f unction – 4.5 / weighted by atomic m asses	RDF descriptors
G1	G ravitational index G1	Geometrical descriptors
H1m	A utocorrelation of lag 1 / weighted by atomic m asses	Getaway descriptors

The best obtained monovariate equation was:

$$y=8.72-0.73 \times \text{EEig04d} \quad (1)$$

$$R= 0.7310; s= 0.47; F= 48.19; n= 44$$

where: R - is the correlation coefficient; s - standard error of estimate; F - Fisher's statistics and n- number of molecules and the best bivariate equation:

$$y= 7.95+0.426 \times \text{Hy}-0.61 \times \text{EEig04d} \quad (2)$$

$$R= 0.8378; s= 0.38; F= 48.25; n= 44$$

Because the statistics of correlation (eqs. 1 and 2) were not satisfactory, we used the program CLUJSIMIL [6,7] to cluster the structures of more than 95 percent similarity with respect to the reference structure (denoted by us RS), by choosing the molecule with the highest log IC₅₀, namely Ro 05-4435 (structure 13).

Table 3. Topological indices: values in the studied BZs

#	EEig 04d	nNH ₂	XMOD	Hy	IC0	MATS 3e	BIC0	S0K	RDF 045m	G1	H1m
1	2.465	0	57.729	-0.776	1.618	-0.082	0.304	66.597	3.439	26.97	1.336
10	2.605	0	66.381	-0.717	1.747	-0.016	0.322	79.771	5.59	34.187	1.592
11	2.529	0	67.832	-0.672	1.739	-0.103	0.315	81.164	5.948	34.1	1.25
12	2.515	0	64.226	-0.704	1.669	-0.092	0.306	73.418	4.563	31.23	1.309
13	2.749	0	67.556	-0.672	1.819	-0.133	0.333	82.794	6.404	35.314	1.351
14	2.767	0	70.335	-0.686	1.782	-0.108	0.321	85.44	6.729	37.611	1.285
15	2.756	0	69.865	-0.672	1.819	-0.134	0.333	82.794	11.126	38.472	1.385
16	2.772	0	72.644	-0.686	1.782	-0.104	0.321	85.44	11.452	40.827	1.313
17	2.914	0	76.208	-0.632	1.932	-0.074	0.348	96.605	9.597	50.247	1.419
18	2.547	0	67.465	-0.260	1.724	-0.058	0.312	81.164	5.739	34.856	1.226
19	2.226	1	57.152	0.349	1.517	-0.022	0.281	64.062	3.54	26.703	1.146
2	2.611	0	60.508	-0.787	1.587	-0.051	0.292	69.309	3.765	29.153	1.262
20	2.333	1	59.93	0.319	1.49	0.025	0.271	66.812	3.866	28.878	1.09
21	2.535	1	63.261	0.338	1.642	-0.054	0.299	75.733	5.77	32.699	1.129
22	2.473	1	62.791	0.368	1.676	-0.079	0.311	73.113	10.115	33.208	1.222
23	2.533	1	63.223	0.291	1.466	0.086	0.262	69.595	4.186	30.254	1.065
24	2.589	1	66.553	0.340	1.61	-0.004	0.288	78.402	6.11	34.182	1.097
25	2.392	0	60.091	-0.836	1.406	0.075	0.255	65.621	4.028	27.872	1.083
26	2.237	0	60.091	-0.836	1.417	0.048	0.258	68.042	3.606	27.732	1.14
27	2.571	0	60.798	-0.787	1.531	-0.001	0.282	70.613	3.59	28.099	1.297
28	2.678	0	67.628	-0.762	1.639	-0.048	0.295	79.763	6.379	33.731	1.158
29	2.043	0	54.5	-0.818	1.453	0.041	0.273	60.112	3.324	24.648	1.138
3	2.688	0	61.059	-0.738	1.713	-0.127	0.322	75.992	5.344	30.775	1.379
30	2.4	0	57.83	-0.776	1.618	-0.049	0.304	69.13	5.229	28.217	1.181
31	2.528	0	60.609	-0.787	1.587	-0.019	0.292	71.733	5.554	30.416	1.124
32	2.535	0	62.918	-0.787	1.587	0.013	0.292	71.733	10.224	32.94	1.162
33	2.592	0	61.16	-0.738	1.713	-0.104	0.322	71.992	6.197	31.178	1.266
34	2.714	0	66.699	-0.704	1.869	-0.162	0.351	78.874	10.665	34.867	1.653
35	2.724	0	69.477	-0.717	1.831	-0.133	0.337	81.608	10.991	37.183	1.568
36	2.716	0	69.008	-0.704	1.869	-0.163	0.351	83.074	15.454	37.931	1.687
37	2.717	0	71.317	-0.704	1.777	-0.169	0.334	78.874	20.478	39.523	1.767
38	2.727	0	74.096	-0.717	1.747	-0.128	0.322	81.608	20.804	41.935	1.683
39	2.698	0	74.674	-0.717	1.831	-0.121	0.337	81.608	8.115	41.412	2.061
4	2.699	0	63.838	-0.750	1.68	-0.1	0.31	78.556	5.669	33.017	1.305
40	2.748	0	66.699	-0.704	1.869	-0.162	0.351	78.874	7.78	34.411	1.591
41	2.549	0	60.193	-0.787	1.587	-0.047	0.292	71.733	5.198	29.847	1.124
42	2.635	0	68.457	-0.750	1.68	0.039	0.31	76.011	9.947	34.013	1.741
43	2.785	0	69.008	-0.704	1.869	-0.087	0.351	83.074	11.28	35.793	1.878
44	2.767	0	65.832	-0.750	1.741	-0.09	0.321	78.556	7.363	33.545	1.363
5	2.472	0	60.038	-0.776	1.618	-0.06	0.304	66.597	7.792	27.883	1.528
6	2.619	0	62.817	-0.787	1.587	-0.018	0.292	69.309	8.118	30.095	1.441
7	2.701	0	63.368	-0.738	1.779	-0.115	0.334	75.992	9.697	31.831	1.569
8	2.708	0	65.678	-0.738	1.713	-0.115	0.322	75.992	14.367	34.831	1.603
9	2.632	0	76.54	-0.750	1.741	-0.034	0.321	78.556	10.551	41.728	2.515

Table 4 lists the similarity data of the structures.

The structures bellow 90 percent of similarity are out of our interest and, after rejecting them from the table, 38 structures remained. Next, we performed mono- and multiple- regressions to find the best models.

Table 4. Similarity coefficients with respect to the reference structure (Ro 05-4435)

MolID	Similarity	MolID	Similarity
13	1.00000	25	0.92442
10	0.99968	26	0.92415
38	0.99941	27	0.92093
15	0.99862	22	0.92004
18	0.99842	20	0.91980
39	0.99744	41	0.91945
28	0.99740	8	0.91785
35	0.99663	32	0.91761
24	0.99527	6	0.91760
11	0.99480	7	0.91665
23	0.96508	31	0.91641
14	0.96165	2	0.91640
44	0.96109	33	0.91545
12	0.96103	3	0.91545
16	0.96057	17	0.88737
9	0.96027	19	0.87689
21	0.96027	5	0.87463
37	0.95954	30	0.87340
42	0.95930	1	0.87340
36	0.95838	29	0.82995
43	0.95838		
34	0.95721		
40	0.95721		
4	0.95697		

Monovariate regression:

$$y = 6.14 - 0.66 \times \text{BIC0} \quad (3)$$

R = 0.6626; s = 0.48; F = 28.18; n = 38

Bivariate regression:

$$y = 6.07 + 0.510 \times \text{Hy} - 0.53 \times \text{IC0} \quad (4)$$

R = 0.8248; s = 0.37; F = 37.23; n = 38

To increase even more the correlation coefficient, we have to remove the structures with similarity coefficients bellow 95 percent; thus, only 24 structures remained; on these we performed mono and multi- variate regressions, as above. The best regression equations are:

Monovariate regression:

$$y = 13.61 - 0.83 \times \text{EEig04d} \quad (5)$$

$R = 0.8264$; $s = 0.36$; $F = 47.38$; $n = 24$

Bivariate regression:

$$y = 11.49 - 0.67 \times \text{EEig04d} + 0.281 \times \text{Hy} \quad (6)$$

$R = 0.8587$; $s = 0.34$; $F = 29.48$; $n = 24$

Trivariate regression:

$$y = 10.29 - 1.57 \times \text{Hy} - 0.71 \times \text{IC0} - 1.2 \times \text{nnNH2} \quad (7)$$

$R = 0.8933$; $s = 0.33$; $F = 26.33$; $n = 24$

$$y = 12.32 - 1.79 \times \text{EEig04d} + 2.19 \times \text{Hy} - 3.03 \times \text{IC0} - 1.18 \times \text{nnNH2} \quad (8)$$

$R = 0.9084$; $s = 0.29$; $F = 22.42$; $n = 24$

The plot for the calculated, by the best regression, [equation (8)] vs. observed biological activity is presented in Figure 2.

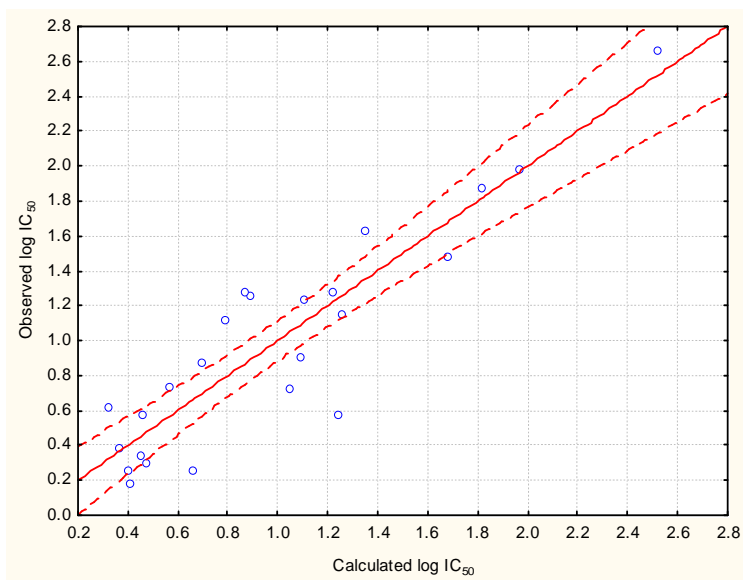
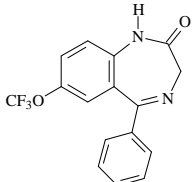
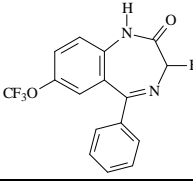
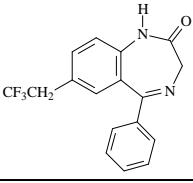
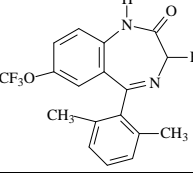
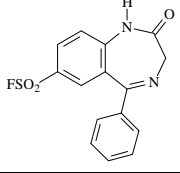
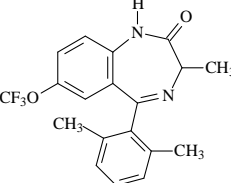
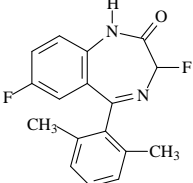


Figure 2. Calculated vs. observed $\log IC_{50}$ for equation 7

Design of new benzodiazepine derivatives

Information on experimental data shows the structures which have the functional groups NO_2 and Cl in position R_7 , as the highest biologically active. For this reason, we tried to build up molecules with the same basic structure of which activities have not been yet measured. These molecules are shown in Table 5.

Table 5. Design of our proposed new structures

No.	Molecule	No.	Molecule
S1.		S5.	
S2.		S6.	
S3.		S7.	
S4.		S8.	

The next step was the calculation of the biological activity for the newly proposed structures by equation (8). The data are presented in Table 7.

Table 7. Calculated indices and evaluated biological activity for the proposed structures (by equation (8)).

Structures	EEig04d	Hy	IC0	nNH ₂	Biological activity (BA)
S1	2.73	-0.69	1.83	0	0.38
S2	2.79	-0.66	1.88	0	0.18
S3	2.87	-0.68	1.81	0	0.21
S4	2.86	-0.72	1.73	0	0.38
S5	2.62	-0.72	1.75	0	0.75
S6	2.70	-0.73	1.72	0	0.68
S7	2.58	-0.67	1.89	0	0.50
S8	2.61	-0.76	1.65	0	0.99

From Table 7, one can see the structures S2, S3, S1, S4 show high biological activity, as those in the initial set of molecules; among these, the structure S2 shows the highest value. For this reason, it could be of interest to synthesize these molecules and make biological activity tests.

Notice that the authors [5] reported a biological activity of 0.176 for the most potent structure, which was taken as the reference structure and denoted RS. In comparing the activity of the above structure with our proposed molecules S2 and S3, we calculated using Hyper Chem software package, the value of log P: RS (-3.34); S2 (2.40) and S3 (0.57). It is known that a positive value of log P indicates a hydrophobic character, which is important in the transport of drugs through the biological membranes up to the receptor. Resuming the above data, our structure S2 appears as very promising in the drug design.

CONCLUSIONS

We studied a set of molecular structures belonging to the class of benzodiazepines for which we obtained a good model for the prediction of log C_{50} biological activity. The best equation (eq. 8) obtained suggests that the biological activity is highly dependent on structure symmetry and hydrophobic characteristics. Based on the proposed model and the original data, we projected eight new structures for which the activity was calculated.

The procedures for model building proved to be reliable in estimating the biological activity and moreover, to predict the values of activity for so far non-tested structures.

ACKNOWLEDGMENTS

The authors wish to thank for the financial support provided from programs co-financed by The SECTORAL OPERATIONAL PROGRAMME HUMAN RESOURCES DEVELOPMENT, Contract POSDRU 6/1.5/S/3 – „Doctoral studies: through science towards society”.

REFERENCES

1. M. V. Diudea, (Ed.), “QSPR/QSAR Studies by Molecular Descriptors”, Nova, New York, **2001**, 438.
2. G. Katona, G. Turcu, A. A. Kiss, O. M. Minailiuc, and M. V. Diudea, “QSAR/QSPR Studies by Cluj and Szeged Descriptors”, *Rev. Roumaine Chim.*, **2001**, *46*, 137.
3. M. Randić, “Design of Molecules with Desired Properties. A Molecular Similarity Approach to Property Optimization. In: Johnson, M. A.; Maggiora, G. M. Eds. “Concepts and Applications of Molecular Similarity”, Wiley, New York, **1990**, Chap. 5, 77-145.
4. R. Todeschini et al., Dragon software, <http://www.taletе.mi.it>.
5. Sung-Sau So and Martin Karplus, “Genetic Neural Networks for Quantitative Structure-Activity Relationships: Improvements and Application of Benzodiazepine Affinity for Benzodiazepine/ GABAA Receptors”, *J. Med. Chem.*, **1996**, *39*, 26.
6. S.H. Bertz and W.C. Herndon, “The Similarity of Graphs and Molecules”. In: Artificial Intelligence Applications in Chemistry, *ACS Symposium Series* 306, Eds.: T. H. Pierce and B. A. Hohne. American Chemical Society, Washington, **1986**, 169–175.
7. O. Ursu, G. Katona, and M. V. Diudea, “Activity prediction by CLUJ-Simil program”, *Rev. Roum. Chim.*, **2003**, *48(4)*, 321.

TECHNICAL ASSESSMENT OF CO₂ CAPTURE USING ALKANOLAMINES SOLUTIONS

ANAMARIA PADUREAN^a, CALIN-CRISTIAN CORMOS^a,
ANA-MARIA CORMOS^a, PAUL-SERBAN AGACHI^a

ABSTRACT: The most promising technology for carbon dioxide removal from coal and natural gas fired power plant flue gases at large scale applications is based on gas – liquid absorption. This paper evaluates the carbon dioxide absorption at low CO₂ partial pressures from flue gases by post-combustion using aqueous solution of alkanolamines e.g., monoethanolamine, diethanolamine, triethanolamine, methyldiethanolamine and diisopropanolamine. The aim of the present paper is to evaluate and compare the energy penalty involved by carbon capture technology using alkanolamines through the following technical coefficients: power consumption, heating agent and cooling agent consumptions. The CO₂ absorption modelling and simulation work described in this paper was developed in ChemCAD software.

Keywords: CO₂ Absorption and Desorption, Alkanolamines, Technical Assessment, Carbon Capture and Storage (CCS)

INTRODUCTION

The most alarming global environmental problems of today are the increase of global temperature and the climate changes. These problems are most likely caused by the increasing atmospheric carbon dioxide concentration due to the burning of fossil fuels from human activity.

Given the advantages of fossil fuels, such as their availability, relatively low cost, and the existing infrastructure for delivery and distribution, they play a major role in the worldwide energy production for at least the next 75 years. On the other hand, combustion of fossil fuels such as coal and natural gas are main sources of CO₂ emissions that, according to the Intergovernmental Panel on Climate Change (IPCC), constitute a major man-made contribution to global warming of our planet.¹

A significant reduction of greenhouse gas emissions (mainly CO₂) resulting from fossil fuels can only be obtained by increasing the efficiency of power plants and production processes, and decreasing the energy demand,

^a Universitatea Babeș-Bolyai, Facultatea de Chimie și Inginerie Chimică, Str. Kogălniceanu, Nr. 1, RO-400084 Cluj-Napoca, Romania, cormos@chem.ubbcluj.ro

combined with CO₂ capture and long term storage (CCS). CO₂ capture and storage is a modern technology approach trying to mitigate the contribution of greenhouse gas emissions resulted from the fossil fuels usage to global warming, based on capturing the carbon dioxide from large point sources such as fossil fuel power plants. The carbon dioxide is then permanently stored away from the atmosphere in suitable geological formations or used for Enhanced Oil Recovery (EOR).²

There are three main CO₂ capture techniques generated from the combustion of fossil fuels: post-combustion capture, pre-combustion capture and oxy-fuel combustion.³ Several possible ways of CO₂ capture technology such as absorption, adsorption, membranes or other physical and biological separation methods are shown in Figure 1.

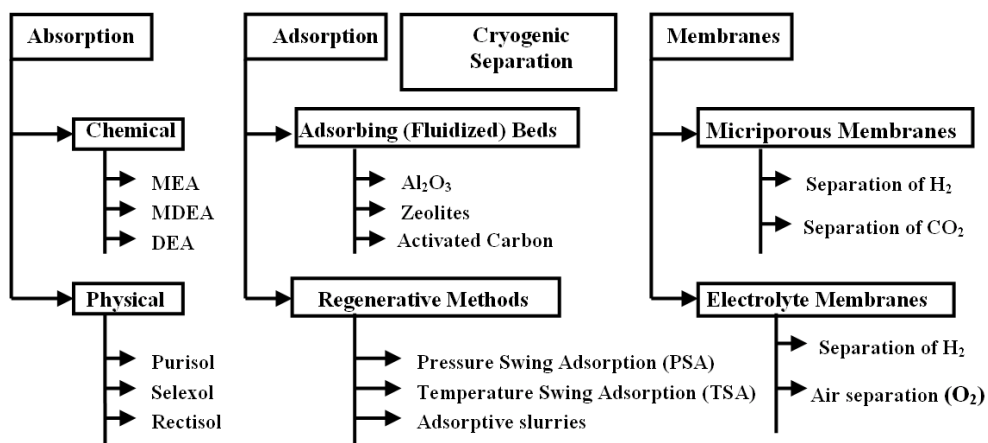


Figure 1. Carbon dioxide capture technologies⁴

Carbon dioxide capture by gas - liquid absorption is one of the common industrial technologies today and, in many cases, has been observed to be the most viable solution, compared to the other processes that are available. However, technological improvements are necessary to reduce the high capital cost and energy requirements of the absorption process. It is expected that process design innovation or the use of better solvents can reduce the capital and energy costs significantly.⁵

As it can be noticed from Figure 1, CO₂ absorption can be divided into chemical absorption (mainly used in post-combustion capture technique) and physical absorption (used in pre-combustion capture technique). In the case of pre-combustion capture technique, where CO₂ partial pressure is relatively high (over 15 bar) and CO₂ concentration is around 40%, it is

recommended to use physical solvents containing for instance methanol (Rectisol[®] process) or dimethyl ethers of polyethylene (Selexol[®]). In the case of post-combustion capture technique, where CO₂ partial pressure is close to atmospheric pressure and CO₂ concentrations are relatively low e.g., 4-8% vol. in natural gas-fired and 12-15% vol. in coal-fired power plants. It is recommended that chemical solvents such as aqueous solutions of alkanolamines, sodium hydroxide (NaOH) or ammonia (NH₃) to be used. No matter what solvent is used for CO₂ capture, the electric power, the heat (steam) and the cooling duties that are required for the capture process are very important aspects that must be considered. From the point of view of electric power consumption, in case of chemical solvents usage, the solvent flow rate is lower than in the case of physical solvents, which means a lower electric power consumption for solvent circulation. The situation is totally reversed for heat consumption; the chemical solvents require much more heat for regeneration than physical solvents due to the chemical reactions involved. These issues require a careful integration analysis in terms of heat and electric power for the CO₂ capture plant.⁶

This paper is focused on post-combustion CO₂ capture by gas – liquid absorption using aqueous alkanolamines because this technology has the highest potential to be implemented on a large scale for CO₂ capture from flue gases (e.g., power generation sector) in the next decade.

It is very important that as a result of the reaction between the CO₂ and solvent, the resulted compounds to be stable enough so that they do not decompose in CO₂ in the absorption column, but can decompose easily in the desorption column with minimal thermal energy consumption. It is also important that the solvent has low volatility in order to avoid losing it with the stream that leaves the absorption column. Considering these circumstances, a comparison between the solvents used for CO₂ absorption: aqueous sodium hydroxide (very strong base), ammonia (too volatile) and alkanolamines (middle alkalinity and low volatility) was made with the conclusion that the most convenient solvents are the alkanolamines. As a result, they were chosen for technical assessment in this paper (quantification of energy penalties involved by carbon capture).⁷

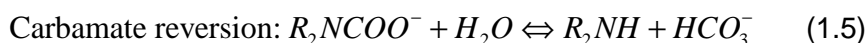
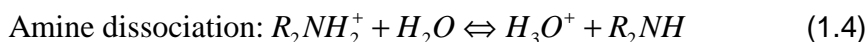
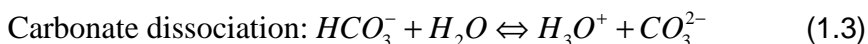
In the present paper are analyzed and compared for the first time the technical coefficients in terms of energy consumption (power, heating duty and cooling duty consumption) of carbon dioxide absorption using five different alkanolamines (monoethanolamine - MEA, diethanolamine - DEA, triethanolamine - TEA, diisopropanolamine - DIPA and methyldiethanolamine - MDEA). The quantification of CO₂ capture energy demand is crucial for the successful implementation of carbon capture and storage technologies in real applications (e.g., in the power generation sector).

RESULTS AND DISCUSSION

Post-combustion CO₂ capture using alkanolamines

The removal of CO₂ by absorption in alkanolamines is widely used in chemical industry (e.g., ammonia synthesis). This process is based on the reversible chemical absorption of CO₂ using an acid - base reaction in an absorption - desorption loop. In the absorber (relatively low temperature and/or high pressure) the acidic gases are absorbed, while in the desorber the loaded solvent is regenerated (elevated temperatures and/or reduced pressure). The alkanolamines that are the most used for this process are: monoethanolamine (MEA), diethanolamine (DEA), triethanolamine (TEA), methyldiethanolamine (MDEA) and diisopropanolamine (DIPA).

The absorption of CO₂ into an alkanolamine solution is a reaction between a weak acid and a weak base, where both are weak electrolytes. The weak electrolytes partially dissociate in aqueous solution. The chemical equilibrium is achieved in liquid phase when CO₂ is absorbed in an aqueous solution of primary or secondary alkanolamines such as MEA (NH₂CH₂CH₂OH), DEA (NH(CH₂CH₂OH)₂), DIPA (NH(CH(CH₃)₂)₂). The equilibrium is described by the following equations where R₂N is an alkyl- or alkanolamine and R can represent an alkyl, alkanol group or hydrogen:

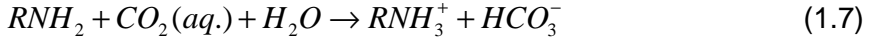


The reaction of CO₂ with primary or secondary alkanolamines (like monoethanolamine or diethanolamine) can be approximated by a single chemical reaction as follow:



The above equation implies that all absorbed CO₂ reacts with the alkanolamine to form carbamate. Equation (1.6) neglects the presence of bicarbonate (HCO₃⁻), hydroxide (OH⁻), and carbonate (CO₃²⁻) ions. The concentration of these ions will be very small in the region of loading. This is of interest to CO₂ capture from fossil fuels burning power plants using a primary or secondary alkanolamine since the area of interest is where the fast carbamate reaction is dominant.

For aqueous solutions of tertiary alkanolamines such as MDEA (CH₃N (C₂H₄OH)₂) or TEA (N(CH₂CH₂OH)₃) equation (1.5) can be neglected since no stable carbamates are formed, thus the main reaction for carbon dioxide absorption process is:



Carbamate is the main product for the reaction of CO₂ with primary and secondary alkanolamines. For aqueous solutions of tertiary alkanolamine, the carbamate stability is low and there, for the main reaction product, is bicarbonate, as seen in equation (1.7).^{3,8}

Results of post-combustion CO₂ capture

The carbon dioxide absorption process was modelled and simulated using the AMINE model from the ChemCAD software. The CO₂ absorption simulation results using various alkanolamines are presented in Table 1.

Table 1. Simulation results

	Case 1	Case 2	Case 3	Case 4	Case 5
Absorbent	MEA	DEA	TEA	DIPA	MDEA
Absorbent mass flow (kg/h)	29·10 ⁵	37·10 ⁵	5·10 ⁸	5·10 ⁸	82·10 ⁵
Initial CO₂ mass flow (kg/h)	3.67·10 ⁵	3.67·10 ⁵	3.67·10 ⁵	3.67·10 ⁵	3.67·10 ⁵
Final CO₂ mass flow to storage (kg/h)	3.32·10 ⁵	3.33·10 ⁵	2.65·10 ⁵	2.65·10 ⁵	3.32·10 ⁵
CO₂ removal ratio (%)	90.48	90.63	72.12	72.23	90.61
Power required (MW_e)	28.02	28.49	-27.23	14.56	28.02
Heating agent duty (MW_{th})	1.27·10 ³	0.25·10 ³	4.90·10 ³	142·10 ³	0.21·10 ³
Cooling agent duty (MW_{th})	1.35·10 ³	0.29·10 ³	5.06·10 ³	12.80·10 ³	0.28·10 ³

As it can be noticed from Table 1, a capture rate of around 90% in most alkanolamines was obtained. This capture rate was calculated reporting the final mass flow CO₂ to the initial mass flow CO₂. Having these results from Table 2 and using the equations below, the technical coefficient for CO₂ absorption in alkanolamines solution was calculated.

$$Power_{required} (MW) = \sum(Ep_{pump}) + \sum(Ep_{compressor}) + \sum(Ep_{engine\ turbine}) (MW) \quad (1.8)$$

$$Heating\ agent_{required} (MW) = \sum(reboiler\ heating\ required) (MW) \quad (1.9)$$

$$Cooling\ agent_{required} (MW) = \sum(heat\ exchanger\ agent) (MW) \quad (1.10)$$

$$X_{coefficient} (MWh/kg_{CO_2\ captured}) = X_{required} (MW) / Final\ CO_2\ captured (kg/h) \quad (1.11)$$

where: X can be electric power (Ep), heating or cooling duties.

Table 3 shows that the best value in all three technical coefficients for CO₂ absorption is the tertiary amine MDEA (methyldiethanolamine). Since this amine is less alkaline than the other four amines, it can be used in a higher concentration (~50%), therefore has a better reactivity.

Table 2. Technical coefficient for CO₂ absorption in alkanolamines solution

Alkanolamine	Energy coefficient (MWh/kg CO ₂)	Heating agent coefficient (MWh/kg CO ₂)	Cooling agent coefficient (MWh/kg CO ₂)
MEA	$8.63 \cdot 10^{-5}$	$3.82 \cdot 10^{-3}$	$4.06 \cdot 10^{-3}$
DEA	$8.62 \cdot 10^{-5}$	$0.81 \cdot 10^{-3}$	$0.83 \cdot 10^{-3}$
TEA	$10.28 \cdot 10^{-5}$	$18.50 \cdot 10^{-3}$	$19.12 \cdot 10^{-3}$
DIPA	$5.49 \cdot 10^{-5}$	$47.75 \cdot 10^{-3}$	$48.32 \cdot 10^{-3}$
MDEA	$8.57 \cdot 10^{-5}$	$0.75 \cdot 10^{-3}$	$0.80 \cdot 10^{-3}$

Another advantage of the methyldiethanolamine is that MDEA does not form carbonates with CO₂, has high resistance to degradation, does not cause corrosion and presents low environmental toxicity.

CONCLUSIONS

Chemical absorption by using alkanolamines solutions is presently considered the most practical and economical method to separate CO₂ from flue gases generated by power sector at near atmospheric pressure. Various solvents are used for the recovery of CO₂ from these gases. The disadvantages of the majority of solvents are that they degrade in the process (thermal degradation, oxidation, forming stable salts with SO_x and NO_x, corrosion etc.), in addition, the desorption process for solvent regeneration requires a great deal of energy in form of heat. If more energy is required for desorption, the total energy demand of the process per unit CO₂ produced will be increasing.

The present paper was devoted to the evaluation of carbon dioxide capture using post-combustion methods and quantification of energy related coefficients (power consumption coefficient, heating agent coefficient, cooling agent coefficient) for CO₂ absorption in five different alkanolamines solution (monoethanolamine, diethanolamine, triethanolamine, methyldiethanolamine and diisopropanolamine). The paper also evaluates the performance of these five alkanolamines.

As it can be seen in the previous paragraph the best alkanolamine for CO₂ absorption is methyldiethanolamine. This tertiary amine can be used in a higher concentration (30-50%) than the other four alkanolamines, it does not form carbonates with CO₂, has high resistance to degradation, it does not cause corrosion and presents low toxicity.

EXPERIMENTAL SECTION

The above paragraph specifies many CO₂ capture techniques, but the present section only deals with the post-combustion capture technique by absorption. The CO₂ is captured from the flue gas after the gasification of coal in a coal power plant.

The CO₂ post-combustion process by absorption technology described in the present paper was modelled and simulated using the AMINE database model from the ChemCAD software. In ChemCAD AMINE model uses the Kent-Eisenberg method. This method is a simplified way to model the reactions (and phase equilibria) in a gas sweetening system. The model can be used in a system where water with one amine is used to treat gas with carbon dioxide, sulfuric acid, and/or ammonia.

For post-combustion capture technique, the CO₂ capture plants that use as solvent alkanolamines consists of an absorption column, a desorption column, drops separators, heat exchangers and stages compressors. A schematic diagram of the equipment used in this work is shown in Figure 2.

Absorption takes place at temperature of about 30 - 45°C and a pressure around to atmospheric (about 1.05 bar). The purified gas, obtained at the top of the absorption column, contains a very small amount of unabsorbed CO₂ (less than 1 % vol.). The rich CO₂ amines solutions obtained at the bottom of the absorption column is sent to the desorption column for solvent regeneration. Contrasting the absorption process, the desorption process takes place at a higher temperature and lower pressure. The rich CO₂ amine stream is compressed using a pump and then is heated to about 100 - 120°C temperature using a heat exchanger and afterwards is sent to the desorption column. The solvent regeneration is done by using a low pressure stream of 2 bar. The top stream is cooled and is sent to a drop separator from where the water is recovered at the bottom and the rich CO₂ gas (more than 90 % CO₂ vol.) is recovered at the top. The rich CO₂ gas obtained is sent to the compression unit, which has 4 compression stages with intercoolers. In the first stage the gas is compressed from 1.98 to about 6 bar; then the pressure is further increased in the second stage from 6 to 18 bar; the third stage the pressure reached 54 bar and last the final pressure is 122 bar. This stage compression method was chosen in order to avoid the overheating of the compressor and to allow the intermediate cooling of the compressed gas. After each cooler a drop separator is added in order to removes the water drops that could condense. The compressed CO₂ stream at 122 bar will be sent at the storage sites (geological storage like saline aquifers or used for Enhanced Oil Recovery - EOR).

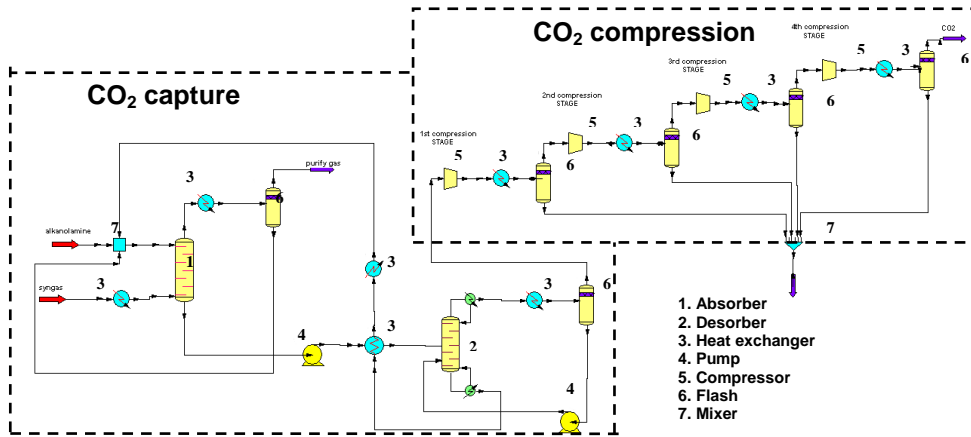


Figure 2. Carbon dioxide capture plant

The carbon dioxide absorption process was modelled and simulated using the AMINE model from the ChemCAD software. Other sub-systems of the plant and their design assumptions used in the mathematical modelling and simulation are presented in Table 3.

Table 3. Main design assumptions

Stream/Unit	Parameters
Flue gas	Pressure: 1.05 bar Temperature: 40 °C Composition (gas % vol.): 12.04 % O ₂ ; 74.13 % N ₂ ; 8.40 % CO ₂ ; 4.52 % H ₂ O; 0.91% Ar
Absorption columnn	Absorbent: alkanolamine Absorbent feed temperature: 40 °C Absorbent feed pressure: 1.05 bar Absorbent feed concentration (wt %): 30% MEA (case 1); 30% DEA (case2); 30% TEA (case 3); 30% DIPA (case 4); 50% MDEA (case 5)
Heat exchangers	$\Delta T_{min} = 10^{\circ}C$
Desorption columnn	Pressure drop: 1% of inlet pressure
CO ₂ compression	Pressure: 2 bar Temperature: 105 °C Delivery pressure: 122 bar Compressor efficiency: 85%
Captured CO ₂ stream	H ₂ O limit concentration: <500 ppm CO ₂ capture rate: >90%

ACKNOWLEDGMENTS

The authors wish to thank for the financial support provided from programs:
 - Investing in people! PhD scholarship, Project co-financed by the SECTORAL OPERATIONAL PROGRAM FOR HUMAN RESOURCES DEVELOPMENT 2007-2013, Contract nr.: POSTRU/88/1.5/S/60185 –“Innovative doctoral studies in a Knowledge Based Society “ and - Romanian National University Research Council (CNCSIS-UEFISCU), project number 575 / 19.01.2009, PNII – IDEI code 2455 / 2008: “Innovative systems for poly-generation of energy vectors with carbon dioxide capture and storage based on co-gasification processes of coal and renewable energy sources (biomass) or solid waste”.

REFERENCES

1. Tobiesen F.A., Juliussen O., Svendsen H.F., *Chemical Engineering Science*, **2008**, 63, 2641.
2. Gabrielsen J., Michelsen M.L., Stenby E.H., Kontogeorgis G.M., *Industrial & Engineering Chemistry Research*, **2005**, 44, 3348.
3. Figuera J.D., Fout F., Plasynski, S., McIlvired, H., Srivastava, R., “Advances in CO₂ capture technology - The U.S. Department of Energy's Carbon Sequestration Program. Int. J. Greenhouse Gas Control”, **2008**, 2, 9-20.
4. Metz B., Davidson O., Coninck H., Loos M., Meyer L., “IPCC Special Reports - Carbon Dioxide Capture and Storage” Cambridge University Press, England, **2005**, chapter 3.
5. Itoh J., *Chemical & Physical absorption of CO₂* , Dow Chemical Japan Ltd., January 14, **2005**.
6. Meisen A., Shuai X., *Energy Conversion and Management*, **1997**, 37.
7. Cormoș C., “Decarbonizarea combustibililor fosili solizi prin gazeificare”, Presa universitară Clujeană , Cluj Napoca, **2008**, chapter 5.
8. Kohl A., Nielsen R., “Gas purification”, fifth edition, Gulf Publishing Company, Houston, **2005**, chapter 2.
9. Maceiras R., Álvarez E., Cancela Á., *Chemical Engineering Journal*, **2008**, 138, 295.
10. Jockenhoevel T., Schneider R., Rode H., *Energy Procedia*, **2009**, 1, 1043.
11. Eide-Huagmo I., Brakstad Gunnar O., Hoff Anders K., Sorheim Rist K., Falck da Silva E., Svendsen H. F., *Energy Procedia*, **2009**, 1, 1297.
12. Heimel S., Lowe C., *Energy Procedia*, **2009**, 1, 4039.
13. Lepaumier H., Picq d., Carrette P.L., *Energy Procedia*, **2009**, 1, 893.
14. Yang H., Xu Z., Fan M., Gupta R., Slimane R., Bland A., Wright I., *Journal of Environmental Science*, **2008**, 20, 14.
15. Usubharatana P., Tontiwachwuthikul P., *Energy Procedia*, **2009**, 1, 95.
16. Dugas R., Alix P., Lemaire E., Broutin P., Rochelle G., *Energy Procedia*, **2009**, 1, 103.

IN VITRO STUDY ON THE EFFECTIVENESS OF A GROUP OF EXPERIMENTAL HYDROGEN PEROXIDE AND CARBAMIDE PEROXIDE BLEACHING GELS UPON DENTAL ENAMEL

DIANA DUDEA^a, MARIOARA MOLDOVAN^b, LAURA SILAGHI DUMITRESCU^b, HORATIU COLOSI^c, ALEXANDRA BOTOS^a, ADA IRIMIE^a, CAMELIA ALB^a

ABSTRACT. Chemical dental bleaching products are mainly based on hydrogen peroxide (HP) or its organic derivative carbamide peroxide (CP). This study aimed to demonstrate the bleaching effect of five experimental bleaching agents formulas (EBA), containing either CP or HP, when compared with five commercial bleaching agents (CBA), with similar concentration in active ingredients. The bleaching effect was tested on five groups of extracted human permanent teeth and the CIEL*a*b* color parameters were recorded with a dental spectrophotometer (Vita Easyshade). In each case, on the facial surface EBA was applied, while on the lingual part CBA with similar concentration in active ingredients was used. Increasing of lightness (L^*) and a tendency of reducing the yellowness (b^*) and redness (a^*) were recorded, for both EBA and CBA. The most important variations were obtained for the formulas based on 15% CP and the lowest for the 35% HP, following the indicated clinical protocols. Overall significant differences regarding lightness (ΔL^*) and color (ΔE^*) between the 5 groups of bleaching agents with various formulas, for both EBA and CBA were recorded.

Key words: carbamide peroxide, hydrogen peroxide, bleaching

INTRODUCTION

One of the most important factors related to the dental appearance is the color, which is considered as a complex parameter, being influenced by reflection, absorption, and dispersion of the incident light through tissues with different optical properties (enamel, dentine, dental pulp) [1,2]. According to the origin of the coloring agent and its location related to the dental structure, either extrinsic or intrinsic discoloration are generated [1,3].

^a University of Medicine and Pharmacy "Iuliu Hațieganu", Dept. of Dental Propaedeutics, Faculty of Dentistry, Clinicilor Str.32, RO- 40006 Cluj-Napoca, Romania, ddudea@umfcluj.ro

^b University Babeș-Bolyai, Institute of Chemical Research "Raluca Ripan", Str. Fântânele Nr. 30, RO-400294, Cluj-Napoca, Romania

^c University of Medicine and Pharmacy "Iuliu Hațieganu" Dept. of Medical Informatics and Biostatistics, Faculty of Medicine, Pasteur str.6, RO-400349 Cluj-Napoca, Romania

In the case of extrinsic discoloration, which affect the enamel surface, the chromophores, represented mainly by polyphenolic compounds, originate more often from dietary sources. Polyphenols range from small flavonoids, such as the green tea catechines and grape-skin antocyanins (molecular weight-300), to highly polymerized structures containing more than 50 flavanol molecules, such as the black tea teaflavins (1kDa) and thearubigins (>1kDa). Acidic proline –rich proteins contained in saliva are included into the pellicle which coats the enamel; they are believed to mediate the staining of the enamel by dietary polyphenols [4].

Indirect extrinsic tooth staining is mainly associated with cationic antiseptics, such as bis- biguanides (chlorhexidine), pyrimidine derivatives (hexetidin), oral iron salts in liquid form, essential oils, and amoxicillin [2, 5, 6]. In these circumstances, the agent is without color or with a different color from the stain produced on the tooth surface.

Internalized stains are the result of extrinsic stains entering the dentine via dental structure's defects [7]. In these circumstances, the chromophores may become attached to the organic tissue contained in interprismatic sites, by chemical binding of their hydroxyl and amino groups. The pigmented substances may also form with the calcium ions new molecules varying in size and optical properties [8].

In the case of intrinsic discoloration, the pigmentation, which affects mainly the dentine, has pulpal or systemic origin [9]. The chromogens enter the tooth by an endogenous route, in case of metabolic disorders with or without genetic involvement. In the same group are included discoloration caused by medication (staining caused by tetracycline or dental fluorosis) or local pigmentation due to pulpal hemorrhage or generated by substances used during endodontic treatment [8,10].

When the chromophore is incorporated into the structure of enamel or dentine, prophylactic methods are not enough, and chemical or prosthetic procedures are indicated [11]. Chemical whitening of discolored teeth was performed in dentistry using various agents: some have an oxidant effect, some act through erosion or abrasive potential, others use a combination of these methods [12]. Except some instances of internal bleaching, when sodium perborate is indicated, most treatments commonly used are based on hydrogen peroxide (HP) or it's organic derivate carbamide peroxide (CP) (peroxid-ureea) [13]. Hydrogen peroxide acts as a powerful oxidizing agent and generates monoanion (HO_2^-) and hydroxyl radical (OH). Subsequently, CP releases urea, which is decomposed into carbon dioxide and ammonia. Chemical reaction of the two reagents with the organic extracelullar matrix components, including pigments or chromophores, constitutes the chemical basis of tooth whitening [13,14]. On the other hand, the oxidative reaction is unspecific and the peroxides can also affect the organic matrix of the enamel and dentine [15,16].

There are two groups of commercial products: based on HP 5.5% or 35% or CP 10%, 15%, 30% or 35 %. The clinical protocols are carried out either as “in-office” methods, performed by dental surgeons or as “at-home” treatments. Each method needs a different protocol, which varies according to the exposure time to bleaching gel, concentration in active substance and individual characteristics of the bleached substrate [13].

The present study aims to demonstrate the bleaching effect of a group of experimental bleaching agents, based on CP and HP, when compared with a group of commercial bleaching products, with similar concentration in active ingredients.

RESULTS AND DISCUSSION

A group of 15 permanent human lateral extracted teeth were experimentally stained in coffee infusion and, in order to obtain a buccal part and a lingual portion, the anatomical crown was sectioned mesio-distally (using a low speed diamond saw -Isomet, Buehler LTD, Lake Bluff, USA-, under water lubrication). The teeth were divided into 5 groups G_1 - G_5 ($n=3$), each group was treated with a different formula of bleaching gel; in each case, similar concentration of active ingredient was used for buccal and lingual surface; on the buccal surface experimental bleaching agent (EBA) was applied, while on the lingual portion commercial bleaching agent (CBA) was used.

Five different formulas of EBA, containing, as active ingredients, either CP 10% (EBA_1), CP 15 %, (EBA_2 and EBA_3), CP 35% (EBA_4) or HP 35% (EBA_5) were tested in this study (section Experimental, table 5)

The number of applications and the duration of each treatment were selected according to the concentration of the active ingredient, in order to simulate the clinical protocol, indicated for each chemical formula (section Experimental, table 6)

Dental color measurement was performed by an instrumental method, using a dental spectrophotometer- Vita Easyshade.

The CIEL*a*b* color parameters L_1^* , a_1^* , b_1^* and L_2^* , a_2^* , b_2^* evaluated before and after the bleaching treatment for the EBA and CBA are included in tables 1 and 2, respectively.

In each case an increasing of lightness (L^*) is noticed, as a result of the bleaching process. Related to the chromatic parameters, a tendency of reducing the yellowness (b^*) and redness (a^*) is associated with the decreasing of staining. Since the differences in lightness (ΔL^*) are best perceived visually when the dental shade is evaluated [17], we indicated the mean values of variation in this parameter for each group. The results are included in table 3.

Table 1. CIEL *a*b* color parameters evaluated for the EBA before and after the bleaching treatment

Group of teeth	Tooth	Before bleaching			After bleaching		
		L* ₁	a* ₁	b* ₁	L* ₂	a* ₂	b* ₂
G1	1	77,2	0,3	24,9	88	-2,1	24,6
	2	75	4,3	26,1	85,5	2,3	27,4
	3	71,7	0,4	25,1	88,1	0,4	34,5
G2	4	74,7	4,1	35,1	87,1	2,8	38,9
	5	71,6	6,1	39,4	86,3	2	38,5
	6	67,9	3,5	37,3	83,8	3,4	37,4
G3	7	67,9	7,3	43	82,2	0,8	33,9
	8	76,6	1,8	33,3	82,9	-1	23,5
	9	74,8	4,2	37,7	86	4,5	38,6
G4	10	67,5	6,4	42,3	71,6	3,6	38,7
	11	67,4	5	33,1	77,1	1,9	28,4
	12	70,3	6,1	39,2	75,2	2,2	33,4
G5	13	71,7	5,4	36,7	77,2	2,6	34,7
	14	76,1	6,2	44,2	77,1	3	38,9
	15	70,3	4,4	31,8	74,3	2,8	29,1

Table 2. CIEL *a*b* color parameters evaluated for the CBA before and after the bleaching treatment

Group of teeth	Tooth	Before bleaching			After bleaching		
		L* ₁	a* ₁	b* ₁	L* ₂	a* ₂	b* ₂
G1	1	66,2	2,3	30,5	95,8	-2,5	28,5
	2	72,7	4,4	29,6	83	1,9	28,5
	3	77,6	-0,4	32,8	92,9	-2,1	35,4
G2	4	69,1	4,1	32	84,4	0,4	29,3
	5	69,8	4,6	33,5	85,9	1,4	35,3
	6	71,6	4,4	34,4	86	1,2	28,4
G3	7	74,5	4,3	39,9	89,8	-0,3	37
	8	76,9	2,7	36	84,5	-0,2	28,4
	9	71,1	5,4	40,9	89,2	3,5	42,8
G4	10	66,3	6,2	37,4	74,1	3,7	38,2
	11	70	4,6	34,6	75,3	0,7	24,4
	12	62,3	10,4	43,2	72,3	4	37,2
G5	13	72,9	5	37,5	79,8	2,5	34,1
	14	73,6	6,8	42,4	78,4	3,2	36,7
	15	72,6	4,7	29,1	75,3	0,8	23,5

The ΔL^* values ranged between 14.33 - 3.5 for the groups treated with EBA and 18.4 - 4.8 for the groups treated with CBA. The highest results were obtained for the 15% CP formulas and the lowest for the 35% HP following the indicated protocols. In each case, the increasing of the lightness was higher for the groups treated with CBA than for the groups treated with EBA, at similar concentration of the active ingredients.

The results of the variation in the dental color (ΔE^*) for the groups treated with EBA and CBA are indicated in table 4. The mean value of ΔE^* for each group is also presented.

Table 3. Variation of lightness (ΔL^*) due to the bleaching treatment with EBA and CBA

Group of teeth	Tooth nr	ΔL^* for EBA	Mean ΔL^* for EBA	Std. Dev.	ΔL^* for CBA	Mean ΔL^* for CBA	Std. Dev.
G ₁	1	10.8	12.567	3.323	29,6	18.400	10.016
	2	10.5			10,3		
	3	16.4			15,3		
G ₂	4	12.4	14.333	1.778	15,3	15.267	0.850
	5	14.7			16,1		
	6	15.9			14,4		
G ₃	7	14.3	10.600	4.033	15,3	13.667	5.437
	8	6.3			7,6		
	9	11.2			18,1		
G ₄	10	4.1	6.233	3.028	7,8	7.700	2.351
	11	9.7			5,3		
	12	4.9			10		
G ₅	13	5.5	3.500	2.291	6,9	4.800	2.100
	14	1			4,8		
	15	4			2,7		

Table 4. Variation of color (ΔE^*) for each group, due to the bleaching treatment with EBA and CBA

Gr. of teeth	Tooth nr.	ΔE^* for EBA	Mean ΔE^* for EBA	Std. Dev.	ΔE^* for CBA	Mean ΔE^* for CBA	Std. Dev.
G ₁	1	11.06	13.573	4.615	30.05	18.770	10.078
	2	10.76			10.65		
	3	18.9			15.61		
G ₂	4	13.03	14.736	1.510	15.97	16.133	0.327
	5	15.28			16.51		
	6	15.9			15.92		
G ₃	7	18.15	13.790	3.793	16.23	15.216	3.685
	8	11.98			11.13		
	9	11.24			18.29		
G ₄	10	6.13	8.623	2.541	8.22	11.216	2.660
	11	11.21			12.13		
	12	8.53			13.3		
G ₅	13	6.48	5.9433	0.755	8.08	7.893	0.497
	14	6.27			8.27		
	15	5.08			7.33		

The results of mean ΔE^* range between 5.943 and 14.736 for the groups treated with EBA and 7.893 and 18.77 for the groups treated with CBA. Like in the case of ΔL^* , the highest ΔE^* was obtained for the group treated with CP 15% and the lowest for the groups treated with HP 35%, using the indicated protocols (regarding the number of applications and the duration of each session). The variation of ΔE^* was higher for the groups treated with CBA than for the groups treated with EBA, in each case.

Considering the differences between ΔL^* and ΔE^* corresponding to the EBA versus CBA, no significantly statistic differences were obtained, for all tested formulas (G_1 - G_5) ($p=1$, exact significance of Wilcoxon signed ranks test for Group 1, $p>0.05$, exact significance of Wilcoxon signed ranks for groups 2-5).

When the bleaching effects of the various formulas and treatment protocols were compared using an analysis of variation, an overall significant difference has been observed between the 5 groups of different formulas regarding ΔL^* and ΔE^* values only for the EBA ($p<0.05$, ANOVA). For the investigated CBA, no overall significant difference between the 5 groups regarding ΔL^* and ΔE^* values has been observed using ANOVA ($p>0.05$). Given the reduced size of the evaluated groups, an exact significance of these differences has also been investigated using a non-parametric Kruskal-Wallis test, which rendered overall significant differences regarding ΔL^* and ΔE^* values ($p<0.05$) between the 5 groups for both EBA and CBA ($p=0.007$ for ΔL^* in EBA groups, $p=0.018$ for ΔL^* in CBA groups, $p=0.017$ for ΔE^* in EBA groups, $p=0.042$ for ΔE^* in CBA groups).

In our study, the extracted teeth were first experimental stained using coffee infusion, since it was stated that it is difficult to reveal differences in the effect of various bleaching techniques on nonstained samples [18]. This might explain the high values of ΔL^* and ΔE^* obtained in all instances, for both EBA and CBA.

Hydrogen peroxide was first used in dentistry in periodontal treatment, since it was demonstrated that it is effective against colonization and replication of anaerobic bacteria [19].

Due to the oxidizing process, highly pigmented carbon-ring compounds of the chromophores attached into the dental structure, are opened and converted into chains which are lighter in color. Existing carbon double-bond compounds are further converted into hydroxilic groups, which are usually colorless [14,20]. However, this reaction is unspecific and the organic and inorganic matrix of the enamel and dentine might be affected by the bleaching agents [15].

When CP gels are used for dental bleaching, upon contact with moisture, CP releases about 33% of it's content as HP [13, 21]. In addition, CP also releases urea, which is decomposed into ammonia and carbon dioxide. It is documented that urea and ammonium ions (NH_4^+) interfere

with the organic matrix of the enamel, initiating the degradation of the proteins, which are split into peptides and finally eliminated. By this, the diffusion of the hydrogen peroxide throughout the whole thickness of the enamel is increased [13].

CP [$\text{CO}(\text{NH}_2)\cdot\text{H}_2\text{O}_2$] [22] gels contain also stabilizers, catalysts, desensitizing and flavor agents [18]. The base vehicles are mainly represented by anhydrous glycerin, a type of glycol or a dentifrice [21].

Carbopol, a frequently used vehicle, enhances the contact between the CP and the tooth and slows the release of HP [13,15]. However, as an acidic polymer, it is believed to induce further adverse effects in the normal structure of the enamel, like demineralization and a consequent reduction of the enamel microhardness [15,23]; it also exhibits a high calcium binding capacity, that can inhibit hydroxiapatite crystal growth [15,24].

The variations of the lightness (ΔL^*) and color (ΔE^*) obtained in this study as a result of the bleaching process were more important than the results presented by other authors in similar protocols performed on bovine extracted teeth [18,25] or in clinical studies, in vivo [26]. This higher variation might be due to differences in the experimental protocols or to the instrumental methods used for measuring the color parameters.

Some manufacturers claim that an HP bleaching agent is faster in generating the whitening effect, as compared to a CP bleaching agent of similar concentration, since CP has to break down into HP and urea in order to be effective [27]. Our results suggests that the home-bleaching protocol, using lower concentration of peroxide carbamide, during a prolonged period of time is more efficient than the in-office methods, based on more powerful 35% hydroxide peroxide. Other studies reported similar results [18,27] and suggest that a higher concentration of hydrogen peroxide cannot compensate the reduced contact time between the bleaching gel and the tissues [18], mainly in the dentine, where the effectiveness of the procedure is dependent on an increased penetration of the active ions. From a clinical point of view, the "in office" methods are often followed by several sessions of lower concentration peroxide carbamide-based gels, during "at home" treatment [28]. Finally, there are studies that indicate no differences between the results obtained when the two methods are used, concluding that "at home" and "in office" methods indicated the same effectiveness [26].

We performed the immersion of the extracted teeth in artificial saliva during the experimental bleaching session, in order to simulate the oral environment; the content in calcium and phosphate might promote a remineralization similar to that produced in human saliva [15].

In order to characterize the dental color, several systems have been used. In this study we used the data derived from CIEL*a*b* system, with three linear coordinates: lightness (L^*) green-red chromatic coordinate (a^*),

and blue-yellow chromatic coordinate (b^*). Two other coordinates are also characteristic for this system- chroma (C^* - the strength of color) and hue (h^* - the name of the color itself). Color difference, which was calculated in this study reflects the sum of either $L^*a^*b^*$ or $L^*C^*h^*$ color coordinate differences, between the initial situation (before bleaching) and the final one (after bleaching) [29].

Dental color can be assessed either by visual or instrumental methods, which use spectrophotometers, colorimeters or computer analysis of digital images. All these methods have been used in order to assess the effectiveness of bleaching materials, with the usual recording of ΔL^* and ΔE^* , when the instrumental methods are used; delta shade guide is evaluated in the case of visual recording of the dental color, with a shade guide [30].

In the present study, we used a handheld intraoral spectrophotometer, Vita Easyshade, which is one of the most commonly used instrumental color measuring system in dentistry. These instruments measure one wavelength at a time from the reflectance or transmittance of an object [1,3] and have been used in dentistry not only for clinical reason but also in experimental studies performed on vital or extracted teeth. Though, two major disadvantages influence the predictability of it's results: edge –loss error, generated by an important fraction of the light which enter the tooth to be lost) and the difficulties in reproduction the position on the tooth's surface, since it is a free hand instrument [29] The edge-loss phenomenon and the difficulties in positioning the optical device are increased in the case of an irregular dental surface.

CONCLUSION

1. As a result of the bleaching treatment, the increase of value (L^*) and a tendency of reducing the yellowness (b^*) and redness (a^*) were recorded using spectrophotometric measurements, for both experimental and commercial bleaching gels.

2.The most important variation was obtained for the formulas based on 15% CP and the lowest for the 35% HP, following the indicated protocols.

3. Overall significant differences regarding ΔL^* and ΔE^* values ($p < 0.05$) between the 5 groups for both EBA and CBA were obtained ($p = 0.007$ for ΔL^* in EBA groups, $p = 0.018$ for ΔL^* in CBA groups, $p = 0.017$ for ΔE^* in EBA groups, $p = 0.042$ for ΔE^* in CBA groups)

4.Even if the variation of ΔL^* and ΔE^* was higher for the groups treated with CBA than for the groups treated with EBA, for all groups G_1 - G_5 , there was no significantly statistic difference between the variation of these parameters in EBA versus CBA groups. ($p = 1$, exact significance of Wilcoxon signed ranks test for Group 1, $p > 0.05$, exact significance of Wilcoxon signed ranks for groups 2-5).

EXPERIMENTAL

Dental staining was performed by immersion of the extracted teeth in a coffee infusion for 14 days. The solution (7 grams coffee, 300 ml boiled water) was daily renewed.

Dental bleaching

The bleaching gels covered the dental surfaces in a uniform layer of 1 mm thickness.

The protocols used are presented in table 5 and the formulas of the EBA, as well as their composition and properties are included in table 6.

Between bleaching intervals, the teeth fragments were maintained in artificial saliva (50mmol/l KCl, 1.5 mmol/l Ca, 0.9mmol/l PO₄, 20 mmol/l trihydroxymethyl-aminomethane buffer at pH 7.0) [15, 32]

Table 5. Clinical protocols indicated for each group of bleaching gels

Group of teeth	Experimental bleaching agents	Commercial bleaching agents	Experimental protocol
G1 Samples corresponding to teeth 1-3	EBA 1 – CP 10%	CBA 1 – CP 10%	14 days, 8 hours/day
G2 Samples corresponding to teeth 4-6	EBA 2 – CP 15%	CBA 2 – CP 15%	14 days, 8 hours/day
G3 Samples corresponding to teeth 7-9	EBA 3 – CP 15%	CBA 3 – CP 15%	14 days, 8 hours/day
Samples corresponding to teeth 10-12	EBA 4 – CP 35%	CBA 4 – CP 35%	7 days, 1 hour/day
Samples corresponding to teeth 13-15	EBA 5 – HP 35%	CBA 5 – HP 35%	2 sessions, 10 min each.

Table 6. Composition and properties of EBA, used on the buccal surfaces of the extracted teeth

EBA	pH [33]	Viscosity [33]	ingredients
EBA 1	6.5	700 CP	Carbamide peroxide 10%,glycerine, water, polyvinilpirolidone (PVP)
EBA 2	6	700 CP	Carbamide peroxide 15%,PVP, polyetilenglycol 200, SiO ₂ , Water
EBA 3	6	700 CP	Carbamide peroxide 15%, glycerine, water, Ethanol, PVP
EBA 4	4	660 CP	Carbamide peroxide 35%,PVP, polyetilenglycol 200 SiO ₂ Water
EBA 5	4	660 CP	Hydrogen peroxide 35%, PVP, SiO ₂

Dental color measurement

Vita Easyshade is a dental spot measurement spectrophotometer, its handpiece ends in a 5 mm fiber optic tip, containing 19 - 1 mm diameter fiber optic fibers [29,31]. The light source of the instrument is represented by a halogen- stabilized lamp, located in the base unit. This is monitored by several spectrophotometers, which also aim to measure the scattered light at 2 different distances from the tooth surface. These readings are combined in order to produce a „ principal spectrum” for the tooth [29]. The dental spectrophotometer was used in „global mode”, which indicate a basic color for the evaluated surface. In this mode, the tip of the instrument was located in the middle of the buccal or lingual surface of each tooth and the CIEL*a*b* color parameters: L*, a*, b*, were recorded.

For each tooth, the dental shade was measured on the buccal and lingual surface, before and after the bleaching treatment. As a result, two pairs of CIEL*a*b* color parameters were evaluated: L₁*, a₁*, b₁* (before bleaching) and L₂*, a₂*, b₂*. Using these parameters, two other values were calculated: ΔL^* (L₂-L₁), and ΔE^* – using the following formula:

$$\Delta E^* = (\Delta L^{*2} + \Delta a^{*2} + \Delta b^{*2})^{1/2}$$
$$\Delta L^* = L_2^* - L_1^*,$$
$$\Delta a^* = a_2^* - a_1^*,$$
$$\Delta b^* = b_2^* - b_1^*.$$

ACKNOWLEDGEMENTS.

This study was supported by Grant 152/2006, Viasan

REFERENCES

1. A. Joiner, *Journal of Denistry*, **2004**, 32, 3.
2. A. Watts, A. Addy, *British Dental Journal*, **2001**, 190, 309.
3. A. Joiner, G. Thakker, *Journal of Denistry*, **2004**, 32, 19.
4. G.B. Proctor, R. Pramanik, G.H. Carpenter, G.D. Rees, *Journal of Dental Research*, **2005**, 84, 73.
5. C.P. Ernst, K. Canbek, B. Willershausen, *Quintessence Int*, **2005**, 36, 641.
6. C.J. Tredwin, C. Scully, J.V. Bagan-Sebastian, *Journal of Dental Research*, **2005**, 84, 596.
7. C. Zantner, F. Derdilopoulou, P. Martus, A.M. Kielbassa, *Quintessence Int*, **2006**, 37, 695.

8. B. Touati. *Esthetic Dentistry and Ceramic Restauration*, Martin Dunitz, London, **1999**.
9. M. Sulieman, *Dental Update*, **2005**, 32, 463.
10. D.C. Chan, G.S. Rozier, A. Steen, W.D. Browning, M.S. Mozzafari, *Quintessence Int*, **2006**, 37, 637.
11. A. Wray, R. Welbury, *International Journal of Paediatric Dentistry*, **2001**, 11, 309.
12. A.B. Caballero, L.F. Navarro, J.A. Lorenzo, *Med. Oral. Patol. Oral. Cir. Bucal*, **2006**, 11, E.94.
13. M. Goldberg, M. Grootveld, E. Lynch, *Clin. Oral. Invest.*, **2009**. Published online 20 June.
14. R.E. Goldstein, D.A. Garber. *Complete Dental Bleaching*. Quintessence Books, Chicago, **1995**, Cap 2.
15. J.A. Rodrigues, G.P.F. Oliveira, C.M. Amaral, *Braz Oral Res*, **2007**, 21, 170.
16. G. Kugel, S. Ferreira, *J.Mass. Dent. Soc.*, **2005**, 53, 34.
17. R.D. Paravina, J.M. Powers. *Esthetic Color Training in Dentistry*. Elsevier Mosby, St Louis, **2004**.
18. D. Dietschi, S. Rossier, I.Krejci, *Quintessence Int*, **2006**, 37, 515.
19. N. Boksman, *Dentistry Today*, **2006**, 25, 74.
20. H. Alberts, ADEPT Report, **1991**, 2, 1.
21. D.S. Javaheri, G. Kugel, J.N. Janis, *Practical Procedures and Aesthetic Dentistry*, **2001**, 13, 10.
22. http://europa.eu.int/comm/food/fs/sc/sccp/out61_en.html acces 06.04.2003
23. R.T. Basting, A. Rodrigues JR, M.C. Serra, *Oper Dent*, **2005**, 30, 608.
24. W.A. Van der Reijden, M.J. Buijs, J.J. Damen, E.C. Veerman, J.M. Tencate JM, A.V. Nieuw Amerongen, *Caries Res.*, **1997**, 31, 216.
25. A. Wielgand, D. Vollmer, M. Foitzik, R. Attin, T. Attin, *Clin Oral Invest*, **2005**, 9, 91.
26. M. Bizhang, Y.H. Chun, K. Damerau, P. Singh, W.H. Raab, S. Zimmer, *Oper dent*, **2009**, 34, 635.
27. B.A. Matis, M.A. Cochran, G. Eckert, *Oper Dent*, **2009**, 34, 230.
28. M. de Silva Gottardi, M.G. Brackett, V.B. Haywood VB, *Quintessence Int*, **2006**, 37, 115.
29. R.D. Paravina, K.L. O'Keefe, B.L. Kuljic, *Balk K Stom*, **2006**, 10, 93
30. G.R. Mokhlis, B.A. Matis, M.A. Cochran, G.J. Eckert, *J Am Dent Assoc*, **2000**, 131, 1269.
31. R.W. Jung, W.D. Jung, Vita Easyshade, Doc.#20030915-1, **2003** Chicago. JLL technologies.
32. M.C. Serra, J.A.Curry, *Quintessence Int.*, **1992**, 23, 143.
33. *Farmacopeea Romana*, Ed a X.a, Editura Medicala, Bucuresti, **1993**.

OMEGA POLYNOMIAL IN DIAMOND-LIKE DENDRIMERS

KATALIN NAGY^a, CSABA L. NAGY^a AND MIRCEA V. DIUDEA^a

ABSTRACT. Design of diamond-related molecular structures can be achieved by using some net operations. The repeat unit used in this paper to build a nano-dendrimer is derived from adamantane, the constructive unit of diamond, and proved to be extremely stable, as shown by computed total energy. The dendrimer topology is described in terms of Omega polynomial.

Keywords: *Omega polynomial, dendrimer, diamond*

INTRODUCTION

The beauty (and usefulness) of diamond has kept its leading interest, among the newer “nano” carbon allotropes: fullerenes (zero-dimensional), nanotubes (one dimensional), graphene (two dimensional) or spongy carbon [1,2]. In the “nano-era”, the period of the last twenty years which started with the synthesis of fullerenes and nanotubes, theoretical and experimental studies revealed new properties, of interest for new applications. Out of electronic properties, the mechanical characteristics appear of great importance, as the composites can overpass the resistance of steel or other metal alloys. There are well-known the efforts in the production and purification of “synthetic” diamonds, from detonation products [3-9].

In this article, a nano-dendrimer is designed by using a diamond-related repeat unit, derived from the adamantane. The stability and topology of these structures are described in terms of total energy and Omega counting polynomial, respectively.

DENDRIMER BUILDING

The repeat unit used to build the nano-dendrimer here discussed was derived, from the tetrahedron T, by using the map operation [10-14] sequence $Op(Trs(P4(T)))$, as shown in Figure 1: The operation P4 (which transform the initial triangles into quadrilaterals – Figure 1, left) is followed by the selective truncation of the red points, which results in the red triangles (Figure 1, center). Finally, the opening of triangles by Op-operation (which puts one point of valence two on each bond of the red triangles) provides the red hexagons (Figure 1, right). The repeat unit superimposes partly over the

^a *Universitatea Babeș-Bolyai, Facultatea de Chimie și Inginerie Chimică, Str. Kogălniceanu Nr. 1, RO-400084 Cluj-Napoca, Romania, diudea@chem.ubbcluj.ro*

diamond lattice and plays the role of sp^3 tetrahedral carbon atom. Next, the nano-dendrimer was built up by pair-wise identification of the open faces (i.e., the red hexagons) of the tetrapode. Figure 2 illustrates the dendrimer at the 1st (left) and 2nd (right) generation.

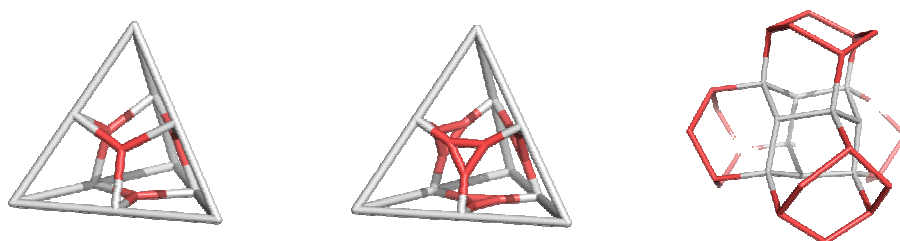


Figure 1. Unit U₃₄, designed by $Op(Trs(P4(T)))$. The red color is for an easier understanding the map operations used in the design of structures.

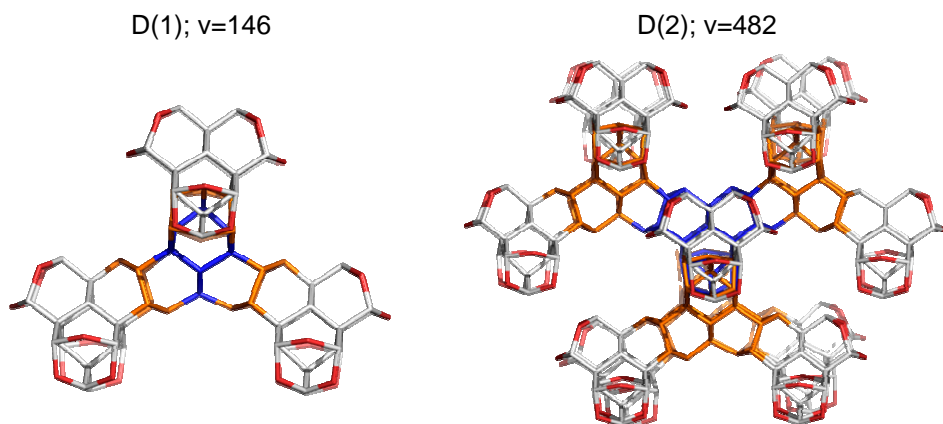


Figure 2. Dendrimers at the 1st (a) and 2nd (b) generation; v is the number of vertices/atoms.

Due to the large number of atoms, we limited here to calculate the total energy at the semi-empirical PM3 level of theory. Table 1 lists data (total energy per heavy atoms and HOMO-LUMO gap) for the new unit, as a hydrogenated sp^3 carbon structure, in comparison to the adamantane and diamantane, units of the diamond network. Data for the reference C_{60} fullerene (an sp^2 carbon structure) are also included. Remark the unit U₃₄ is closer to the diamond-related structures than to the C_{60} fullerene. The C-C bond length is in the range of 1.53-1.55 Angstroms while C-C-C angles fit between 107 and 110 degrees, as expected for single C-C bond containing compounds.

Table 1. PM3 data for the new diamond-related unit (as hydrogenated molecule) and some reference structures

Molecule	N_heavy	TE(kcal/mol)	TE/N_heavy	HOMO-LUMO Gap (eV)
U_34	34	-107178.99	-3152.32	13.07
Adamantane	10	-33051.90	-3305.19	14.43
Diamantane	14	-45414.05	-3243.86	14.06
C ₆₀	60	-163347.18	-2722.45	6.59

OMEGA POLYNOMIAL

In a connected graph $G(V,E)$, with the vertex set $V(G)$ and edge set $E(G)$, two edges $e = uv$ and $f = xy$ of G are called *codistant* e *co* f if they obey the relation [15]:

$$d(v,x) = d(v,y) + 1 = d(u,x) + 1 = d(u,y) \tag{1}$$

which is reflexive, that is, e *co* e holds for any edge e of G , and symmetric, if e *co* f then f *co* e . In general, relation *co* is not transitive, an example showing this fact is the complete bipartite graph $K_{2,n}$. If “*co*” is also transitive, thus an equivalence relation, then G is called a *co-graph* and the set of edges $C(e) := \{f \in E(G); f \text{ co } e\}$ is called an *orthogonal cut* oc of G , $E(G)$ being the union of disjoint orthogonal cuts:

$E(G) = C_1 \cup C_2 \cup \dots \cup C_k$, $C_i \cap C_j = \emptyset, i \neq j$. Klavžar [16] has shown that relation *co* is a theta Djoković-Winkler relation [17,18].

We say that edges e and f of a plane graph G are in relation *opposite*, e *op* f , if they are opposite edges of an inner face of G . Note that the relation *co* is defined in the whole graph while *op* is defined only in faces. Using the relation *op* we can partition the edge set of G into *opposite edge strips*, ops . An ops is a quasi-orthogonal cut qoc , since ops is not transitive.

Let G be a connected graph and $S(G) = S_1, S_2, \dots, S_k$ be the ops strips of G . Then the ops strips form a partition of $E(G)$. The length of ops is taken as maximum. It depends on the size of the maximum fold face/ring F_{max}/R_{max} considered, so that any result on Omega polynomial will have this specification.

Denote by $m(G,s)$ the number of ops of length $s=|s_k|$ and define the Omega polynomial as [19-26]:

$$\Omega(G,x) = \sum_s m(G,s) \cdot x^s \tag{2}$$

Its first derivative (in $x=1$) equals the number of edges in the graph:

$$\Omega'(G,1) = \sum_s m(G,s) \cdot s = e = |E(G)| \quad (3)$$

On Omega polynomial, the Cluj-Illmenau [15] index, $CI=CI(G)$, was defined:

$$CI(G) = \{ [\Omega'(G,1)]^2 - [\Omega'(G,1) + \Omega''(G,1)] \} \quad (4)$$

CALCULATION OF OMEGA POLYNOMIAL IN NANO-DENDRIMER

We used here the topological description by Omega polynomial because this polynomial was created to describe the covering in polyhedral nanostructures and because is the best in describing the constitutive parts of nanostructures, particularly for large structures, with a minimal computational cost. For the monomers/ repeat units, the stability evaluation was shown in Section 2.

Formulas for calculating the Omega polynomial and CI index are written function of the generation number r (Table 2); within this paper, the main results refer to $F_{\max}(6)$. The number of vertices/atoms v and the number of monomers/units m are also given. Examples were calculated by our original program called Nano Studio [27].

Table 2. Omega polynomial in $F[6]Id$ dendrimer.

Unit	Formulas
$F[6]IdD$	$\Omega(F[6]IdD, x) = 4(4 \cdot 3^r - 1) \cdot x^3 + \sum_{k=2}^r 12k(k-1) \cdot x^{3+4(r-k+1)} + 12 \cdot x^{3+4r}$ $\Omega'(F[6]IdD, 1) = 4r^4 + 20r^3 - 4r^2 + 28r + 24 + 48 \cdot 3^r$ $\Omega''(F[6]IdD, 1) = (32/5)r^5 + 36r^4 + 64r^3 + 156r^2 +$ $+ (848/5)r + 48 + 96 \cdot 3^r$ $CI(F[6]IdD) = 16r^8 + 160r^7 + 368r^6 + (288/5)r^5 +$ $1288r^4 + 652r^3 + 440r^2 + (5732/5)r + 504 +$ $3^r(384r^4 + 1920r^3 - 384r^2 + 2688r + 2160 +$ $2304 \cdot 3^r)$ $v(F[6]IdD) = 34m - 6(m - 1)$ $m(F[6]IdD) = 3^{r+1} - 3^r - 1$
Examples	$r=1; 44x^3+12x^7; CI=45672; v=146; e=216$ $r=2; 140x^3+24x^7+12x^{11}; CI=514512; v=482; e=720$ $r=3; 428x^3+72x^7+24x^{11}+12x^{15}; CI=4968840; v=1490; e=2232$

CONCLUSIONS

Design of diamond-like hypothetical structures was performed by using some operations on maps. The computed total energy of the involved repeat unit/monomer indicated stability close to that of adamantane and diamantane, the constructive units of diamond. The topology of the proposed networks was described in terms of Omega polynomial.

ACKNOWLEDGMENTS

Financial support from CNCSIS PNII IDEI 506/2007 is gratefully acknowledged.

REFERENCES

1. M. V. Diudea, *Ed.*, "Nanostructures, Novel Architecture", NOVA, **2005**.
2. M. V. Diudea, Cs. L. Nagy, "Periodic Nanostructures", Springer, **2007**.
3. P. S. DeCarli, J. C. Jamieson, *Science*, **1961**, 133, 1821.
4. A. E. Aleksenski, M. V. Baidakova, A. Ya. Vul', V. Yu. Davydov, Yu. A. Pevtsova, *Phys. Solid State*, **1997**, 39, 1007.
5. A. Krüger, F. Kataoka, M. Ozawa, T. Fujino, Y. Suzuki, A. E. Aleksenskii, A. Ya. Vul', E. Ōsawa, *Carbon*, **2005**, 43, 1722.
6. O. A. Williams, O. Douh ret, M. Daenen, K. Haenen, E. Ōsawa, M. M. Takahashi, *Chem. Phys. Lett.*, **2007**, 445, 255.
7. E. Ōsawa, *Diam. Rel. Mat.*, **2007**, 16, 2018.
8. E. Ōsawa, *Pure Appl. Chem.*, **2008**, 80, 1365.
9. V. N. Mochalin, Yu. Gogotsi, *J. Am. Chem. Soc.*, **2009**, 131, 4594.
10. M. V. Diudea, P. E. John, A. Graovac, M. Primorac, T. Pisanski, *Croat. Chem. Acta*, **2003**, 76, 153.
11. M. V. Diudea, *Forma (Tokyo)*, **2004**, 19, 131.
12. M. V. Diudea, M. Őtefu, P. E. John, A. Graovac, *Croat. Chem. Acta*, **2006**, 79, 355.
13. M. Őtefu, M. V. Diudea, P. E. John, *Studia Univ. Babeş-Bolyai*, **2005**, 50, 165.
14. M. V. Diudea, *J. Chem. Inf. Model.*, **2005**, 45, 1002.
15. P. E. John, A. E. Vizitiu, S. Cigher, M. V. Diudea, *MATCH Commun. Math. Comput. Chem.*, **2007**, 57, 479.
16. S. Klav ar, *MATCH Commun. Math. Comput. Chem.*, **2008**, 59, 217.
17. D. Ő. Djokovi , *J. Combin. Theory Ser. B*, **1973**, 14, 263.
18. P. M. Winkler, *Discrete Appl. Math.*, **1984**, 8, 209.
19. M. V. Diudea, *Carpath. J. Math.*, **2006**, 22, 43.

20. M. V. Diudea, S. Cigher, P. E. John, *MATCH Commun. Math. Comput. Chem.*, **2008**, 60, 237.
21. M. V. Diudea, S. Cigher, A. E. Vizitiu, M. S. Florescu, P. E. John, *J. Math. Chem.*, **2009**, 45, 316.
22. M. V. Diudea, *J. Math. Chem.*, **2009**, 45, 309.
23. M. V. Diudea, A. E. Vizitiu, F. Gholaminezhad, A. R. Ashrafi, *MATCH Commun. Math. Comput. Chem.*, **2008**, 60, 945.
24. M. V. Diudea, *MATCH Commun. Math. Comput. Chem.*, **2008**, 60, 935.
25. M. V. Diudea, S. Cigher, A. E. Vizitiu, O. Ursu, P. E. John, *Croat. Chem. Acta*, **2006**, 79, 445.
26. A. E. Vizitiu, S. Cigher, M. V. Diudea, M. S. Florescu, *MATCH Commun. Math. Comput. Chem.*, **2007**, 57, 457.
27. Cs. L. Nagy, M. V. Diudea, Nano Studio software, "Babes-Bolyai" Univ. **2009**.

OMEGA POLYNOMIAL IN SUCOR NETWORK

MAHBOUBEH SAHELI^a, MAHDIEH NEAMATI^a,
KATALIN NAGY^b AND MIRCEA V. DIUDEA^b

ABSTRACT. A new structurally functionalized graphene domain, called SuCor, was designed by combining the patterns of sumanene [6:(5,6)₃] and coronene [6:6₆]. The topology of the network is described in terms of Omega counting polynomial. Close formulas for calculating the polynomial and the Cluj-Ilimenau index derived from this polynomial are given.

Keywords: *sumanene, coronene, Sucor network, Omega polynomial*

INTRODUCTION

Several new carbon allotropes have been discovered and studied for applications in nano-technology, in the last twenty years, which can be assigned as the “Nano-era”. The impact of the Nano-Science resulted in reduction of dimensions of electronic devices and increasing their performances, at a lower cost of energy and money. Among the carbon new structures, fullerenes (zero-dimensional), nanotubes (one dimensional), graphene (two dimensional) and spongy carbon (three dimensional) are the most studied [1,2].

The present study deals with a hypothetical modified graphene, patterned by sumanene- and coronene-like units, of which topology is described in terms of Omega counting polynomial.

The lattice was built on the graphene sheet, of (6,3) tessellation, by decorating it with sumanene-like flowers, having coronene units as petals. The pattern, called Sucor, can be described as: {6:[5:(6:6₆)₃]}, with vertices/atoms of degree 3 and 4, as shown in Figure 1 (below). This network is the twin of Corsu lattice {6:[6:(5,6)₃]}, also proposed by Diudea [3-5].

Notice, the coronene and sumanene are molecules synthesized in the labs [6-8]. Our idea about these networks was also supported by the synthesis of several bowl-shaped molecules, inspired from the architecture of fullerenes and, more recently, by the direct synthesis [9] of fullerenes starting from open precursors. The design and synthesis of various domains on the graphene sheet, eventually functionalized, is nowadays a challenge study and practice [10-13].

^a Department of Mathematics, Faculty of Science, University of Kashan, Kashan 87317-51167, I.R. Iran, mmsaheli@yahoo.com

^b Faculty of Chemistry and Chemical Engineering, “Babes-Bolyai” University, 400028 Cluj, Romania, diudea@gmail.com

OMEGA POLYNOMIAL

Let $G(V,E)$ be a graph, with $V(G)$ and $E(G)$ being the set of vertices/atoms and edges/bonds, respectively. Two edges e and f of a plane graph G are in relation *opposite*, e *op* f , if they are opposite edges of an inner face of G . Then e *co* f holds by the assumption that faces are isometric. The relation *co* is defined in the whole graph while *op* is defined only in faces/rings (see below), thus being included in relation *co*. Relation *op* will partition the edges set of G into *opposite edge strips ops*, as follows. (i) Any two subsequent edges of an *ops* are in *op* relation; (ii) Any three subsequent edges of such a strip belong to adjacent faces; (iii) In a plane graph, the inner dual of an *ops* is a path, an open or a closed one (however, in 3D networks, the ring/face interchanging will provide *ops* which are no more paths); (iv) The *ops* is taken as maximum possible, irrespective of the starting edge.

The Ω -polynomial [14-17] is defined on the ground of opposite edge strips *ops* $S(G) = S_1, S_2, \dots, S_k$ in the graph. Denoting by m , the number of *ops* of cardinality/length $s=|S|$, then we can write

$$\Omega(x) = \sum_s m \cdot x^s \quad (1)$$

The first derivative (in $x=1$) can be taken as a graph invariant or a topological index; in this case, it equals the number of edges in the graph.

$$\Omega'(1) = \sum_s m \cdot s = e = |E(G)| \quad (2)$$

We used here the topological description by Omega polynomial because this polynomial was created to describe the covering in polyhedral nanostructures and because is the best in describing the constitutive parts of nanostructures, particularly for large structures, with a minimal computational cost.

METHOD

In elaborating the close formula for counting the Omega polynomial, we followed the steps: (1) find the coefficients of x^1, \dots, x^6 in every Sucor unit; (2) find the number of common edges W_n between the Sucor units; (3) find the number of blue hexagons B_n (i.e., triple joints); (4) find the coefficient of x^1, x^2, \dots, x^6 in the whole net; (5) find the formula to compute $\Omega(G, x)$ in a Sucor cyclic structure; (6) find W_n and B_n by a formula independent from common edges of the last complete cycle and (7) find a formula for $\Omega(G, x)$ in Sucor parallelogram structure.

Coefficients of x^1, \dots, x^6 in Sucor units

Local contributions to the polynomial coefficients are as follows.

The coefficient of x^1 is equal to $(3 \times 6) + (2 \times 6) + (3 \times 2) = 36$, for every Sucor unit.

The coefficients of x^2 and x^3 can be deduced from Figure 1, by following the red lines, in the left and right structures, respectively. In any 1/3 of Sucor units, there are 3 red lines, thus there are $3 \times 3 = 9$ red lines in each unit. Coefficient of x^4 is derived as shown in Figure 2. The coefficient of x^5 is equal to 6 and the coefficient of x^6 is deduced from W_n and B_n (see Figure 2 and below).

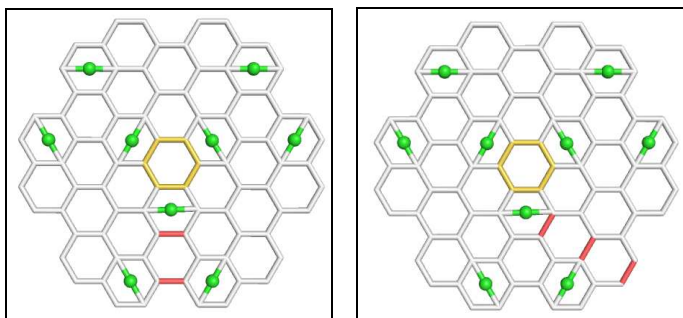


Figure 1. Ops of length 2 and 3 (edges marked in red).

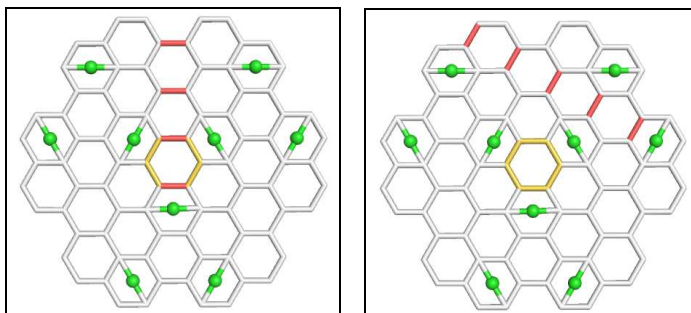


Figure 2. Ops of length 4 and 5 (edges marked in red).

Common edges (W_n) between Sucor units

“Common edges” means the edges common (i.e., double joints) of two SuCor units (Figure 3, in red). Clearly, $W_1=0$. Note, the colors have no chemical meaning (i.e., heteroatoms), they only help in describing the net. The center of SuCor units is yellow while the green points can be seen as bridges, in the chemical sense.

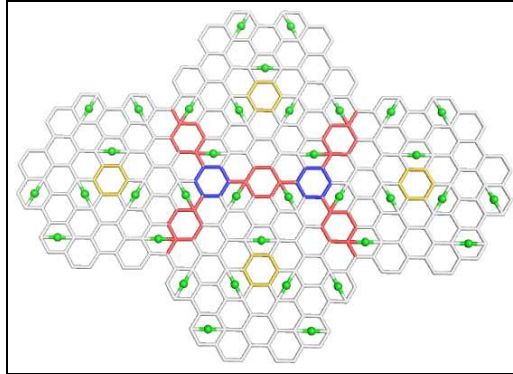


Figure 3. Network of four ($n=4$) Sucor units: yellow hexagons represent the unit core, while the blue one is the triple joints (B_n); the shared edges (W_n) between the units are marked in red.

We define r_k the number of Sucor units contained in a complete cyclic domain D_k , at the level k . For example $r_0=1$ and $r_1=7$, in general

$$\begin{aligned} r_k &= r_{k-1} + 6k \quad \text{or} \\ r_k &= 1 + 3k(k+1) \end{aligned} \quad (3)$$

To compute W_n we must calculate the number of common edges of the last complete cyclic domain D_k and the number of common edges between the newly added units and the last complete cycle and the already added new units.

The addition of a unit is made stepwise around the complete cyclic domain D_k and results in either one common edge or two common edges.

The number of units that make one common edge is $\left\lfloor \frac{n-r_{k-1}}{k} \right\rfloor$ while the number of units that make two common edges is $n-r_{k-1} - \left\lfloor \frac{n-r_{k-1}}{k} \right\rfloor$. So we

have the following formula for W_n

$$W_n = W_{n_{k-1}} + \left\lfloor \frac{n-r_{k-1}}{k} \right\rfloor + 2 \left(n-r_{k-1} - \left\lfloor \frac{n-r_{k-1}}{k} \right\rfloor \right) + (n-r_{k-1}-1) \quad (4)$$

For the special case when $n=r_k$, we need to add one more edge, thus we have:

$$W_n = W_{n_{k-1}} + \left\lfloor \frac{n-r_{k-1}}{k} \right\rfloor + 2 \left(n-r_{k-1} - \left\lfloor \frac{n-r_{k-1}}{k} \right\rfloor \right) + (n-r_{k-1}) \quad (5)$$

Triple joint blue hexagons B_n

The triple joints denoted B_n are depicted in Figure 3 by blue hexagons that get join of three units. It is easily seen that $B_1=B_2=0$ and $B_3=1$ and $B_4=2$; in general, to compute B_n we can use the formula

$$B_n = B_{r_{k-1}} + \left(n - r_{k-1} - \left\lfloor \frac{n - r_{k-1}}{k} \right\rfloor \right) + (n - r_{k-1} - 1) \quad (6)$$

When a cycle is completed, we have $n=r_k$ and one more edge must be added, thus:

$$B_n = B_{r_{k-1}} + \left(n - r_{k-1} - \left\lfloor \frac{n - r_{k-1}}{k} \right\rfloor \right) + (n - r_{k-1} - 1) + 1 \quad (7)$$

Coefficients of x^1, x^2, \dots, x^6

For every complete cycle, the coefficient of x^1 are:

$$6 \times 3 + 6 \times 2 + 3 \times 2 = 36$$

This value is modulated by the contributions of double and triple joints, so the coefficient of x is $36n - 4W_n - 3B_n$. Every common edge reduces the value of coefficient of x^2 by 3, thus it will be $9n - 3W_n$. Next, every common edge will increase by 2 the coefficient of x^3 , so that its value is $12n + 2W_n$. Similarly, we have: for x^4 ; $3n - W_n$; for x^5 ; $6n - 3B_n$; for x^6 ; $W_n + 3B_n$.

Omega polynomial in a Sucor cyclic structure

Now, we are able to write the formula for the Omega polynomial in case of a general cyclic Sucor structure (Figure 4, left):

$$\begin{aligned} \Omega(G, x) = & (36n - 4W_n - 3B_n)x + (9n - 3W_n)x^2 + (12n + 2W_n)x^3 \\ & + (3n - W_n)x^4 + (6n - 3B_n)x^5 + (W_n + 3B_n)x^6 \end{aligned} \quad (8)$$

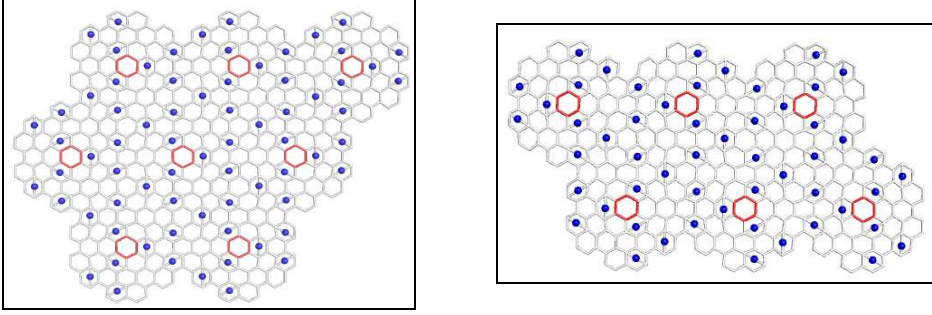


Figure 4. A cyclic domain $SuCor_8$, $v=688$ (left) and a parallelogram-like domain $P_{3,2}$, $v=522$ (right)

Examples are given in the table 1.

General formulas for W_n and B_n

In such a case, W_n is calculated by the formula:

$$\begin{aligned}
 W_n &= W_{r_{k-1}} + \left\lfloor \frac{n-r_{k-1}}{k} \right\rfloor + 2 \left(n-r_{k-1} - \left\lfloor \frac{n-r_{k-1}}{k} \right\rfloor \right) + (n-r_{k-1}-1) = W_{r_{k-1}} + 3(n-r_{k-1}) - \left\lfloor \frac{n-r_{k-1}}{k} \right\rfloor - 1 \\
 &= W_{r_{k-2}} + 3(r_{k-1} - r_{k-2}) - \left\lfloor \frac{r_{k-1} - r_{k-2}}{k-1} \right\rfloor + 3(n-r_{k-1}) - \left\lfloor \frac{n-r_{k-1}}{k} \right\rfloor - 1 \\
 &= \dots = W_{r_{k-k}} + 3(r_{k-(k+1)} - r_{k-k}) - \left\lfloor \frac{r_{k-(k+1)} - r_{k-k}}{k-(k+1)} \right\rfloor + \dots + 3(n-r_{k-1}) - \left\lfloor \frac{n-r_{k-1}}{k} \right\rfloor - 1 \\
 &= \left(\sum_{k=1}^z 3(r_k - r_{k-1}) - \left\lfloor \frac{r_k - r_{k-1}}{k} \right\rfloor \right) + \left(3(n-r_z) - \left\lfloor \frac{n-r_z}{z+1} \right\rfloor - 1 \right) \\
 &= \left(\sum_{k=1}^z 18k - 6 \right) + \left(3(n - (3z(z+1)+1)) - \left\lfloor \frac{n - (3z(z+1)+1)}{z+1} \right\rfloor - 1 \right)
 \end{aligned} \tag{9}$$

Similarly, for B_n we have:

$$\begin{aligned}
 B_n &= B_{r_{k-1}} + \left(n-r_{k-1} - \left\lfloor \frac{n-r_{k-1}}{k} \right\rfloor \right) + (n-r_{k-1}-1) \\
 &= \left(\sum_{k=1}^z 12k - 6 \right) + \left(2(n - (3z(z+1)+1)) - \left\lfloor \frac{n - (3z(z+1)+1)}{z+1} \right\rfloor - 1 \right)
 \end{aligned} \tag{10}$$

To find z in case $n > r_z$, (i.e., when the number of Sucor units are higher than in a complete cyclic domain D_z) we simply use the formula (3).

An algorithm for compute Omega polynomial $\Omega(G, x)$ in the Sucor net can be written as: give n ; find z ; find W_n and B_n ; if $n = 3z(z+1)+1$ then put $W_n = W_n + 1$ and $B_n = B_n + 1$; compute $\Omega(G, x)$

Omega polynomial in parallelogram domains $P_{a,b}$

In case of a parallelogram domain (Figure 4, right)) in Sucor net, the formulas are presented in the following.

$$W_{a,b} = (a-1)b + (2a-1)(b-1) = 3ab - 2a - 2b + 1 \quad (11)$$

$$B_{a,b} = 2(a-1)(b-1) = 2ab - 2a - 2b + 2 = W_{a,b} - ab + 1 \quad (12)$$

$$\begin{aligned} \Omega(G, x) &= (36n - 4W_{a,b} - 3B_{a,b})x + (9n - 3W_{a,b})x^2 + (12n + 2W_{a,b})x^3 + (3n - W_{a,b})x^4 \\ &\quad + (6n - 3B_{a,b})x^5 + (W_{a,b} + 3B_{a,b})x^6 \\ &= (36ab - 12ab + 8a + 8b - 4 - 6ab + 6a + 6b - 6)x + (9ab - 9ab + 6a + 6b - 3)x^2 \\ &\quad + (12ab + 6ab - 4a - 4b + 2)x^3 \\ &\quad + (3ab - 3ab + 2a + 2b - 1)x^4 + (6ab - 6ab + 6a + 6b - 6)x^5 \\ &\quad + (3ab - 2a - 2b + 1 + 6ab - 6a - 6b + 6)x^6 \\ &= (18ab + 14a + 14b - 10)x + (6a + 6b - 3)x^2 + (18ab - 4a - 4b + 2)x^3 \\ &\quad + (2a + 2b - 1)x^4 + (6a + 6b - 6)x^5 + (9ab - 8a - 8b + 7)x^6 \end{aligned} \quad (13)$$

Examples are given in Table 1.

Table 1. Examples of Omega polynomial and CI in Sucor network

Domain	Omega polynomial	CI
D_7	$186X + 27X^2 + 108X^3 + 9X^4 + 24X^5 + 30X^6$	806910
D_{19}	$444X^1 + 45X^2 + 312X^3 + 15X^4 + 42X^5 + 114X^6$	5866950
D_{12}	$297X^1 + 36X^2 + 192X^3 + 12X^4 + 33X^5 + 63X^6$	2353842
D_{17}	$408X^1 + 45X^2 + 276X^3 + 15X^4 + 42X^5 + 96X^6$	4709766
P_{32}	$168X^1 + 27X^2 + 90X^3 + 9X^4 + 24X^5 + 21X^6$	596490
P_{44}	$391X^1 + 45X^2 + 258X^3 + 15X^4 + 42X^5 + 87X^6$	4182894

Numerical calculations were made by our software package Nano Studio [18].

CONCLUSIONS

Omega polynomial description proved to be a simple and efficient method in topological characterization of new designed nano-structures. Quantum calculations, to evaluate the stability of some small domains of the SuCor graphene are in progress in our. Lab and will be presented in a further article.

ACKNOWLEDGMENTS

The work was supported in part by the Romanian Grant CNCSIS PN-II IDEI 506/2007.

REFERENCES

1. M. V. Diudea, Ed., "Nanostructures, novel architecture", NOVA, **2005**.
2. M. V. Diudea and Cs. L. Nagy, "Periodic Nanostructures", Springer, **2007**.
3. M. V. Diudea, A. Ilić, *Studia Univ. Babes-Bolyai*, **2009**, in press.
4. M. V. Diudea, *Int. J. Chem. Model*, **2009** (in press).
5. M. Saheli, M. Neamati, A. Ilić and M. V. Diudea, **2009**, *Croat. Chem. Acta* (submitted).
6. K. Yamamoto, *Pure Appl. Chem.*, **1993**, *65*, 157.
7. H. Sakurai, T. Daiko, T. Hirao, *Science*, **2003**, *301*, 1878.
8. H. Sakurai, T. Daiko, H. Sakane, T. Amaya, T. Hirao, *J. Am. Chem. Soc.*, **2005**, *127*, 11580.
9. K. Yu. Amsharov and M. Jansen, *J. Org. Chem.*, **2008**, *73*, 2931.
10. Novoselov K.S, Geim A.K., *Nat. Mater.*, **2007**, *6*, 183.
11. Dresselhaus M.S., Dresselhaus G., Hofmann M., *Phil. Trans. R. Soc. A.*, **2008**, *366*, 231.
12. Ando T., *Phil. Trans. R. Soc. A.*, **2008**, *366*, 221.
13. Katsnelson M.I., Geim A.K., *Phil. Trans. R. Soc. A.*, **2008**, *366*, 195.
14. M. V. Diudea, *Carpath. J. Math.*, **2006**, *22*, 43.
15. P. E. John, A. E., Vizitiu, S. Cigher, M. V. Diudea, *MATCH Commun. Math. Comput. Chem.*, **2007**, *57*, 479.
16. M. V. Diudea, S. Cigher, P. E. John, *MATCH Commun. Math. Comput. Chem.*, **2008**, *60*, 237.
17. M. V. Diudea, S. Cigher, A. E. Vizitiu, M. S. Florescu, P. E. John, *J. Math. Chem.*, **2009**, *45*, 316.
18. Cs. L. Nagy, M. V. Diudea, *Nano Studio software*, Babes-Bolyai Univ., **2009**.

A NEW LC/MS/MS METHOD FOR DETERMINATION OF LISINAPRIL IN HUMAN PLASMA

LAURIAN VLASE^a, DANIELA-SAVETA POPA^a,
DANA MUNTEAN^a, MARCELA ACHIM^a

ABSTRACT. A simple and sensitive liquid chromatography coupled with tandem mass spectrometry (LC/MS/MS) method for the quantification of lisinopril in human plasma was developed and validated. The separation was performed on a Zorbax SB-C18 column under isocratic conditions using a mobile phase of 11:89 (v/v) acetonitrile and 0.1% (v/v) trifluoroacetic acid in water at 45 °C with a flow rate of 1 mL/min. A 1% ammonia solution in acetonitrile was added post column. The detection of lisinopril was performed in multiple reaction monitoring (MRM) mode using an ion trap mass spectrometer with electrospray positive ionisation. The human plasma samples (0.25 mL) were deproteinized with 12% perchloric acid in water and aliquots of 15 µL from supernatants obtained after centrifugation were directly injected into the chromatographic system. The method shows a good linearity ($r > 0.9946$), precision (CV < 11.3 %) and accuracy (bias < 7.0 %) over the range of 1.29-129 ng/mL plasma. The lower limit of quantification (LLOQ) was 1.29 ng/mL and the recovery was between 97.5-105.9 %. The method is not expensive, it needs a minimum time for plasma sample preparation and has a run-time of 5.0 min for instrument analysis (retention time of lisinopril was 4.5 min). The developed and validated method is very simple, rapid and efficient, with wide applications in clinical level monitoring, pharmacokinetics and bioequivalence studies of lisinopril.

Keywords: *lisinopril, LC/MS/MS, therapeutic drug monitoring*

INTRODUCTION

Lisinopril, (S)-1-[N2-(1-carboxy-3-phenylpropyl)-L-lysyl]-L-proline (Fig. 1), is an orally active angiotensin converting enzyme inhibitor, primarily used in the treatment of hypertension, congestive heart failure and acute myocardial infarction, with benefits in diabetic nephropathy [1] and diabetic retinopathy [2]. It has a hydrophilic molecule. After oral administration the bioavailability of lisinopril is about 25%, but widely variable between individuals (6 to 60%). Lisinopril has a long half-life and is eliminated by kidneys, in the unchanged form, without being metabolized [3]. Elimination rate of lisinopril decreases with old age and kidney or heart failure. Therapeutic drug monitoring and dose

^a *University of Medicine and Pharmacy "Iuliu Hațieganu", Faculty of Pharmacy, Emil Isac 13, RO-400023, Cluj-Napoca, Romania, vlaselaur@yahoo.com*

adjusting can be necessary in elderly patients or in patients with significant renal impairment to avoid drug accumulation and the risks of dosage-related side effects.

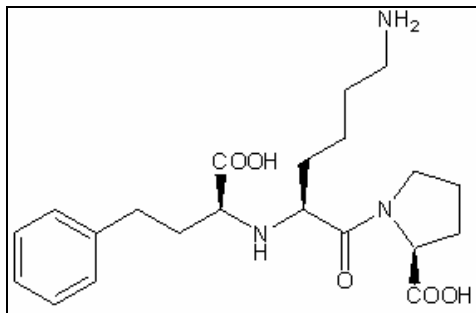


Figure 1. Chemical structure of lisinopril

Several methods involving radioimmunoassay [4], gas-chromatography (GC) coupled with mass spectrometry (MS) [5] and high-performance liquid-chromatography (HPLC) with ultraviolet (UV) [6], fluorescence [7] or mass spectrometric (MS) [8-10] detection have been reported to determine therapeutic levels of lisinopril in plasma. Radioimmunoassay is very sensitive but requires radiolabels and antilisinopril serum and it is not available to all researchers. Because its molecule is thermolabile and ionic, lisinopril must be derivatised into a derivative suitable for GC analysis. The sensitivity of HPLC-UV methods is inadequate for the measurement of lisinopril in plasma and the fluorescence detection also requires a derivatization step to chromophore derivatives. The GC and conventional HPLC methods involve solid phase extraction for the sample preparation. Both extraction and derivatization are time-consuming steps; they increase the cost of assay and can affect the recovery.

The LC/MS or LC/MS/MS method offers considerable advantages by its powerful performances: speed, selectivity, sensitivity and robustness [11, 12]. Sample preparation is more simple and rapid and often includes only precipitation of proteins (PP) [8, 13] or extraction before chromatographic analysis [9, 10, 14-16].

The aim of this work was to develop and validate a new simple and efficient LC/MS/MS assay for the quantification of lisinopril in human plasma for application in therapeutic drug monitoring and bioavailability studies.

RESULTS AND DISCUSSION

Sample preparation

In LC/MS/MS assays sensitivity depends on MS detection mode, but the method involved in sample preparation may influence the chromatographic background level and can generate matrix suppression effect. Several

researchers prefer to include in plasma sample preparation an extraction step to eliminate the impurities and to increase sensitivity (Table 1). Solid-phase extraction (SPE) is preferred as isolation method [9, 10, 14, 16] because of the amphoteric nature of lisinopril that would make the isolation difficult by simple liquid-liquid extraction (LLE). Huang et al. obtained constant extraction recoveries of lisinopril with a mixture of isopropanol and ethyl acetate (1:2, v/v) and pseudoephedrine hydrochloride as internal standard [15]. However, the extraction step increases the time of analysis and the costs and can affect the recovery. In scientific literature there were reported only two methods that used PP without extraction for determination of lisinopril in human plasma. Zhou et al. analyzed lisinopril by LC/MS after twice PP with methanol. They obtained a good sensitivity (LOQ of 2.5 ng/mL) and absolute recoveries between 94.4-98.2% [8]. Qin et al. used perchloric acid for PP. They obtained a better sensitivity (LOQ of 2 ng/mL), but the method requires the use of internal standard (absolute extraction recoveries of lisinopril were 55.1-58.6% for QC levels and absolute recovery of IS was 66.8%) [13]. Huang et al. reported the better LOQ. They quantified lisinopril in the linear range of 0.78-100 ng/mL plasma, but after isolation by LLE. The method also requires the use of internal standard (absolute extraction recoveries of lisinopril were 40.68-42.09% for QC levels) [15].

In our method we analysed volumes of only 0.25 mL plasma by PP with 12% perchloric acid (0.05 mL) and direct injection into the chromatographic system from supernatant after centrifugation. We obtained a very good sensitivity (LLOQ of 1.29 ng/mL) and better absolute recoveries (between 97.5 and 105.9%). Our method is more simple and rapid and offers a shorter time of analysis and a lower cost as compared with the other longer methods which used an extraction step prior to the chromatographic assay (Table 1). No matrix interference or ion suppression was observed from the plasma samples.

As the therapeutic doses effective in lowering blood pressure range from 10 to 80 mg of lisinopril per day and the therapeutic plasma levels of lisinopril are < 100 ng/mL, the LLOQ of 1.29 ng/mL established in our method can be accepted in bioequivalence studies and in routine purposes for therapeutic level monitoring of lisinopril in human plasma.

LC-MS assay

The chromatographic conditions, especially the composition of mobile phase, were optimized in several trials to achieve maximum sensitivity and symmetrical chromatographic peaks, a short retention time of lisinopril and consequently a shorter run time of analysis.

Several mobile phases containing varying percentages of organic acid were tested (Table 2). The best results were obtained with the mixture of acetonitrile and 0.1% (v/v) trifluoroacetic acid (TFA) in water (11:89, v/v) under isocratic conditions. By its amphoteric nature, lisinopril is ionized in aqueous solution whatever the pH is, thus giving a poor chromatographic

peak shape (tailing) on reversed-phase chromatography. The use of TFA as additive to aqueous phase has a large impact on the retention of lisinopril on C18 chromatographic column and also on its peak shape.

Table 1. Analytical characteristics of reported LC/MS and LC/MS/MS methods for the determination of lisinopril in human plasma or serum

Reference	Matrix	Detection mode ^a	Mobile phase constituents ^b	Pre-treatment/ extraction ^c	LOQ ^d (ng/mL)	Run time (min)	Absolute recovery (%)
Zhou [8]	Plasma	ESI-MS, SIM	formic acid (pH 2.9)- MeOH-ACN (58:25:17, v/v)	PP with methanol	2.5	NA ^e	94.4-98.2
Tashtoush [9]	Plasma	ESI-MS, SIM		SPE	10	NA	91.69
Tsakalof [10]	Serum (1mL)	ESI-MS, SIM	50 mM ammonium formate buffer (pH 3)-ACN- MeOH (72:7:21, v/v)	SPE	6	6	88
Qin [13]	Plasma (0.5mL)	ESI-MS/MS, SRM (m/z 406→246)	10 mM ammonium acetate buffer (pH 5)-MeOH (70:30, v/v)	PP with perchloric acid	2	5	NA
Padua [14]	Plasma (0.5mL)	ESI-MS/MS, MRM (m/z 406.3>84.3)	ACN:water (60:40, v/v) with 20 mM acetic acid and 4.3 mM TEA	SPE	2	6.5	79.2-82.5
Huang [15]	Plasma (0.4mL)	ESI-MS/MS, SRM (m/z 406.1→246)	MeOH:0.1% formic acid (50:50, v/v)	LLE	0.78	5	NA
Kousoulos [16]	Plasma (0.5mL)	ESI-MS/MS, SRM (m/z 406.1→83.6)	75% MeOH, 25% 10mM formic acid and 5mM ammonium acetate in water (v/v)	SPE	2	2	NA

^aSIM, selected ion monitoring; SRM, selected reaction monitoring; MRM, multiple reaction monitoring; ^bACN, acetonitrile; MeOH, methanol; TEA, triethylamine; ^cPP, protein precipitation; SPE, solid-phase extraction; LLE, liquid-liquid extraction; ^dLOQ, limit of quantification; ^eNA, not available.

Table 2. Influence of organic acid percent in aqueous mobile phase on retention time (RT) of lisinopril and its factor of capacity, k

Aqueous mobil phase	RT (min)	k
FA1 0.1%	0.75	2.8
TFA2 0.02%	1.5	6.5
TFA 0.04%	2.5	11.5
TFA 0.08%	4.8	23.0
TFA 0.1%	6.9	33.5
TFA 0.12%	7.2	35.0

¹FA – formic acid, ²TFA – trifluoroacetic acid

In 0.1% aqueous TFA (pH 1.9), lisinopril is transformed in a neutral adduct: the ionization of carboxylic groups is suppressed by the pH and the trifluoroacetate anion forms an ion-pair with ionized primary and secondary amino groups, neutralizing their charge. This way the lipophilicity of lisinopril is increased (Table 2) and the chromatographic peak becomes symmetric. However, there is also a drawback of using TFA in mass spectrometry: the strong ion-pair formed by TFA with analyte is no more ionized, so it cannot be “seen” by the mass spectrometer. The poor sensitivity due to TFA can be avoided by post-column adding a 1% ammonia solution in acetonitrile to neutralize the acid and to allow the ionization of lisinopril in electrospray ion source.

In the case of lisinopril, electrospray ionization (ESI) mode offers significantly higher signals compared to atmospheric pressure chemical ionization (APCI). The signal intensities of lisinopril obtained in positive ion mode were much higher than those in negative ion mode, so the former ionization mode was chosen. After the collision that induced the dissociation of lisinopril in ion trap mass spectrometer, the $[M+H]^+$ ion (m/z 406) produced some abundant ions (m/z 245, 246, 291, 309) at the optimum collision energy of 0.9 V (Fig. 2), thus, the detection of lisinopril was carried out in multiple reaction monitoring (MRM). The extracted ion chromatogram (EIC) of m/z (245, 246, 291, 309) from m/z 406 was monitored and analyzed. In the selected chromatographic conditions the retention time of lisinopril was 4.5 min and the analytical run-time was 5 min.

Assay validation

The method was validated in accordance with international regulations [17, 18]. Representative chromatograms of drug-free plasma and plasma spiked with lisinopril at LLOQ are shown in Fig. 3. No interfering peaks from the endogenous plasma components were observed in the retention time of lisinopril.

The calibration curves were linear over the concentration range of 1.29 – 129 ng/mL in human plasma, with a correlation coefficient greater than 0.9946. The LLOQ was 1.29 ng/mL. The values obtained for intra-day and inter-day precision and accuracy during the validation are shown in Tables 3 and 4, respectively.

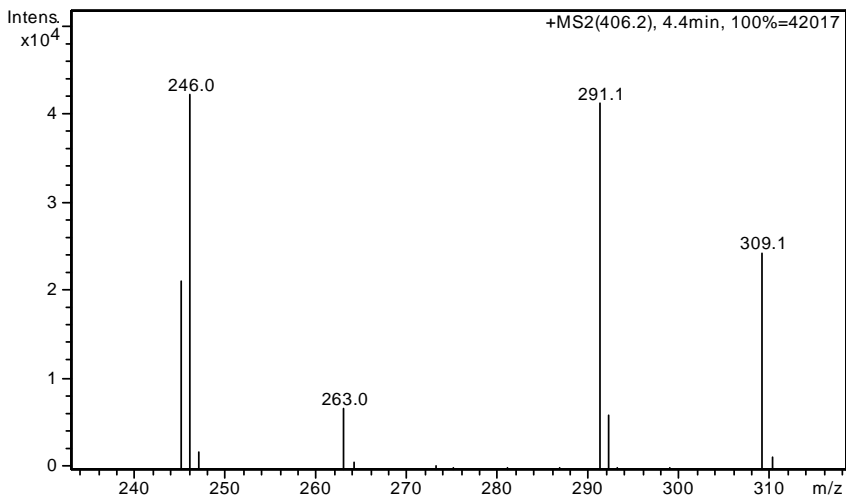


Figure 2. MS/MS spectra of lisinopril

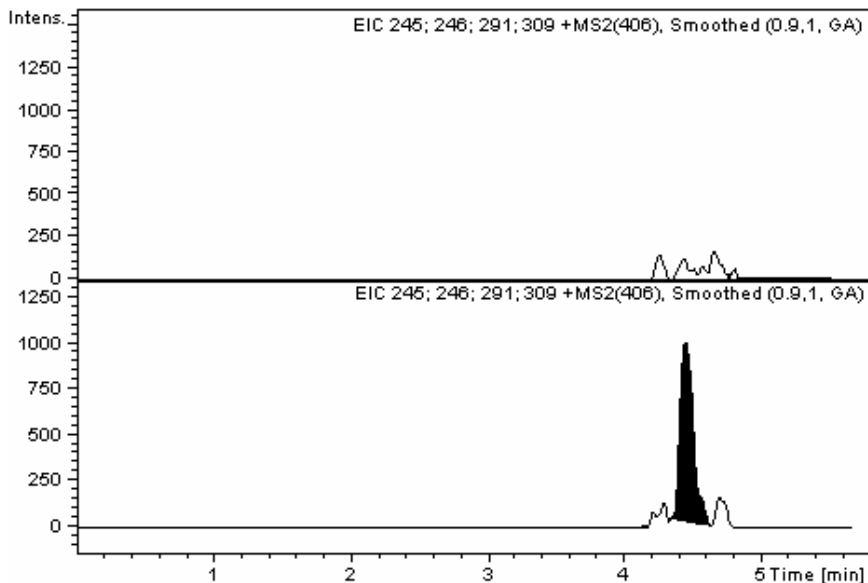


Figure 3. Representative chromatograms of (up) blank plasma and (down) plasma spiked with lisinopril at lower limit of quantification (1.29 ng/ml) (retention time – 4.5 min)

Table 3. The intra-day precision (CV %) and accuracy (bias %) and recovery data for the measurement of lisinopril in human plasma (n = 5)

C_{nominal} ng/mL	Mean C_{found} ng/mL (± S.D.)	CV %	Bias %	Recovery % (± S.D.)
1.29	1.26±0.10	8.2	-2.8	98.9±8.7
3.87	3.72±0.32	8.5	-3.9	105.9±9.2
19.36	19.83±1.31	6.6	2.4	99.1±6.6
51.62	53.16±1.71	3.0	3.0	99.0±3.2

Table 4. The inter-day precision (CV %) and accuracy (bias %) and recovery data for the measurement of lisinopril in human plasma (n = 5)

C_{nominal} ng/mL	Mean C_{found} ng/mL (± S.D.)	CV %	Bias %	Recovery % (± S.D.)
1.29	1.38±0.16	11.3	7.0	100.9±3.9
3.87	3.70±0.21	5.6	-4.4	101.3±11.4
19.36	20.49±0.77	3.8	5.8	102.1±4.3
51.62	53.77±1.42	2.6	4.2	97.5±7.6

All values for accuracy and precision were within recommended limits (<15%). The absolute recovery values were between 97.5 and 105.9%. Lisinopril showed a good post-preparative stability (PPS) in autosampler at room temperature following sample processing for at least 24 h (CV% of -6.4% at lower level and -3.8% at higher level, respectively) and a good stability (RTS) in plasma for 4 hours at room temperature (CV of -6.6% at lower level and -1.7% at higher level, respectively). Lisinopril is found to be stable at three freeze-thaw cycles (the concentration was changed with 3.5% at lower level and with 9.1% at higher level, respectively) and it was also stable in plasma stored at -20°C for at least 5 months (concentration changed with 0.2% at lower level and with 3.0% at higher level, respectively).

Method application

The validated method for determination of lisinopril in human plasma was successfully applied in a bioequivalence study of a generic formulation with lisinopril versus Zestril after oral administration of a dose of 20 mg lisinopril to 20 volunteers. The mean drug plasma concentration – time curve of lisinopril obtained is shown in Fig. 4.

CONCLUSION

Our developed LC-MS/MS assay is simple, rapid, accurate and not expensive. In comparison with other published LC-MS/MS [13-16] or LC-MS [8-10] assays for therapeutic level monitoring of lisinopril in human plasma our method performs better in terms of volume of analyzed plasma sample, analyte recovery, speed (both sample preparation and chromatographic run-time) and costs, which are essential attributes for methods used in routine analysis. The method was validated over the concentration range of 1.29-129 ng/mL which covers therapeutic plasma levels of lisinopril. This new fast method was successfully applied in bioavailability study of lisinopril, but it can also be used in therapeutic drug monitoring of lisinopril in human plasma.

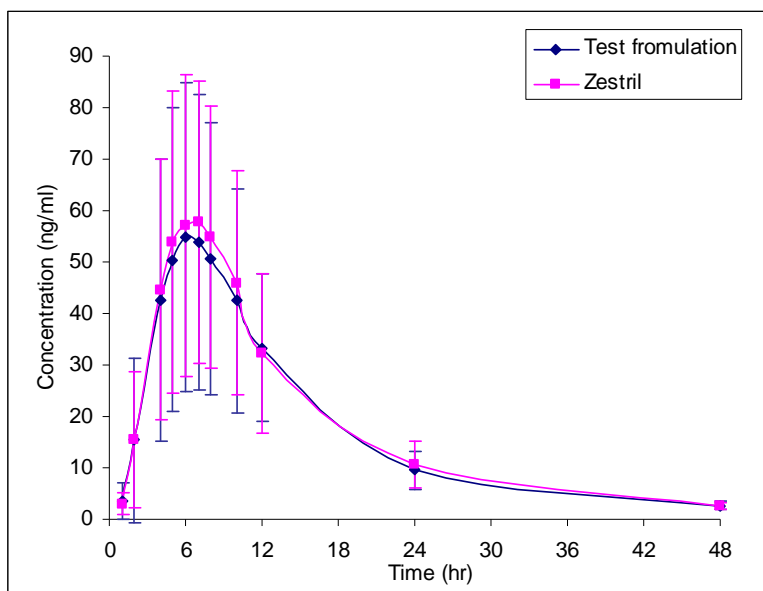


Figure 4. Mean plasma concentration – time curve for lisinopril after oral administration of a generic formulation containing 20 mg lisinopril and Zestril (20 mg lisinopril), respectively, obtained from healthy male volunteers (n=20, mean value and SD are plotted)

EXPERIMENTAL SECTION

Reagents

Lisinopril was reference standard from AC Helcor SA, Romania. Acetonitrile and methanol of isocratic grade for liquid chromatography, formic acid, trifluoroacetic acid and 70% perchloric acid of analytical-reagent

grade were purchased from Merck KGaA (Darmstadt, Germany). Bidistilled, deionised water pro injections was purchased from Infusion Solution Laboratory of The University of Medicine and Pharmacy Cluj-Napoca (Romania). The human blank plasma was supplied by the Bleeding Centre Cluj-Napoca (Romania) from healthy volunteers, men and women.

Apparatus

The following apparatus were used: 204 Sigma Centrifuge (Osterode am Harz, Germany); Analytical Plus and Precision Standard Balance (Mettler-Toledo, Switzerland); Vortex Genie 2 mixer (Scientific Industries, New York, USA); Ultrasonic bath Elma Transsonic 700/H (Singen, Germany). The HPLC system used was an 1100 series Agilent Technologies model (Darmstadt, Germany) consisting of two G1312A binary pumps, an in-line G1379A degasser, an G1329A autosampler, a G1316A column oven and an Agilent Ion Trap Detector 1100 VL.

Chromatographic and spectrometric conditions

Chromatographic separation was performed on a Zorbax SB-C18 (100 mm x 3.0 mm i.d., 3.5 μm) column (Agilent Technologies) under isocratic conditions using a mobile phase of a 11:89 (v/v) mixture of acetonitrile and 0.1% (v/v) trifluoroacetic acid in water at 45 °C with a flow rate of 1 mL/min. A 1% ammonia solution in acetonitrile was added post column with a flow rate of 0.1 mL/min by an another Agilent HPLC pump. The detection of lisinopril was performed in multiple reaction monitoring (MRM) mode using an ion trap mass spectrometer with an electrospray ion (ESI) source, positive ionisation (capillary 4000 V, nebulizer 70 psi (nitrogen), dry gas nitrogen at 12 L/min, dry gas temperature 350°C). The extracted ion current (EIC) chromatogram of m/z (245, 246, 291, 309) from m/z 406 was analyzed.

Standard solutions

A stock solution of lisinopril (0.963 mg/mL) was prepared by dissolving an appropriate quantity of lisinopril in methanol. Two working solutions (9.63 $\mu\text{g/mL}$ and 129 ng/mL, respectively) were prepared by appropriate dilution in drug-free human plasma. These solutions were used to prepare plasma calibration standards with the concentrations of 1.29, 2.58, 5.16, 10.32, 20.64, 41.29, 82.58 and 129.04 ng/mL. Quality control (QC) samples of 3.87 ng/mL (lower), 19.36 ng/mL (medium) and 51.62 ng/mL (higher) were prepared by adding the appropriate volumes of working solutions to drug-free human plasma. The resultant plasma calibration standards and quality control standards were pipetted into 15 mL polypropylene tubes and stored -20°C until analysis.

Sample preparation

Standards and plasma samples (0.25 mL) were deproteinized with 12% perchloric acid in water (0.05 mL). After vortex-mixture (10 s) and centrifugation (5 min at 5000 rpm), the supernatants (0.15 mL) were transferred in autosampler vials and 15 μ L were injected into the HPLC system.

Method validation

The specificity of the method was evaluated by comparing the chromatograms obtained from the plasma samples containing lisinopril with those obtained from different plasma blank samples (n=6).

The concentration of lisinopril was determined automatically by the instrument data system using peak areas and the external standard method. The calibration curve model was determined by the least squares analysis: $y = b + ax$, weighted (1/y) linear regression, where y - peak area of the analyte and x - concentration of the analyte (ng/mL).

The intra-day precision (expressed as coefficient of variation, CV %) and accuracy (expressed as relative difference between obtained and theoretical concentration, bias %) were determined by the analysis of five different samples (n = 5) from each QC standards (at lower, medium and higher levels) on the same day. The inter-day precision and accuracy were determined by analysis on five different days (n = 5) of one sample from each QC standards (at lower, medium and higher levels).

The lower limit of quantification (LLOQ) was established as the lowest calibration standard with an accuracy and precision less than 20%.

The relative recoveries (at LLOQ, lower, medium and higher levels) were measured by comparing the response of the spiked plasma with the response of standards in solvent with the same concentration of lisinopril as the plasma (n = 5).

The lisinopril stability in plasma at lower and higher levels (n=5) was investigated. For the post-preparative stability (PPS) study, the samples were prepared, analyzed immediately and after 12-24 h (kept in the autosampler of the HPLC system at 25°C). The concentrations were calculated against the same calibration curve. For the long-term stability (LTS) study, the samples were stored below -20°C and analyzed during 5 months. The concentrations were calculated against calibration curve of the day and the mean values for the stored samples were determined and compared. For the freeze-thaw stability (FTS) study, the samples were subjected to three cycles of freeze-thaw operations in three consecutive days. After the third cycle the samples were analyzed and the concentrations were calculated against calibration curve of the day. The requirement for the stability studies of the drug is that the difference between the mean concentrations of the tested samples in various conditions and the nominal concentrations was in $\pm 15\%$ range.

REFERENCES

1. S. E. Nielsen, T. Sugaya, L. Tarnow, M. Lajer, K. J. Schjoedt, A. S. Astrup, T. Baba, H. H. Parving, P. Rossing, *Diabetes Care*, **2009**, *32*, 1684.
2. A. K. Sjølie, N. Chaturvedi, *J. Hum. Hypertens*, **2002**, *16*, S42.
3. A.C. Moffat, M.D. Osselton, B. Widdop, "Clarke's Analysis of Drug and Poisons in pharmaceuticals, body fluids and postmortem material", Pharmaceutical Press, Inc, London, **2004**, 1180.
4. P. J. Worland, B. Jarrott, *J. Pharm. Sci.*, **1986**, *75*, 512.
5. H. J. Leis, G. Fauler, G. Raspotnig, W. Windischhofer, *Rapid Commun. Mass Spectrom.*, **1999**, *13*, 650.
6. Y. C. Wong, B. G. Charles, *J. Chromatogr. B Biomed. Appl.*, **1995**, *673*, 306.
7. O. Sagirli, L. Ersoy, *J. Chromatogr. B Analyt. Technol. Biomed. Life Sci.*, **2004**, *809*, 159.
8. N. Zhou, Y. Z. Liang, B. M. Chen, P. Wang, X. Chen, F. P. Liu, *J. Chromatogr. Sci.*, **2008**, *46*, 848.
9. B. M. Tashtoush, F. Q. Alali, N. M. Najib, *Pharmazie*, **2004**, *59*, 21.
10. A. Tsakalof, K. Bairachtari, M. Georgarakis, *J. Chromatogr. B Analyt. Technol. Biomed. Life Sci.*, **2003**, *783*, 425.
11. D. Mihiu, L. Vlase, S. Imre, C.M. Mihiu, M. Achim, D.L. Muntean, *Studia Universitatis Babeş-Bolyai, Chemia*, **2009**, *3*, 151.
12. M. Achim, D. Muntean, L. Vlase, I. Bâldea, D. Mihiu, S. E. Leucuța, *Studia Universitatis Babeş-Bolyai, Chemia*, **2009**, *3*, 7.
13. W. Qin, Z. Zhang, Y. Tian, F. Xu, N. Wang, Y. Chen, *Biomed. Chromatogr.*, **2007**, *21*, 415.
14. A. A. Padua, R. E. Barrientos-Astigarraga, V. M. Rezende, G. D. Mendes, G. De Nucci, *J. Chromatogr. B Analyt. Technol. Biomed. Life Sci.*, **2004**, *809*, 211.
15. J. Huang, Y. Xu, F. Liu, S. Gao, Q. Guo, *Rapid Commun. Mass Spectrom.*, **2006**, *20*, 248.
16. C. Kousoulos, G. Tsatsou, Y. Dotsikas, Y. L. Loukas, *Analytica Chimica Acta*, **2005**, *551*, 177.
17. Guidance for Industry, Bioanalytical Method Validation. U.S. Department of Health and Human Services, Food and Drug Administration. Federal Register, **2001**, 66.
18. Guidance on the Investigation of Bioavailability and Bioequivalence. The European Agency for the Evaluation of Medicinal Products, Committee for Proprietary Medicinal Products, **2001**, CPMP/EWP/QWP/1401/98

DETERMINATION OF AROMATIC AMINES AND PHENOLS BY KINETIC METHODS BASED ON LANDOLT EFFECT

LUCIAN COPOLOVICI^a, IOAN BALDEA^b, ALEXANDRA CSAVDARI^b

ABSTRACT. A simple kinetic method for the determination of aniline (and substituted anilines) and phenols in water has been set up. A Landolt type system has been employed, using the hydrogen peroxide - bromide reaction in acidic media, with aniline as a trap for bromine. The course of the reaction was followed potentiometrically. The plot of potential versus reaction time exhibits an inflexion point either in presence or absence of the analyte. It is similar to a titration curve, exhibiting a delay on the abscissa. The value of the difference Δt between end-point times for the sample and the blank is proportional to the concentration of the trapping agent. According to the initial rate method in kinetically based analytical determinations, it represents the base of calibration. The best operating conditions regarding ionic strength, pH, concentration range of reagents and temperature have been established. The method was checked for mixtures of anilines or aniline and phenol. Additive effects were found. No discrimination among individual components is possible by this method. Depending on the analyte, detection limits were in the range of 1.7 - 52 $\mu\text{g}\cdot\text{L}^{-1}$. Copper and iron ions interfere in the determination only at large concentrations.

Keywords: *kinetic methods, phenols, aromatic amines*

INTRODUCTION

Phenols and aromatic amines are byproducts of large-scale production and use of man-made organics such as drugs, dyes, antioxidants, paper pulp and pesticides. They cause ecologically undesirable effects[1]. Most phenols and anilines exhibit different toxicities; hence their determination is very important for evaluating the total toxicity of an environmental sample.

Current methods for the determination of anilines include spectrophotometric methods [2-4], gas chromatography-mass spectroscopy techniques [5-7], high-performance chromatography [8-12] and sensors [13, 14].

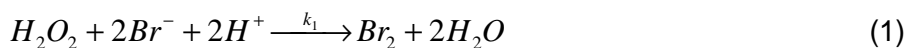
^a Present address: Estonian University of Life Sciences, Institute of Agricultural and Environmental Sciences, Kreutzwaldi 1, Tartu 51014, Estonia
E-mail: lucian.copolovici@emu.ee

^b Faculty of Chemistry and Chemical Engineering, "Babes-Bolyai" University Cluj-Napoca, 11 Arany Janos Str., 400028 Romania, e-mail: ibaldea@chem.ubbcluj.ro

Generally, phenolic compounds are subjected to chromatographic separation before detection [15-17]. However, the separation takes time, and often requires pre-concentration. In addition, the equipment is expensive and usually is not portable. Many biosensors have been developed in the past for phenol determination [18-25].

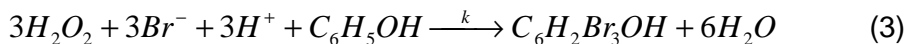
This paper shows that aromatic amines and phenols can be determined bromometrically in water samples, with bromine generated *in situ* by a redox reaction. Many such brominations of activated aromatic compounds use various bromides and oxidizing agents ($NH_4Br-H_2O_2$ [26], $NaBr-Oxone$ ($KHSO_5-KHSO_4$) [27], $HBr-H_2O_2$ [28, 29], $LiBr-Cerium$ ammonium nitrate [30]) or even heterogeneous catalysis [31, 32].

The proposed kinetic method is based on the following two formal reactions:



Reaction (2) can also be written with phenols. The bromination of the first-brominated compound can continue to second and/or third bromination. This type of bromination has been employed for synthetic purposes by using H_2O_2 and NH_4Br [26]. The rate constant for bromination reaction (2) is larger than that of reaction (1), where the brominating agent is formed, while the oxidation of aniline or phenols by hydrogen peroxide under the employed experimental conditions takes place slower as compared to process (1). Although further bromination takes place in consecutive steps, the substitution reactions are relatively rapid as compared to the brominating agent generation. Therefore, the couple of reactions (1) and (2) resemble a Landolt-type system.

The concentration of bromine is quite low, so that a steady-state is reached that depends on the nature of phenol or aniline. Different reactivity of aromatic amines or phenols towards bromine causes quite different steady-state concentration for this species. Under these steady-state conditions, the rate of nuclear bromination is independent of the substrate concentration, but depends on the nature of these species and the number of bromination steps. The overall stoichiometry for bromination of phenol molecules in a mixture of hydrogen peroxide - bromide ions in acidic media is given by:



It was determined experimentally, by using mixtures with increasing ratio of bromine/phenol, that tri-bromination has taken place. These findings confirmed previous research [33]. The same tri-bromination occurs with aniline. As shown above, the rate of nuclear bromination depends primarily on the nature, but not on the concentration of the analyte. The electrophile generation rate depends upon the H_2O_2 , Br^- and H^+ concentrations [34].

RESULTS AND DISCUSSION

Figure 1a shows the evolution of electromotive force vs reaction time for kinetic runs of the blank and in the presence of *para*-toluidine and 3-aminobenzenesulfonic acid.

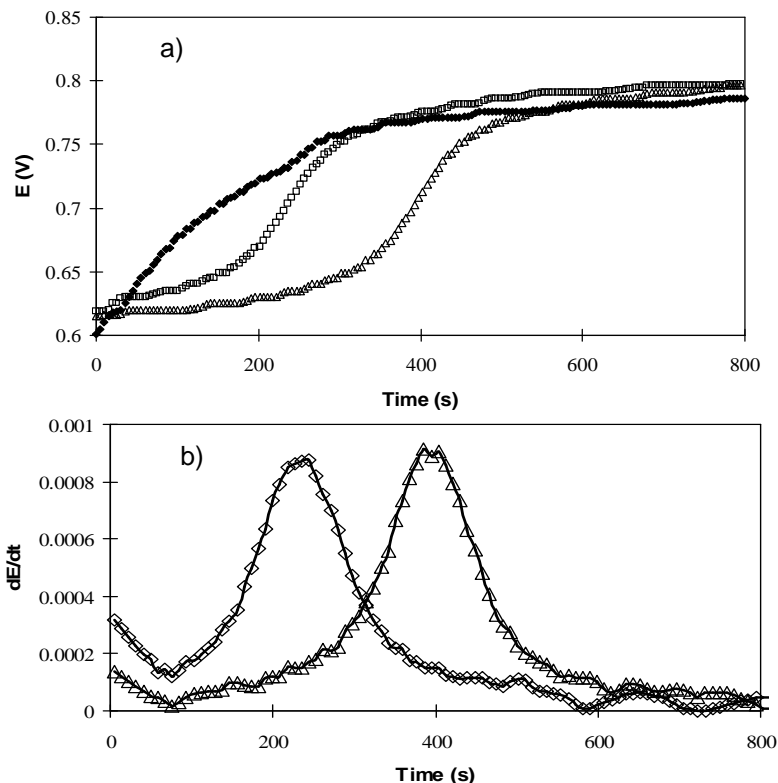


Figure 1. Electromotive force vs reaction time (a) and dE/dt (b) plots obtained in the determination of 0 (■), $2 \times 10^{-5} \text{ mol.L}^{-1}$ *para*-toluidine (◇) and 3-aminobenzenesulfonic acid (△). Other experimental conditions are described under Procedures.

The graph exhibits an inflexion point and has the shape of a titration curve. The so-called “titration agent” is generated in the reaction mixture at a well-established rate. Therefore, the abscissa is time instead of “titration agent volume”. The end-point is considered to correspond to the inflexion point on the curve. The time value at the inflexion is determined by derivation of the recorded curve (see Figure 1b). In fact, the complete consumption of the aromatic amine does not correspond to the inflexion point, but to the moment at which the electromotive force increases steeply. This corresponds to the extrapolation to the abscissa of the linear increase of E values around the

inflection point. It should be mentioned that the formation of bromine in the absence of the trapping agent (blank probe) is not instantaneous. It generates a similar curve. However, the inflection point is more precisely determined by derivation of the curves. Therefore, we have chosen this approach. The difference $\Delta t = t - t_0$ is proportional to the amount of pollutant in the mixture. The values t_0 and t stand for the end-point times of a reaction mixture in the absence and in the presence of the analyte, respectively. Because the indicator reaction behaves as a Landolt-type system, the reciprocal of Δt is directly related to the value of the rate. According to the initial rate method in kinetically based analytical determinations, the base of calibration is the plots Δt vs pollutant concentration.

Optimisation of conditions. To achieve the maximum possible sensitivity with the proposed kinetic method, we searched for the effect of a number of parameters such as pH, concentration of reactants, conversion of hydrogen peroxide and temperature. The quest for the best condition was carried out with respect to the determination of 3-aminobenzensulphonic acid and of phenol.

The effect of the H^+ concentration on the reaction rate is shown in Fig. 2a. Hydrogen ions affect the Landolt-type system, namely the rate of bromine generation. The shape of the curves is similar either in the presence or in absence of amines. First-order dependence with respect to the hydrogen ion has been confirmed by our data, because of the linearity of graphs in Figure 2a. From the point of view of the ionic strength (high enough to cover any contribution by an unknown sample) and the convenience of reaction rate determination the value of $0.1 \text{ mole}\cdot\text{L}^{-1}$ was chosen for further measurements.

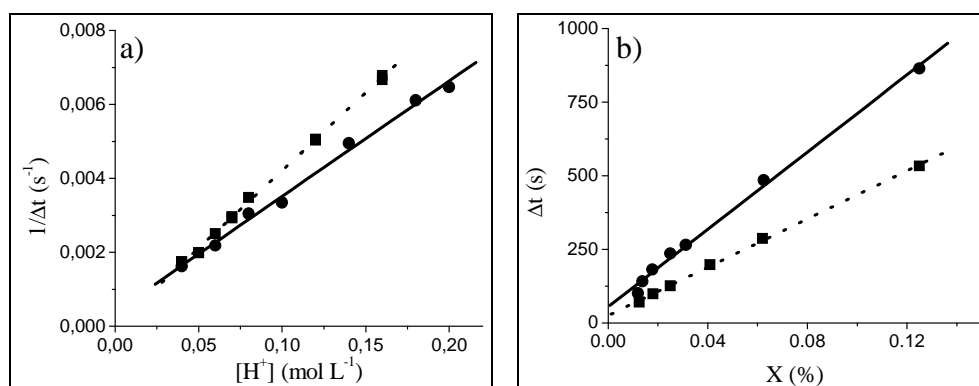


Figure 2. Influence of (a) $[H^+]$ and (b) conversion of H_2O_2 on kinetic determination of $2 \times 10^{-5} \text{ mol}\cdot\text{L}^{-1}$ phenol (■) and aminobenzensulphonic acid (●). Other experimental conditions are described under Procedures.

The conversion of hydrogen peroxide is defined by:

$$X = \frac{[H_2O_2]_0 - [H_2O_2]_{cont}}{[H_2O_2]_0} = \frac{\Delta[H_2O_2]}{[H_2O_2]_0} = \frac{[analyte]_0}{[H_2O_2]_0} \quad (4)$$

The effect of the conversion on the reaction rate at a 3-aminobenzensulphonic acid and phenol concentration of 2×10^{-5} mole·L⁻¹ is illustrated in Figure 2b. At low conversions, the end-point time is quite short to be precisely determined. At higher values, it is too long and the concentration of H_2O_2 smaller than that of the start of the reaction. This is caused by the H_2O_2 consumption by bromide and by self-decomposition. Moreover, the initial rate method cannot be used at large consumption [36]. A compromise should be made. We have chosen a value of 0.025 (2.5 %). It ensures practically a constant rate within this initial part of the reaction. The concentrations of H^+ , H_2O_2 and Br^- are almost constant.

The effect of temperature upon the reaction rate was examined in the range of 293–318 K. As expected, an Arrhenius-type dependence was observed. At higher values of temperatures, the decomposition of H_2O_2 becomes more important. A value of 298 K seems to be convenient for analytic measurements, either for reasonable rates of the process or for the negligible rates of side reactions.

Calibration curves. The electromotive force vs time curves recorded for different amounts of pollutant were analysed by the initial-rate method. Five aromatic amines: aniline, *para*-aminophenol, *para*-toluidine, 3-aminobenzensulphonic acid and *para*-iodoaniline and five phenols: phenol, resorcinol, hydroquinone, *ortho*-cresol and β -naphthol were examined. Data relevant for calibration graphs, covering the concentration range of two orders of magnitude (10^{-6} – 10^{-5} mol·L⁻¹), are summarised in Table 1. The detection limit was computed as recommended by IUPAC. *R* stands for the correlation factor.

The sensitivity, defined as the slope of the calibration lines (see Table 1), is good and depends on the nature of the analyte. The precision of the proposed method was checked on seven samples containing $2.0 \cdot 10^{-5}$ mol·L⁻¹ phenol. The relative standard deviation was 3.2 %.

Effects of interfering species. The interfering effect of some metal ions and organic compounds associated with pollutants in wastewater was studied. The results are summarised in Table 2 for determination of phenol.

The following ions do not modify the rate of electrophile generation: Zn(II), Cd(II), Ni(II), Mo(VI), V(V), Fe(III), Cu(II). Their effect upon the amine determination is negligible. However, we noticed that copper ion interferes in reaction at relatively large concentrations. Cu(II) has a catalytic effect upon the decomposition of hydrogen peroxide and possibly on the oxidation of bromide by hydrogen peroxide.

Table 1. Features of calibration graphs for the determination of some aromatic compounds

Analyte	Linear regression Δt = end-point time (s); C = molar concentration (mole·L ⁻¹)	R/ nr. points	Detection limit·10 ⁷ (mol·L ⁻¹)
Amines			
Aniline	$\Delta t = (-0.4 \pm 9.5) + (179 \pm 8) \cdot 10^6 \cdot C$	0.995/12	0.1
3-Aminobenzen-sulphonic acid	$\Delta t = (11 \pm 6.2) + (12.1 \pm 0.2) \cdot 10^6 \cdot C$	0.999/9	1.6
<i>para</i> -Amino phenol	$\Delta t = (16 \pm 26) + (54.7 \pm 0.5) \cdot 10^6 \cdot C$	0.999/9	0.4
<i>para</i> -Toluidine	$\Delta t = (17.2 \pm 13) + (11.6 \pm 0.3) \cdot 10^6 \cdot C$	0.999/9	1.7
<i>para</i> -Iodaniline	$\Delta t = (2.8 \pm 3.4) + (14.8 \pm 0.3) \cdot 10^6 \cdot C$	0.999/11	1.3
Phenols			
Phenol	$\Delta t = (-3.1 \pm 3.1) + (8.5 \pm 0.2) \cdot 10^6 \cdot C$	0.998/18	2.3
<i>ortho</i> -Cresole	$\Delta t = (-0.9 \pm 2.3) + (5.7 \pm 0.2) \cdot 10^6 \cdot C$	0.998/11	3.5
Hidroquinone	$\Delta t = (-0.9 \pm 2.3) + (5.5 \pm 0.2) \cdot 10^6 \cdot C$	0.999/9	3.6
Resorcine	$\Delta t = (-1.2 \pm 4.8) + (20.2 \pm 0.4) \cdot 10^6 \cdot C$	0.999/11	0.9
β -Naphthol	$\Delta t = (0.4 \pm 3.9) + (0.86 \pm 0.06) \cdot 10^6 \cdot C$	0.995/7	23.0

Table 2. Tolerance limit for various organic compounds and ions on the determination of 2×10^{-5} mol·L⁻¹ phenol

Interfering species	Tolerance limit ratio (mole/mole)
oxalic acid, isopropyllic acid, ethanol, methanol	400
Zn(II), Cd(II), Ni(II), Mo(VI), V(V), KCl, EDTA	200
Fe(III), Cu(II)	90
Vitamin B ₁₂	100
cysteine, methionine, ascorbic acid, acetylsalicylic acid, paracetamol, vitamin B ₆ , vitamin B ₂	1

*maximum limit tested

The most serious interference in these analyses was caused by: *B* vitamins, acetylsalicylic acid and ascorbic acid. These react with bromine in the same manner as the aromatic amines and phenols.

All aromatic amines and all phenols employed in the study react similarly. Therefore, no discrimination among them is possible in mixtures. This constitutes a drawback of the method.

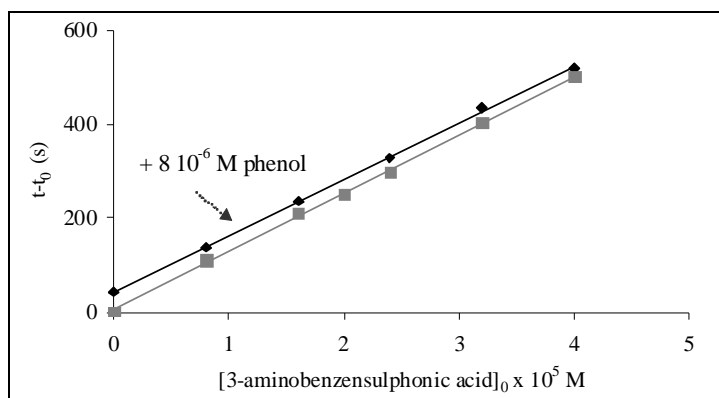


Figure 3. Calibration line in the absence and presence of a constant concentration of phenol ($8 \times 10^{-6} \text{ mol.L}^{-1}$). Other experimental conditions are described under Procedures.

Nevertheless, a mixture of two analytes can be determined as a sum. If a known and constant concentration of phenol and increasing concentrations of 3-aminobenzensulphonic acid are used in calibration, the obtained calibration lines are parallel. This is illustrated in Figure 3 and indicates the additivity of the end-point times. The same behaviour has been observed for *p*-toluidine and 3-aminobenzensulphonic acid mixtures.

Table 3. Recovery of aniline added or determined concentration in waste-water

Sample provenience	[aniline] ₀ × 10 ⁶ (M)			Recovery (%)
	added	Standard Method [37]	Kinetic method	
River water with added aniline	1.58	1.60	1.52	101.3/96.2
	4.17	4.10	4.15	98.3/99.5
	8.35	8.32	8.28	99.6/99.1
Several samples of wastewater		7.1	7.22	100.7
		3.5	3.61	103.1
		1.7	1.62	95.3
		0.60	0.63	105.0
		1.30	1.26	96.9
		2.20	2.15	97.7
		2.30	2.29	99.6
	3.40	3.41	100.3	

Testing on some real samples. The aniline content in several samples of waste-water from S.C. Sinteza Oradea S.A. was determined by our technique. Results were compared to those obtained by means of the Romanian Standard for determination of aniline in surface and waste-waters. This is an equilibrium

spectrophotometrical method and relies on the oxidative coupling of amine with phenol in the presence of chloramine T to yield an indophenol dye [37]. Some measurements have been carried out by adding known amounts of aniline to previously analysed river water samples. These contained micromolar amounts of: Fe(II), Fe(III), Cu(II) and Mn(II), respectively. The recoveries were calculated relative to this method and the results are presented in Table 3. They correspond to mean values of at least three replicate experiments and range between 95% and 105 %, proving the proposed kinetic method is reliable.

EXPERIMENTAL SECTION

Reagents. Analytical-grade and commercially available chemicals were used without further purification, with the exception of phenol. Solutions were prepared first in deionised and four-distilled water and, after the study of various effects, only in twice-distilled water. Precautions taken at the beginning of the study, concerning the interference of metal ions, proved to be not entirely necessary. Stock solutions ($1.0 \times 10^{-3} \text{ mole} \cdot \text{L}^{-1}$) were prepared from the aromatic amines and phenol in ethanol. The phenol solution was prepared from freshly purified stuff (distillation under low pressure; m.p. $40.5 - 41.5^\circ\text{C}$).

Perchloric acid ($0.5 \text{ mole} \cdot \text{L}^{-1}$) and potassium bromide ($0.5 \text{ mole} \cdot \text{L}^{-1}$) were prepared in de-ionised and twice-distilled water. Hydrogen peroxide solution ($8.0 \cdot 10^{-2} \text{ mol} \cdot \text{L}^{-1}$) was freshly prepared before each set of runs and standardised by common titration with permanganate.

Apparatus. The instrumental set-up was described in detail previously [35]. It consists of a temperature controlled reaction vessel. The measuring electrode was a platinum plate, the electromotive force being measured against a saturated calomel electrode by means of a potentiometer (Digitronix, DXP 2040). The latter is connected to a 32-bit Hewlett-Packard analogue-digital converter and a DTK computer.

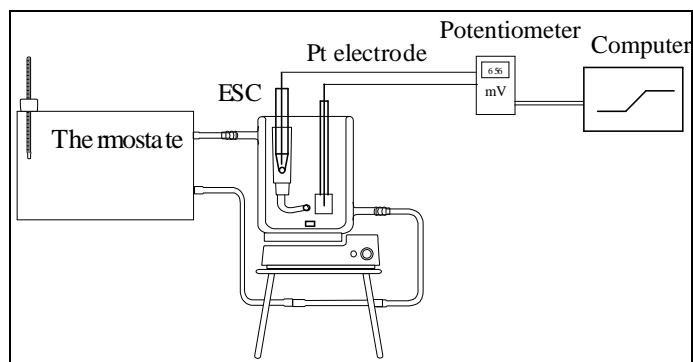


Figure 4. Experimental device

Procedure. Various aliquots of standard aniline or phenol solution, 5.0 mL of 0.5 mole·L⁻¹ HClO₄ and 5.0 mL of 0.5 mole·L⁻¹ KBr were placed in a 50-mL reaction vessel and accurately diluted to 20 mL. The reaction was initiated by rapid addition of 5 mL solution of hydrogen peroxide 8.0x10⁻² mole·L⁻¹ by means of a syringe. The progress of reaction was monitored potentiometrically and kinetic data (electromotive force vs reaction time) were collected and processed. Each measurement was carried out at least in triplicate.

CONCLUSIONS

The proposed method is simple, cheap and permits the determination of low concentrations of aromatic amines or phenols if only one species is present in the sample. If it contains more compounds, the total concentration of the pollutants can be determined as a sum. Depending on the analyte, detection limits range between 1.7 and 52 µg·L⁻¹. Data acquisition by means of a personal computer facilitates data collection and processing. Transition metals do not interfere at concentration levels usually encountered in surface or wastewater.

ACKNOWLEDGEMENT

Financial support of Romanian National University Research Council (CNCSIS) is gratefully acknowledged by the authors.

REFERENCES

1. S. Canofeni, S. Disario, J. Mela, R. Pilloton, *Anal. Lett.*, **1994**, 27, 1659.
2. N. A. Zatar, A. Z. Abu-Zuhri, A. A. Abu-Shaweesh, *Talanta*, **1998**, 47, 883.
3. A. Labudzinska, K. Gorczynska, *Analyst*, **1994**, 119, 1195.
4. L. Copolovici, L. Baldea, *Anal. Bioanal. Chem.*, **2002**, 374, 13.
5. K. J. Chia, S. D. Huang, *J. Chromatogr. A*, **2006**, 1103, 158.
6. M. Akyuz, S. Atu, *J. Chromatogr. A*, **2006**, 1129, 88.
7. C. H. Deng, N. Li, L. Wang, X. M. Zhang, *J. Chromatogr. A*, **2006**, 1131.
8. L. Cardenes, A. Martin-Calero, J. H. Ayala, V. Gonzalez, A. M. Afonso, *Anal. Lett.*, **2006**, 39, 405.
9. X. N. Cao, J. H. Li, H. H. Xu, J. R. Zhan, L. Lin, K. Yamamoto, L. T. Jin, *Chromatographia*, **2004**, 59, 16.
10. J. W. Blythe, A. Heitz, C. A. Joll, R. I. Kagi, *J. Chromatogr. A*, **2006**, 1102, 73.
11. M. I. Evgen'ev, I. I. Evgen'eva, F. S. Levinson, E. A. Ermolaeva, Y. R. Valitova, *J Anal. Chem*, **2006**, 61, 133.

12. Y. Zhu, M. H. Wang, H. Y. Du, F. Wang, S. F. Mou, P. R. Haddad, *J. Chromatogr. A*, **2002**, 956, 215.
13. M. Wimmerova, L. Macholan, *Biosens. Bioelectron.*, **1999**, 14, 695.
14. A. Ferancova, E. Korgova, J. Labuda, J. Zima, J. Barek, *Electroanal*, **2002**, 14, 1668.
15. M. Kladi, M. Dassenakis, M. Scoullou, N. Psaroudakis, *Fresen. Environ. Bull.*, **2006**, 15, 1003.
16. A. Asan, I. Isildak, *J. Chromatogr. A*, **2003**, 988, 145.
17. M. S. Zhang, A. M. Wang, *Chinese Anal. Chem.*, **1999**, 27, 63.
18. S. L. Mu, *Biosens. Bioelectron.*, **2006**, 21, 1237.
19. Z. H. Dai, X. X. Xu, L. Wu, H. X. Ju, *Electroanal.*, **2005**, 17, 1571.
20. N. Li, M. H. Xue, H. Yao, J. J. Zhu, *Anal. Bioanal. Chem.*, **2005**, 383, 1127.
21. Q. Zhao, L. H. Guan, Z. N. Gu, Q. K. Zhuang, *Electroanal.*, **2005**, 17, 85.
22. H. H. Yu, S. Q. Liu, H. X. Ju, *Biosens. Bioelectron.*, **2003**, 19, 509.
23. J. Kulys, R. Vidziunaite, *Biosens. Bioelectron.*, **2003**, 18, 319.
24. S. C. Chang, K. Rawson, C. J. McNeil, *Biosens. Bioelectron.*, **2002**, 17, 1015.
25. Y. I. Korenman, S. A. Tunikova, N. V. Belskikh, M. Bastic, L. Rajakovic, *J. Anal. Chem.*, **1997**, 52, 278.
26. K. Mohan, N. Narender, P. Srinivasan, S. J. Kulkarni, K. V. Raghavan, *Synthetic Commun.*, **2004**, 34, 2143.
27. C. K. Lee, B. S. Koo, Y. S. Lee, H. K. Cho, K. J. Lee, *B. Kor. Chem. Soc.*, **2002**, 23, 1667.
28. N. B. Barhate, A. S. Gajare, R. D. Wakharkar, A. V. Bedekar, *Tetrahedron Lett.*, **1998**, 39, 6349.
29. R. Neumann, I. Assael, *Chem. Commun.*, **1988**, 1285.
30. S. C. Roy, C. Guin, K. K. Rana, G. Maiti, *Tetrahedron Lett.*, **2001**, 42, 6941.
31. T. Esakkidurai, M. Kumarraja, K. Pitchumani, *Catal. Lett.*, **2004**, 92, 169.
32. D. P. Das, K. Parida, *Catal. Commun.*, **2006**, 7, 68.
33. A. W. Francis, A. J. Hill, *J. Am. Chem. Soc.*, **1924**, 45, 2498.
34. S. U. Kreingold, L. V. Lavrelashvili, I. M. Nelen, *J. Anal. Chem. USSR*, **1982**, 37, 1441.
35. S. Bungau, I. Baldea, L. Copolovici, *Rev. Chim. Bucharest*, **2003**, 54, 213.
36. H. A. Mottola, "Kinetic aspects of analytical chemistry", (Vol. 96 of the Series "Chemical Analysis"), John Wiley&Sons, New-York, **1988**, pg. 20; A. Csavdári, "Catalytic Kinetic Methods in Analytical Chemistry. Principles and applications", **2008**, Editura MEGA, Cluj-Napoca.
37. ***, STAS 8507-70, "Eaux de surface et eaux usees. Dosage de l'aniline"; V. G. Amelin *J. Anal. Chem.*, **2002**, 57, 733; J. F. Van Bocxlaer, K. M. Clauwaert, W. E. Lambert and A. P. De Leenheer, *Clin. Chem.*, **1997**, 43, 627.

RADIOCARBON DATING OF THE HISTORIC OAK OF TEBEA, ROMANIA

ADRIAN PATRUT^{a,*}, KARL F. VON REDEN^b, DANIEL A. LOWY^c,
SALVINA PASCA^d, LASZLO KEKEDY-NAGY^a, IRINA SOVAGO^a

ABSTRACT. Two wood samples originating from the historic pedunculate oak (*Quercus robur*) of Tebea, Romania, which died in 2005, were processed and radiocarbon dated by AMS for determining the age of the tree. The radiocarbon date of the oldest sample was 503 ± 25 BP, which corresponds to a calibrated calendar age of 580 ± 10 years. Taking into account the original position of this sample in the hollow trunk, one can estimate that the historic tree was around 800 years old.

Keywords: radiocarbon dating, accelerator mass spectrometry, pedunculate oak, age determination, calibration curve.

INTRODUCTION

For trees from temperate zones, especially gymnosperms, ages in the pith/centre or in different points of tree trunks are determined by ring counting. This is performed on fallen logs or remaining stumps of dead trees, as well as on thin cores extracted from the exterior of the trunks of live trees. Therefore, when possible, ring counting is the most accurate and reproducible method for age and growth rate determination [1].

By contrast, for many old angiosperm trees, with large cavities in their trunk, the problem of age determination is a significantly more difficult task. For such old and hollow broadleaf trees, without a continuous ring sequence in the trunk, ring counting is of very limited value and is replaced by alternative direct (radiocarbon dating) or indirect dating methods (relation size/diameter-age, projections of short-term growth data, projections based on mortality rates etc.). Indirect dating methods can provide, however, only very approximate and questionable results. Therefore, radiocarbon dating of wood samples collected from the trunk represents the only alternative method for accurately aging these

^a Babes-Bolyai University, Faculty of Chemistry and Chemical Engineering, 11 Arany Janos, RO-400028, Cluj-Napoca, Romania

* Email: apatrut@gmail.com

^b NOSAMS Facility, Department of Geology & Geophysics, Woods Hole Oceanographic Institution, 360 Woods Hole Rd., Mailstop 8, Woods Hole, MA 02543, U.S.A.

^c FlexEl, LLC, College Park, MD 20742, U.S.A.

^d "Avram Iancu" General School, RO-337005 Baia de Cris, Romania

trees. This method determines the ^{14}C (radiocarbon) content relative to stable carbon [2, 3]. Due to its higher costs, so far radiocarbon dating of broadleaf trees was not used on the large scale. Several noteworthy investigations were performed, however, on different tree species, to determine the age of trees and/or growth rates or to provide climate information [4, 5].

The pedunculate oak (*Quercus robur*) and its close relative, the sessile oak (*Quercus petraea*), are the most representative and widespread European species of the genus *Quercus*, which belongs to the family Fagaceae. The two species, especially the pedunculate oak are usually considered to be the most longlived European deciduous trees. Their age limit is still controversial, even if modern tree researchers consider that the age of the oldest oaks is probably close to 1,000 years [6, 7].

Here we report the AMS (accelerator mass spectrometry) radiocarbon dating results of two wood samples that originate from the historic pedunculate oak of Țebea, Romania, which died in 2005.



Figure 1. The drawing from the late 19th century showing the historic oak of Țebea and the tomb of Avram Iancu.

RESULTS AND DISCUSSION

The historic oak of Țebea and its location

The historic oak, known as “*gorunul lui Horea*”, i.e., the sessile oak of Horea, even if it is in fact a pedunculate oak, was the most popular and famous

Romanian tree. Its fame arises from the fact that under its canopy, Horea, the main leader of the Revolt of 1784-1785, addressed his local force of serfs, known as “moți”. Horea called to battle against the feudal serfdom and for political equality between Romanians and other ethnicities in Transylvania. In 1872, Avram Iancu, another Romanian hero, who played an important role in the local chapter of the Austrian Empire Revolutions of 1848–1849, was buried by this tree.

The oak is located in the Heroes' Cemetery of the village Țebea, in the rural community Baia de Criș, Hunedoara county, in the north-western part of Romania. Its GPS coordinates are 46°10.213' N, 022°42.842' E, the altitude is 269 m and the mean annual rainfall in the area is 680 mm.

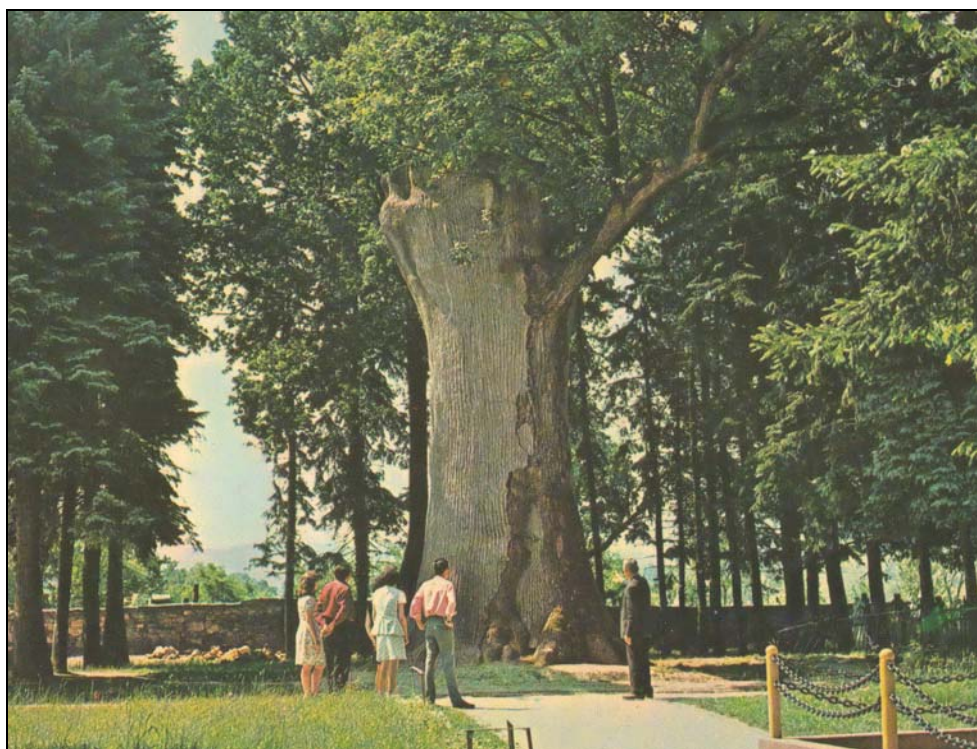


Figure 2. The photo taken in 1975 shows the remaining trunk of and the new branch which emerged from a high cut. The bark decline is obvious.

An ink drawing from the late 19th century (Figure 1) shows the large oak from Țebea, with a height of ca. 20 m, in a decline phase with several dry branches in its canopy. The decline of the tree worsened dramatically in the first decades of the 20th century; it was suffering probably from the complex disease called today “dieback of pedunculate oak”. In this disease, a number of biotic and abiotic agents interact to bring about a severe deterioration of the tree condition [8]. The foliage of the oak became very

thin, almost all branches died and large fissures appeared in the bark of its trunk. In order to save the historic tree from complete decay and drying out, the Romanian authorities decided to cut completely the trunk at a height of 9 m from the ground. The remaining trunk was secured with steel rings and its interior, which was partially hollowed, was cemented.

Over the next years, the oak recovered partially and from a high cut of the trunk developed a vigorous branch (Figure 2). However, the decline of the trunk could not be stopped, due also to the old age of the tree. The bark of the trunk continued fissuring and falling off. In 1977-78, for preventing the collapse of the tree, the trunk was encased in a concrete sarcophagus, which reconstituted its outline, retaining part of the original bark. In July 2005, during a violent storm, which affected many trees in the area, the single branch of the oak broke off. This is how the legendary oak died.



Figure 3. The image shows the remains of the dead oak, with the trunk encased in the concrete sarcophagus. The remaining original bark is visible on the left side of the photo.

The concrete sarcophagus damaged by the storm was rebuilt and it still incorporates ca. 10-15 % of the original bark in the exterior, while the interior is cemented and contains some original wood (Figure 3). Its circumference at breast height (cbh; 1.30 m above ground level) is of 9.90 m. This value can

be considered very close to the original cbh value of the trunk outside bark.

Two small wood samples originating from the upper part of the trunk, which was removed in 1924 were pretreated and investigated by AMS radiocarbon analysis.

AMS results and calibrated ages

Fraction modern values and radiocarbon dates of the two samples are listed in Table 1. Radiocarbon dates and errors were rounded to the nearest year. Calibrated (cal) ages, which were derived directly from fraction modern values, are also presented in Table 1. The 1- σ probability distribution was chosen to calculate calibrated age ranges. For sample 1, the 1- σ distribution corresponds only to one range. On the other hand, for sample 2, the 1- σ distribution corresponds to two ranges of calendar years. The confidence interval of one range (marked in bold) is much greater than of the other and it was selected as the most probable cal AD range.

For obtaining single calendar age values of samples, we derived a mean calendar age of each sample from the 1- σ range with the highest probability. Calendar ages of samples represent the difference between AD 2005 (when the tree died) and the mean value of the selected 1- σ range, with the corresponding error. Calendar ages of samples and errors were rounded to the nearest 5 years. The plotted OxCal calibration for the oldest sample is displayed in Figure 4. The radiocarbon dates of the investigated samples were found to be of 503 ± 25 BP ($fm = 0.9393 \pm 0.0031$) and 291 ± 26 BP ($fm = 0.9644 \pm 0.0033$). These values correspond to calibrated calendar ages of 580 ± 10 years and 455 ± 25 years, respectively.

Table 1. AMS dating results and calibrated calendar ages

Sample code	Fraction modern [error]	Radiocarbon date [error] (^{14}C yr BP)	Cal AD range(s) 1- σ [confidence interval]	Sample age ⁽¹⁾ [error] (cal yr)
1	0.9393 [± 0.0031]	503 [± 25]	1414-1435 [68.2%]	580 [± 10]
2	0.9644 [± 0.0033]	291 [± 26]	1522-1574 [46.5%] 1628-1650 [21.7%]	455 [± 25]

⁽¹⁾ In 2005

Age of the tree

In order to determine the age of the oak of Tebea, it is necessary to take into account the original position of the oldest sample, which was 580 ± 10 years old. As we mentioned above, the sample originates from a height of 9 m, from the removed upper part of the trunk. The main problem is to extrapolate the age of the oldest sample in the pith/center, by considering its position in a cross-section of the trunk at the height of 9 m. The only

information we have from 1924, when the hollow trunk of the oak was cut at 9 m above ground, is that it had only a thin layer of wood at the base, while at the cut height it was more than half empty. Therefore, in a conservative estimate, we can consider that the trunk was only half empty at the cut height and that the sample was collected from a cavity wall. In this case, the sample would originate from the midway between the center and the outside part/bark of the trunk.

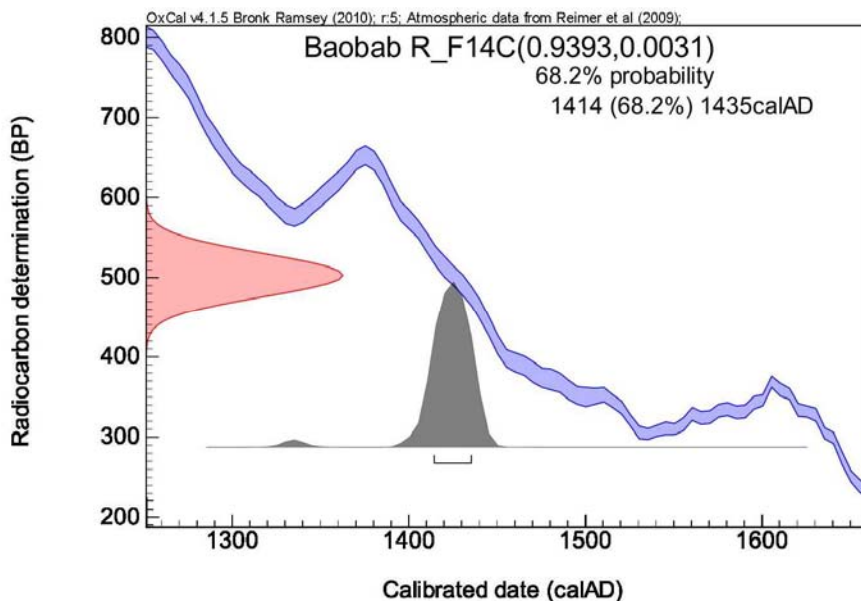


Figure 4. The plotted OxCal calibration for sample 1.

For establishing the true age of the tree, we must determine at what age did the old oak of *Tebea* reach half the trunk radius it had in 1924. By considering the literature data on the growth rate dynamics of large deciduous broadleaf trees, especially oaks, during their life cycle and the decline of the mean annual increase in radius with age [3, 14], we estimate that the tree needed around 200-250 years of growth to reach half of its trunk radius in 1924. This value must be added to the determined sample age of 580 years, to find out the age in the pith/center of the trunk at a height of 9 m above ground. An additional value of at least 20-30 years, which is necessary to a pedunculate oak to reach a height of 9 m, must be also added for determining the true age of the tree.

According to these estimates, the investigated tree was around 800 years old in 2005, when it died. Thus, one can state that the historic pedunculate oak of *Tebea* had started growing around AD 1200.

CONCLUSIONS

Two samples originating from the historic pedunculate oak of Tebea were investigated by AMS radiocarbon analysis. According to the dating results and by considering the original position of the oldest sample, we estimate that the tree, which died in 2005, started growing around AD 1200.

This research is the first radiocarbon dating of a Romanian tree.

EXPERIMENTAL SECTION

Sample preparation. The acid-base-acid pretreatment method [9] was used to remove soluble and mobile organic components. The resulted cellulose samples were combusted to CO₂ by the closed tube combustion method [10]. Then, CO₂ was reduced to graphite on iron catalyst, under hydrogen atmosphere [11]. Eventually, the graphite samples were analyzed by AMS.

AMS measurements. Radiocarbon measurements were performed at the National Ocean Sciences AMS Facility of the Woods Hole Oceanographic Institution, with a 3 MV Tandatron (TM) AMS system. The surface of the graphite samples was sputtered with cesium ions and the secondary negative ions were extracted and accelerated in the AMS system. ¹²C and ¹³C ions were measured in Faraday cups, where a ratio of their currents was recorded. Simultaneously, ¹⁴C ions were recorded in a solid state detector, so that instantaneous ratios of ¹⁴C to ¹²C were also recorded. The raw signals were compared to ratios obtained with a known standard material (Oxalic Acid I, NIST-SRM-4990) and converted to a fraction modern value. Fraction modern values, corrected for isotopic fractionation with the normalized $\delta^{13}\text{C}$ value of -25 ‰, were ultimately converted to radiocarbon dates, expressed in years BP (radiocarbon years before present, i.e., before AD 1950).

Calibration. Fraction modern values were calibrated and converted into calendar ages with the OxCal v4.1.5 for Windows [12], by using the IntCal09 atmospheric data set [13].

ACKNOWLEDGEMENTS

This research is based on work supported by a grant from the Romanian National University Research Council (PN II – IDEI No. 1092/2354) and also by U.S. National Science Foundation under Cooperative Agreement OCE-022828996.

REFERENCES

1. S.E. Nash, "Time, Trees and Prehistory: Tree-Ring Dating and the Development of North American Archaeology", University of Utah, Salt Lake City, **2003**.
2. M. Worbes, *Dendrochronologia*, **2002**, 20, 217.

3. A. Patrut, K.F. von Reden, D.A. Lowy, D.H. Mayne, K.E. Elder, M.L. Roberts, A.P. McNichol, *Nuclear Instr. and Meth. B*, **2010**, 268, 910.
4. A. Patrut, K.F. von Reden, D.A. Lowy, A.H. Alberts, J.W. Pohlman, R. Wittmann, D. Gerlach, L. Xu, C.S. Mitchell, *Tree Physiol.*, **2007**, 27, 1569.
5. A. Patrut, K.F. von Reden, D.A. Lowy, P. Lindeque, A.H. Alberts, R. Wittmann, E. Forizs, D. Margineanu, J. Pohlman, L. Xu, D. Gerlach, C.S. Mitchell, *Studia Univ. Babeş-Bolyai, Chem.*, **2006**, 51, 71.
6. P.H. Raven, G.B. Johnson, J.B. Losos, S.R. Singer, "Biology: Seventh Edition", McGraw Hill, New York, **2005**.
7. A. le Hardy de Beaulieu, T. Lamant, "Le guide illustré des chênes", Vol. 1-2, Huitième, Paris, **2007**.
8. J.N. Gibbs, B.J.W. Greig, *Forestry*, **1997**, 70, 399.
9. I.U. Olsson, in B. Berglund (ed.), "Handbook of Holocene palaeoecology and palaeohydrology", Wiley, Chichester, **1986**, p. 273.
10. Z. Sofer, *Anal. Chem.*, **1980**, 52, 1389.
11. J.S. Vogel, J.R. Southon, D.E. Nelson, T.A. Brown, *Nuclear Instr. and Meth. B*, **1984**, 5, 289.
12. C. Bronk Ramsey, *OxCal Program, v4.1.5*, **2010**, <http://www.rlaha.ox.ac.uk/oxcal/oxcal.html>.
13. P.J. Reimer, M.G.L. Baillie, E. Bard, A. Bayliss, J.W. Beck, P.G. Blackwell, C. Bronk Ramsey, C.E. Buck, G.S. Burr, R.L. Edwards, M. Friedrich, P.M. Grootes, T.P. Guilderson, I. Hajdas, T.J. Heaton, A.G. Hogg, K.A. Hughen, K.F. Kaiser, B. Kromer, F.G. McCormac, S.W. Manning, R.W. Reimer, D.A. Richards, J.R. Southon, S. Talamo, C.S.M. Turney, J. van der Plicht, C.E. Weyhenmeyer, *Radiocarbon*, **2009**, 51,1111.
14. A J. Godet, "Collins guide to the trees of Britain and northern Europe", Collins, London, **1986**.

ANTIOXIDANT CAPACITY DETERMINATION BY THE BRIGGS-RAUSCHER OSCILLATING REACTION IN A FLOW SYSTEM

An application of functional dynamics in analytical chemistry

NORBERT MUNTEAN^a, IOAN BÂLDEA^a, GABRIELLA SZABÓ^a,
ZOLTÁN NOSZTICZIUS^b

ABSTRACT. A new method to determinate the antioxidant capacity by means of Briggs-Rauscher system under flow conditions is being described. The basis of this method is a continuous perturbation of an oscillating system performed in a continuously fed stirred tank reactor (CSTR) by an inlet flow of an antioxidant solution, namely resorcinol. Under proper experimental conditions the amplitude and the time period of the oscillations will be strongly affected by the concentration of the antioxidant inflow. In our experiments the amplitude and the frequency of the oscillations followed a supercritical Hopf bifurcation scenario where the resorcinol concentration plays the role of the bifurcation parameter. Switching between pure water and resorcinol solutions can be performed many times, applying standard solutions of the antioxidant or the analyte providing data for the calibration curve or for the actual measurement.

Keywords: *Briggs-Rauscher oscillating reaction, inhibitory effect, CSTR, analytical method, resorcinol*

INTRODUCTION

Kinetic methods of analysis are currently regarded as highly effective tools in analytical chemistry for both the kinetic determination of a single species and the simultaneous kinetic determination of several species in a mixture with no prior separation. The dynamic regime of the chemical process involved in these methods is mainly monotonic; however, various types of dynamic regime have been explored in recent years in order to characterize non-linear chemical phenomena in the context of theoretical and experimental chemical kinetics [1].

^a Department of Physical Chemistry, "Babeș-Bolyai" University, Cluj-Napoca, 11 Arany Janos Str. Romania, RO-400028. E-mail: gszabo@chem.ubbcluj.ro

^b Center for Complex and Nonlinear Systems and the Department of Physics, Budapest University of Technology and Economics, H-1521 Budapest, Hungary

These non-linear phenomena, known as oscillating chemical reactions, include regular oscillations, period doubling, quasi-periodicity and deterministic chaos, among others [2-5]. These phenomena usually depend strongly on certain parameters of the system. Functional dynamics applies that parameter dependence to measure the actual values of the parameters after a calibration procedure.

Oscillating chemical reactions are complex systems involving a large number of chemical species as reactants, products, and intermediates that interact via unusual mechanisms. The Briggs-Rauscher (BR) reaction is one of the most spectacular oscillating reactions, which is a hybrid of the well-known Belousov-Zhabotinsky and the Bray-Liebhafsky reactions. The net chemical transformation of the BR reaction is the oxidation and iodination of malonic acid by hydrogen-peroxide and iodate ion, catalyzed by manganous ion in acidic media [6].

An oscillating reaction is very sensitive to small perturbation and this behavior is used in several analytical determinations, like the antioxidant capacity [7] of various chemical compound or some plants extract. The basis of this analytical method is that various antioxidants, for example resorcinol, change the dynamics of the BR reaction fundamentally by suppressing the oscillations even in a surprisingly low concentration (usually in a few micromoles/liter) [8-12].

The BR reaction method is based on the inhibitory effects by antioxidant scavengers of free radicals on the oscillations of the BR reaction. Free radicals can play an important role in the BR reaction, e.g. the strong CO and CO₂ evolution discovered recently in the reaction [9] has also a radical mechanism [13]. The generated hydroperoxyl radicals (HOO·) are among the main intermediates of the BR system. The mechanism of the action of antioxidants against HOO· radicals in the BR system has recently been described [10, 14]. When antioxidant scavengers of free radicals are added to an active oscillating BR mixture there is an immediate quenching of the oscillations, an inhibition time that linearly depends on the concentration of the antioxidant. The inhibition time is defined as the time elapsed between the end of the addition of the antioxidant and the first regenerated oscillation.

Based on these results a new analytical method was developed for the determination of the antioxidant activity of free radical scavengers.

It is a disadvantage of the method that a re-start of the oscillating regime is necessary each time before a new determination if a chemical oscillator like the BR is applied in a batch reactor.

The analyte pulse perturbation (APP) technique is performed in a continuous-flow stirred tank reactor (CSTR). Injecting a small amount of an analyte into the reactor causes a transient modification of the oscillator properties (affecting its amplitude and/or the period). It was first proposed by Jimenez-Prieto et al [15-16].

They applied the $\text{H}_2\text{O}_2\text{-NaSCN-CuSO}_4$ system in an alkaline medium which is an oscillatory system in CSTR as it was discovered by Orban [17]. The CSTR technique allows a system to be kept oscillating for a long time (as long as we have reactants, usually for several hours) and thus be employed as an inexhaustible indicator system for successively added samples and/or standards. Up to now, the usefulness of the APP technique has been demonstrated with various oscillating reaction for the determination of several chemical substances, for example heavy metal ions in aqueous solution, reduced glutathione, gallic acid [18-23].

No similar technique was developed, however, until now to determinate the antioxidant capacity with BR reactions in a CSTR. The aim of this paper is to present such a new determination possibility of antioxidant capacity using an active BR mixture in CSTR. To this end a mini-CSTR with a low flow rate was developed to minimize the consumption of chemicals needed for an experiment and a new perturbation technique different from the APP method was applied switching between a continuous inflow of either pure water, and the aqueous solution of the perturbing antioxidant.

RESULTS AND DISCUSSION

Perturbation of a BR system in its oscillatory regime with resorcinol causes a change in the oscillation amplitude as well as in their period see Figure 1.

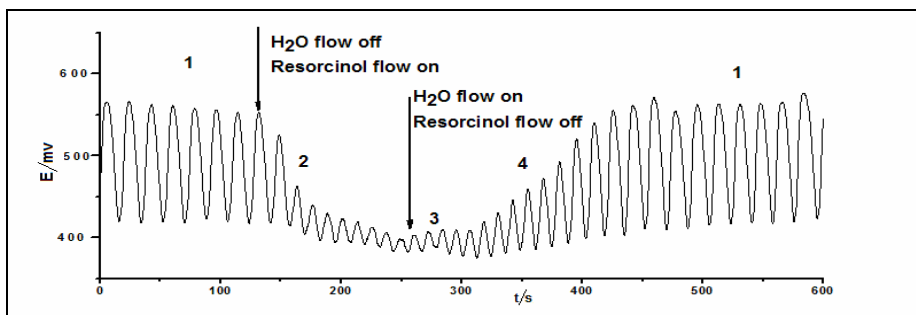


Figure 1. Evolution of an active BR mixture's oscillations in presence of resorcinol added with a 0.25mL/min flow rate for 120 s The arrows indicate the moment when feeding of 100 μM resorcinol solution was started or stopped.

State 1 represents the normal behavior of the unperturbed BR system, showing the regular oscillations of the active mixture.

The arrows indicate moments of switching from pure water to the resorcinol solution, or back. In the presence of resorcinol the amplitude and period decrease with time, and when the concentration of resorcinol reaches its maximum value in the mixture, the amplitude reaches a minimum.

Now, switching the resorcinol flow to that of distilled water, the amplitude and period increases slowly again, and finally returns to the unperturbed state. The variations of these parameters are presented in Figure 2.

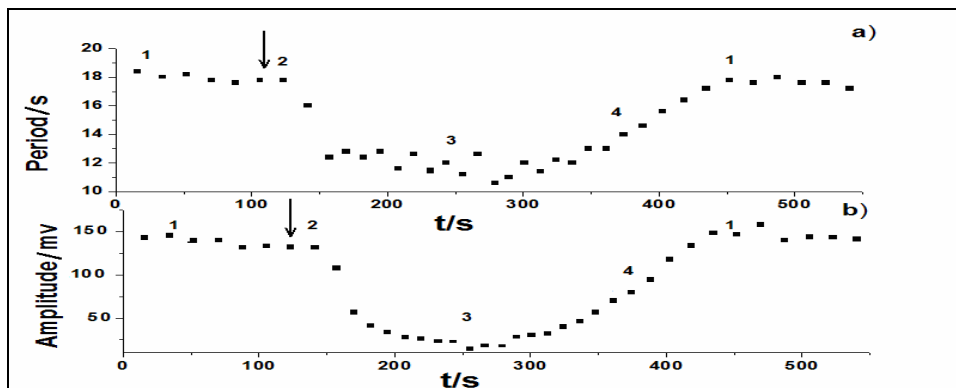


Figure 2. Variation of the period (a) and the amplitude (b) of the oscillations caused by the addition (indicated with arrow) of resorcinol.

As Figure 2 shows the system has four different dynamical states: two asymptotic (1, 3) and two transient ones (2, 4).

State 1 (asymptotic state after all transients died out):

- only H₂O is fed in the fourth channel. Stable high amplitude oscillations can be observed;

State 2 (transient between the asymptotic states 1 and 3):

- antioxidant solution is fed in the fourth channel with the same flow rate as H₂O was fed in state 1. The amplitude and the time period decrease in time;

State 3 (asymptotic state after all transients died out)

- still the antioxidant solution is fed to the reactor but the small amplitude oscillations are already stabilized;
- when the concentration of resorcinol reaches its maximum, the oscillations became monotone and stable (stage 3);

State 4 (transient between states 3 and 1):

- Feeding pure H₂O in the fourth channel is resumed. The oscillation parameters slowly reach their initial values.

It is interesting to observe that the period and amplitude changes in state 4 is more gradual than in state 2 and in a wide time interval within state 4 the period and the amplitude increase in a close to linear fashion with time.

Experiments were repeated with the same resorcinol solution, the same flow rate and identical addition time of the analyte. Results are presented in Figure 3.

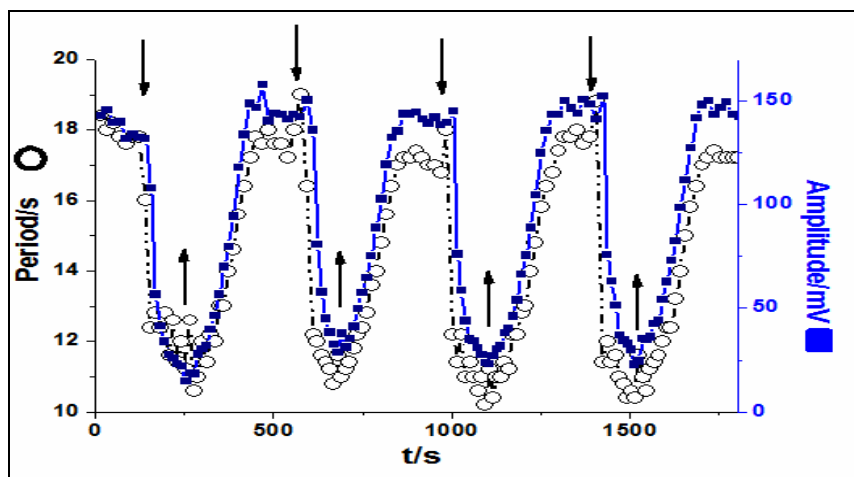


Figure 3. BR system's oscillations period and amplitude evolution caused by resorcinol inflow. The arrows pointing down indicate the moment when feeding of $100 \mu\text{M}$ resorcinol solution was started with the usual 0.25 mL/min flow rate. After 120 s the inflow of the channel was switched to pure H_2O (arrows pointing up) with the same 0.25 mL/min flow rate but for 4 minutes (time equal to mean residence time). Then the whole cycle was repeated.

The figure reveals the same pattern of oscillations during the perturbation of BR system with resorcinol solution and the repetitiveness of the behavior.

The oscillation amplitude and time period are plotted as a function of the analyte concentration of the resorcinol in Figure 4.

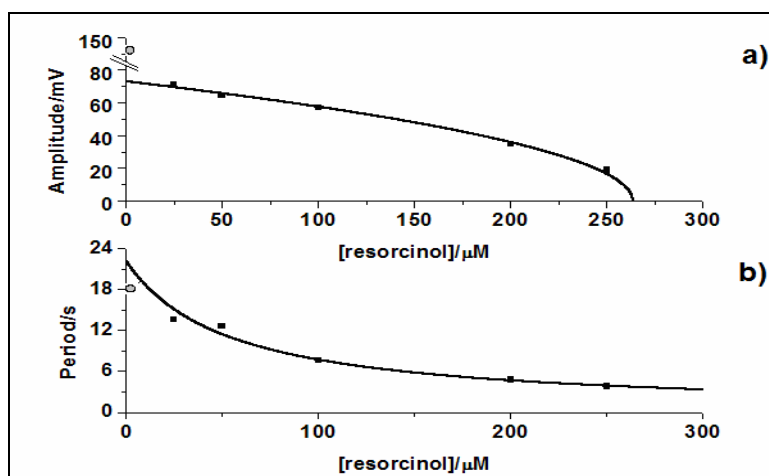


Figure 4. Plot of the amplitude a) or the period b) in state 3 (indicated with \blacksquare) vs. the concentration of resorcinol; the average period and amplitude in state 1 were indicated with (\circ)

Figure 4 shows that already 25 μM resorcinol in the inflow causes a substantial change in the dynamics as the amplitude of the oscillations is halved. On that basis one would expect that the effect of the resorcinol in the interval between 0 and 25 μM (e.g. at 12.5 μM) would be still considerable. This is not the case, however, according to our experiments. We found that the resorcinol concentration should reach a threshold level (somewhere below but close to 25 μM) before it can affect the dynamics considerably. Unfortunately, the details of that strongly nonlinear behavior close to the threshold, was difficult to study experimentally. On the other hand the dynamics was more reproducible above 25 μM thus we calibrated the system applying such resorcinol concentrations. In that region the amplitude decreases to zero smoothly with the increasing resorcinol concentration.

The parabolic type decrease of the amplitude, depicted in Figure 4 and the decreasing but finite time period of the disappearing oscillations suggested a Hopf bifurcation. To check this the square of the amplitude (the average amplitude of state 3) and the frequency (inverse of the average period of state 3) was plotted against the resorcinol concentration as a bifurcation parameter (see Figure 5).

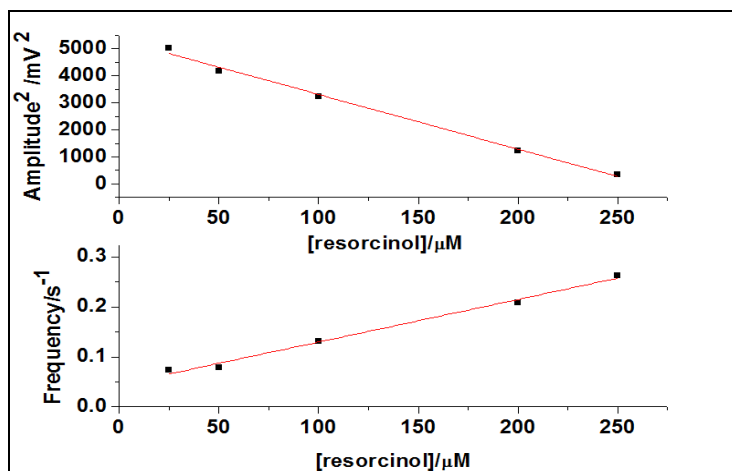


Figure 5. Plot of the analytical signal vs concentration of resorcinol

The equations of calibration curve are :

$$\text{Amplitude}^2 = 5323.38(\pm 125.4) - 20.19(\pm 0.82)[\text{resorcinol}] \quad R^2 = 0.993$$

$$\text{Frequency} = 0.045(\pm 0.0068) + 8.51 \cdot 10^{-4} (\pm 4.2 \cdot 10^{-5})[\text{resorcinol}] \quad R^2 = 0.99$$

CONCLUSIONS AND OUTLOOK

The BR system's oscillations were perturbed by continuous inflow of resorcinol into the reactor. In the 25 μM -250 μM region the square of amplitude and the frequency of the oscillations were found to be proportional to the concentration of the resorcinol in the inflow. On the basis of this relationship a new analytical method for determination of the antioxidant capacity [7] can be developed for various mono- and polyphenolic compounds

This technique is automatic, fast, relatively inexpensive, and provides two analytical signals at the same time. The approximately linear variation of the period and amplitude with the slowly decrease of resorcinol concentration in tube indicates the sensitivity of the method.

Under the selected experimental conditions, the system oscillated in the CSTR for at least 3 h, during which time as many perturbations as required to implement quantitative analytical determinations could be applied without oscillations being stopped.

Based on the time needed for the system to recover after each perturbation, the throughput can be estimated to be 8 sample/h, which is quite acceptable, taking into account how slow most oscillating reactions are. This sample throughput clearly better those of determinations based on Briggs Rauscher reaction operated in batch modem.

In such determinations, the analyte is added jointly with the reagents to the oscillating system from the start, which needs preparing a fresh sample for each analysis; this obviously reduces throughput to less than 2 sample/h.

To increase further the sensitivity of the method shorter residence times are needed. To this end higher flow rates or an even smaller CSTR is necessary, the research being in progress in our laboratoty.

EXPERIMENTAL SECTION

Apparatus. The instrumental set-up used to implement the proposed method consisted of a double walled glass vessel of 4 mL capacity, fitted with auxiliary equipment necessary to fed this CSTR with reactant solutions and an overflow pipe situated near the top of the vessel to maintain a constant volume. Connection to a FALC FA 90 thermostat ensures a constant temperature by water circulation through the temperature jacket. We have chosen a value of 25°C. Continuous and thorough stirring was provided by a FALC 60 magnetic stirrer. Reactants were pumped into the reactor by means of a peristaltic pump, through four Tygon tubes with a 0.25 mL/ min volumetric flow rate each. These Tygon tubes were connected to inlet Teflon tubes and the reagents were introduced to the reaction vessel through them. Low volumetric flow rate is necessary to reduce the volume of the processed

solution and, consequently, the cost of the experiments. The overflow outlet tube was connected to a vacuum pump and maintains a constant level of the mixture in the reactor (Figure1). Oscillations were monitored with a Pt electrode and an Ag/AgI indicator electrode, both handmade. In the BR reaction both the Platinum and the Ag/AgI electrodes are so called “indicator “ electrodes i.e. their potential oscillate with respect to a reference electrode. Such a reference electrode should be connected to the system via a double junction salt bridge. To fit a double junction salt bridge into the reactor, however, increases the reactor volume considerably. Moreover the liquid–liquid junction of a salt bridges always a source of contamination and “memories”. To keep the reactor volume at a minimum and to avoid memory effects we applied two indicator electrodes. The voltage between these electrodes in the BR reaction was found to be still oscillatory thus the dynamic state of the reactor can be followed by recording that voltage. Potentiometric traces recorded this way were quite reproducible.

They were connected to a PC through a PCI 6036 E data-acquisition interface.

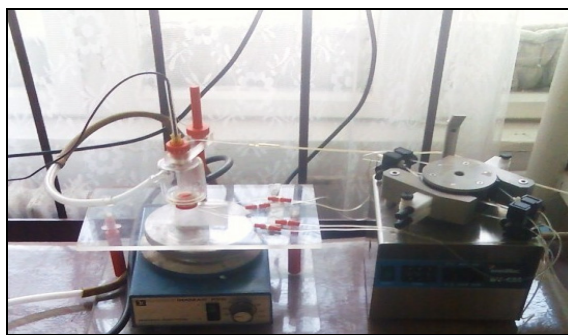
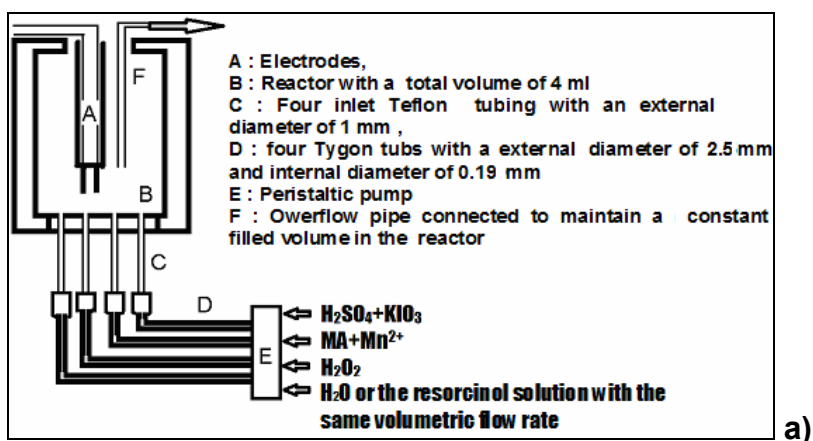


Figure 6 a) Experimental setup for implementation of oscillating reactions in a CSTR; **b)** picture of the experimental setup.

CHEMICALS AND PROCEDURE

All chemicals were of analytical grade and were used without further purification. Stock solutions with the following concentration were made: $[H_2SO_4]_0=0.078$ M, $[KIO_3]_0= 0.200$ M, $[MA]_0=0.150$ M, $[MnSO_4]_0=0,027$ M, $[H_2O_2]_0=0.023$ M by using twice distilled water

CSTR was fed with reactant solutions and water through four inlet tubings as Figure 1 shows. The volumetric feeding rate was 0.25 mL for all channels producing a 4 min residence time in the reactor. After the oscillation amplitude and period had stabilized the H₂O flow was interrupted and started the resorcinol addition to the system. After 120 s the flow of antioxidant was interrupted and replaced with water for 240 s. This procedure has been repeated several times.

APPENDIX: Hopf bifurcation

Oscillations of the state variables can occur in different dynamical systems in Physics, Biology, and in Chemistry. The same system can be both oscillatory and nonoscillatory depending on the given experimental conditions called as parameters of the system. By changing one of its parameters (denoted by μ , for example) an oscillating system can be driven from its oscillatory state to a nonoscillatory one back and forth. That qualitative change in the asymptotic behavior of the dynamical system occurring at a critical parameter value μ_c is called bifurcation. Transitions between limit cycle oscillations and stable steady states can proceed via various bifurcation scenarios which can be observed in chemical systems as well [24]. One possibility is the so called supercritical Hopf (or Poincaré-Andronov-Hopf [25]) bifurcation where oscillations are born (or disappear) with a small amplitude and with a finite time period. For dynamical systems described by ordinary differential equations the general form of the Hopf bifurcation in polar coordinates [25, 26]:

$$\frac{dr}{dt} = d\mu r + ar^3; \quad \frac{d\theta}{dt} = \omega + c\mu + br^2$$

Here r and θ are the polar coordinates in the phase plane a, b, c, d are fixed constants and μ is the bifurcation parameter. (The above formula is a good approximation of general nonlinear oscillators usually in the neighborhood of the bifurcation point only, when μ and r values are relatively small and higher order terms of the Taylor expansion used to derive the above formula can be neglected.) A special case - the so called normal form of the supercritical Hopf bifurcation - can be obtained by choosing $d=1$, and $a = -1$:

$$\frac{dr}{dt} = \mu r - r^3; \quad \frac{d\theta}{dt} = \omega + c\mu + br^2$$

The above system has one fixed point which is in the origin ($r=0$). By changing the parameter μ the following bifurcation scenario can be observed. When $\mu < 0$ the fixed point is a stable focus but when $\mu > 0$ it becomes an unstable one and a small stable limit cycle appears surrounding the unstable focus.

Thus in the normal form the supercritical Hopf bifurcation takes place at $\mu_c = 0$. The amplitude r_{LC} of the limit cycle oscillations can be calculated as

$$r_{LC} = \sqrt{\mu} ,$$

because limit cycle oscillation is an asymptotic state where:

$$\frac{dr}{dt} \Big|_{LC} = 0$$

The frequency ω_{LC} of the limit cycle oscillations can be obtained by substituting r_{LC} into the second differential equation:

$$\omega_{LC} = \frac{d\theta}{dt} \Big|_{LC} = \omega + f\mu \quad \text{where } f = (c + b)$$

Thus in the case of a supercritical Hopf bifurcation when plotting the frequency or the square of the amplitude of the limit cycle oscillations vs. μ the bifurcation parameter linear graphs will be obtained as:

$$r_{LC}^2 = \mu \quad \text{and} \quad \omega_{LC} = \omega + f\mu$$

In our experiments the bifurcation parameter should be proportional with the resorcinol concentration. An increase of this parameter, however, causes not an increase but a decrease of the oscillation amplitude in our experiments. Another deviation from the simple normal form is that the critical parameter value, (where the oscillations disappear) is not zero but occurs at a finite resorcinol concentration. Thus, to be compatible with the above normal form picture the bifurcation parameter can be chosen as:

$$\mu \propto (c_c - c)$$

Where c_c is the critical resorcinol concentration where the oscillations disappear. (In these linear graphs the factor of proportionality does not play a role thus it is not denoted.) This transformation of the experimental parameter c to the theoretical bifurcation parameter is not necessary, however, to evaluate the experimental data, as linear plots of the frequency vs. c and (amplitude)² vs. c can be obtained without such a transformation.

ACKNOWLEDGMENTS

This work was partially supported by OTKA grants K-60867 and K-77908 and by the foundation Domus Hungarica Scientiarum et Artium. N. M. thanks the ESF Programme Functional Dynamics for supporting his visits to Z. Noszticzius's lab.

REFERENCES

1. R. Jimenez Prieto, M. Silva, D. Perez Bendito, *Analyst*, **1998**, *123*, 1R-8R.
2. S. K. Scott, "Oscillations waves and chaos in chemical kinetics", Oxford, **1998**.
3. I. R. Epstein, J. A. Pojman, "An introduction to nonlinear chemical dynamics", Oxford, **1998**.
4. S. K. Scott, B. R. Johnson, A. F. Taylor, M. R. Tinsley, *Chemical Engineering Science*, **2000**, *55*, 209.
5. Z. Noszticzius., W.D McCormick, H. L. Swinney, *J. Phys. Chem.*, **1989**, *93*, 2796.
6. E. Briggs, A. Rauscher, *J. Chem. Educ.*, **1973**, *50*, 496.
7. R. A. Moyer, K. E. Hummer, C. E. Finn, B. Frei, Wrolstad, *J. Agric Food Chem.*, **2002**, *50*, 519.
8. R. Cervellati, N. Crespi-Perellino, S. D. Furrow, M. Anacleto, *Helv. Chim. Acta*, **2000**, *83*: 12, 3179.
9. R. Cervellati, K. Hoener, S. D. Furrow, C. Neddens, S. Costa, *Helv. Chim. Acta*, **2001**, *84*(12), 3533.
10. R. Cervellati, C. Renzulli, M. C. Guerra, E. Speroni, *J. Agric. Food Chem.*, **2002**, *50*, 7504.
11. L. Onel, G. Bourceanu, M. Wittmann, Z. Noszticzius, G. Szabó, *J. Phys. Chem. A.*, **2008**, *112*, 11649.
12. T. Lawson, J. Fülöp, M. Wittmann, Z. Noszticzius, N. Muntean, G. Szabó, L. Onel, *J. Phys. Chem. A.*, **2009**, *113*, 14095.
13. N. Muntean, G. Szabó, M. Wittmann, T. Lawson, Z. Noszticzius, J. Fülöp, L. Onel, *J. Phys. Chem. A.*, **2009**, *113*, 9102.
14. R Cervellati, K. Hoener, S. R. Furrow, F. Mazzanti, *Helv. Chim. Acta*, **2002**, *85*: (8), 2523.
15. R. Jimenez-Prieto, M. Silva, D. Perez Bendito, *Analyst*, **1997**, *122*, 287.
16. R. Jahan-Bakhsh, O. Reza, Abolfazl, *Analytical Sciences*, **2004**, *20*, 883.
17. M. Orbán, *J. Am. Chem. Soc.*, **1986**, *108*, 6893.
18. L. Minuti, R. Pellegrino, *J. Chromatogr. A*, **2008**, *1185*, 23.
19. Jinzhang Gao, Jie Ren, Wu Yang, Xiuhui Liu, Hua Yang, Qizhi Li, Hualing Deng, *J. Electroanal. Chem.*, **2002**, *520*, 157.
20. Jinzhang Gao, Hua Yang, Xiuhui Liu, Jie Ren, Xiaoquan Lu, Jingguo Hou, Jingwan Kang, *Talanta*, **2001**, *55*, 99.
21. Peter E. Strizhak, Olga Z. Didenko, Tatyana S. Ivashchenko, *Anal. Chim. Acta*, **2001**, *428*, 15.
21. H. Chen, W. Yang, H. Xia Dai, X. Xia Wei, J. Qu, J. Zhang Gao, *Chin. Chem. Letters*, **2006**, *17*(9), 1221.
23. J. Gao, H. Yang, X. Liu, J. Ren, L. Qizhi, J. Kang, *Talanta*, **2007**, *57*, 105.

24. Z. Noszticzius, P. Stirling, M. Wittmann, *J. Phys. Chem.*, **1985**, *89*, 4914.
25. S. Wiggins, "Introduction to Applied Nonlinear Dynamical systems and Chaos", Springer, New York, **1990**, p. 272.
26. J. Guckenheimer, P. Holmes, "Nonlinear Oscillations, Dynamical Systems, and Bifurcations of Vector Fields", Springer, New York, **1986**, p. 151.